Frequency metrology of the 1S-3S transition of hydrogen: contribution to the proton charge radius puzzle

Hélène Fleurbaey

▶ **To cite this version:**

Hélène Fleurbaey. Frequency metrology of the 1S-3S transition of hydrogen: contribution to the proton charge radius puzzle. Atomic Physics [physics.atom-ph]. Université Pierre et Marie Curie (UPMC), 2017. English. NNT : . tel-01633631

HAL Id: tel-01633631

https://theses.hal.science/tel-01633631

Submitted on 13 Nov 2017

HAL is a multi-disciplinary open access archive for the deposit and dissemination of scientific research documents, whether they are published or not. The documents may come from teaching and research institutions in France or abroad, or from public or private research centers.

L'archive ouverte pluridisciplinaire **HAL**, est destinée au dépôt et à la diffusion de documents scientifiques de niveau recherche, publiés ou non, émanant des établissements d'enseignement et de recherche français ou étrangers, des laboratoires publics ou privés.

THÈSE DE DOCTORAT
DE L'UNIVERSITÉ PIERRE ET MARIE CURIE

Spécialité : Physique

École doctorale : "Physique en Île-de-France"

réalisée

au Laboratoire Kastler Brossel

présentée par

Hélène FLEURBAEY

pour obtenir le grade de :

DOCTEUR DE L'UNIVERSITÉ PIERRE ET MARIE CURIE

Sujet de la thèse :

Métrologie de la fréquence de transition 1S–3S dans l'hydrogène : contribution au débat sur le rayon de charge du proton

Frequency metrology of the 1S–3S transition of hydrogen: contribution to the proton charge radius puzzle

soutenue le 26 octobre 2017

Composition du jury :

M^{me}	Anne Amy-Klein	Rapporteuse
M.	François Biraben	Invité
M^{me}	Caroline Champenois	Rapporteuse
M^{me}	Emily Lamour	Présidente du jury
M^{me}	Helen Margolis	Examinatrice
M.	François Nez	Directeur de thèse

Remerciements

Ces quelques lignes seront trop courtes pour rendre compte de l'ambiance familiale et chaleureuse de l'équipe de métrologie du LKB. Tant de bons souvenirs se pressent dans ma mémoire, la fascination de la salle de manip, la joie de voir le premier signal de transition du deutérium, nos discussions passionnées lors des pauses thé, ...

Je remercie de tout coeur François Nez, mon directeur de thèse, qui a su être toujours présent. J'ai beaucoup appris à ses côtés, tant sur le plan expérimental, de l'optique à l'électronique en passant par la construction de boîtes en bois, qu'à travers ses qualités humaines, la patience étant de mise sur une expérience comme la nôtre. ... sans oublier ses réserves de chocolats !

Je tiens à exprimer toute ma gratitude à Lucile Julien. C'est grâce à son cours de physique atomique que je suis entrée dans cette équipe inoubliable. Sa grande gentillesse et son sens de la pédagogie m'ont été d'un grand secours tout au long de ces trois années de thèse et des stages qui les ont précédées, et je lui en suis reconnaissante.

Je remercie profondément François Biraben, pour son aide précieuse et sa patience pour m'expliquer les bases de l'analyse de données. Son statut de chercheur émérite, tout en lui permettant de profiter du beau temps, ne l'a pas empêché d'être toujours disponible pour répondre à mes questions, et je lui en sais gré.

J'ai eu la chance de bénéficier d'un encadrement idéal, tous les trois apportant ainsi leurs compétences qui se complètent. Je remercie également Saïda Guellati pour sa douceur et sa présence apaisante, ainsi que Pierre Cladé pour ses conseils sur la programmation en Python.

Je remercie Anne Amy-Klein et Caroline Champenois d'avoir accepté de rapporter sur ce manuscrit, ainsi que Helen Margolis, Emily Lamour et Ferdinand Schmidt-Kaler pour l'intérêt qu'ils ont porté à ce travail.

Je voudrais remercier Astrid Lambrecht qui a accepté d'être ma marraine au sein du laboratoire, ainsi que Noël Dimarcq en sa qualité de co-directeur de thèse.

Un grand merci à Ouali Acef pour son laser qui est devenu indispensable pour notre expérience, et pour son accueil le temps de préparer un montage transportable pour ledit laser. Je remercie également l'équipe du SYRTE qui nous fournit la référence de fréquence, ainsi que tous ceux qui ont contribué aux divers essais d'asservissement du peigne de fréquence.

Je remercie vivement Sandrine Galtier, qui m'a transmis son savoir-faire au cours de mes trop courts mois de stage à ses côtés. Je souhaite bon courage à Simon Thomas, qui me succède sur la manip hydrogène ; grâce à ses talents d'expérimentateur, je sais qu'elle sera en de bonnes mains ! Merci également à Marie Bonnaud pour son sourire durant nos journées passées dans la pénombre de la salle de manip.

Je voudrais aussi remercier les autres doctorants de l'équipe et/ou collègues de bureau : Manuel Andia, pour son amitié, Clément Courvoisier, pour sa bonne humeur contagieuse, Raphaël Jannin, Léo Morel, Pauline Comini, pour les chocolats suisses et les raisins italiens, et Bian Guojie pour ses cadeaux de Chine.

Je remercie pêle-mêle tous les membres du laboratoire, chercheurs ou enseignants-chercheurs, doctorants ou post-docs, techniciens ou personnels administratifs, trop nombreux pour les nommer ici, avec qui j'ai partagé d'amicales discussions autour de la table de la cafétéria ou ailleurs.

Je remercie tout particulièrement Jean-Michel Isac et tous les membres de l'atelier de mécanique, pour le « cryostat », et aussi pour leur aide efficace face aux diverses pannes et fuites d'eau.

Je remercie Brigitte Delamour, Loïc Garcia et Jean-Pierre Opkisz, du service d'électronique, pour leur disponibilité, ainsi que Florence Thibout qui nous a fabriqué les petits tubes en quartz pour la fluorescéine.

Merci à Annick Lamarck et Bintou Maïga, qui égayent les locaux par leur présence matinale. Je souhaite une belle retraite à Annick !

Je remercie tous les membres du secrétariat, ainsi que Delphine Charbonneau et Valérie Revelut, pour leur efficacité et leur bonne humeur.

J'aimerais remercier Jérôme Simon, et tout l'orchestre, pour notre passion partagée de la musique. Merci également à Audrey et Gaëlle pour leur amitié et leur soutien.

Enfin, un merci infini à mes parents qui m'ont toujours soutenue et encouragée, même depuis l'autre bout du monde ! et en effet, la « vallée de la Thèse », ça descend tout seul, même si il y a parfois des rapides !

Contents

Introduction

The work presented in this manuscript has been realized from 2014 to 2017 in the "Metrology of simple systems and fundamental tests" team of Laboratoire Kastler Brossel, under the supervision of François Nez.

The team has a decades-long experience in high-resolution two-photon spectroscopy of hydrogen and deuterium. Hydrogen spectroscopy plays a key role in the determination of the Rydberg constant, and in testing fundamental theories such as the quantum electrodynamics theory. Recent results from the spectroscopy of muonic hydrogen have given rise to a controversy around the value of the proton charge radius. This has caused a renewed interest in precise measurements in electronic hydrogen.

Our experiment is focused on the measurement of the two-photon $1S-3S$ transition frequency of hydrogen. Several systematic effects must be taken into account, most importantly the second-order Doppler shift, which depends on the atomic velocity. An original method to estimate the velocity distribution of the hydrogen atoms was implemented during the Ph.D. of Gaëtan Hagel [Hagel2001].

Using this method, Olivier Arnoult was able to measure the $1S-3S$ transition frequency with an uncertainty of 13 kHz, or a relative uncertainty of 4.4×10^{-12} [Arnoult2010]. This made it the second most precisely known optical transition frequency in hydrogen. Nevertheless, this uncertainty is not sufficient to discriminate between the two conflicting values of the proton radius.

During her Ph.D. realized from 2011 to 2014, Sandrine Galtier modified the excitation laser source and performed a new measurement with a promising statistical uncertainty of 2.1 kHz [Galtier2014a]. However, it was impossible to conclude on the absolute frequency value because of an unresolved question surrounding the collisional shift and a possible pressure dependence of the velocity distribution.

In the present work, after tackling with several experimental issues, we have estimated the velocity distribution at several pressure values and obtained a new measure of the $1S-3S$ transition frequency, which contributes to the ongoing search to solve the proton radius puzzle.

The outline of this manuscript is the following.

The first chapter starts with a general overview of the theory of hydrogen energy levels. It then underlines the important role of hydrogen spectroscopy, both in the determination of the Rydberg constant and in the context of the proton radius puzzle. The last part of the chapter presents the principle of our $1S-3S$ experiment, in particular the method used to determine the atomic velocity distribution and the second-order Doppler shift, and gives a brief review of recent experimental improvements.

The second chapter is devoted to the experimental setup. The 205-nm excitation laser, obtained by sum frequency generation, is described, along with the frequency stabilization and measurement system. The atomic beam, and the power build-up cavity in which the excitation takes place, are also presented. This chapter ends with an description of the recording process, and the observed transition signals.

In the third chapter, systematic effects are considered. After a presentation of the theoretical line profile, which includes velocity-dependent effects, other shifting and broadening effects are discussed. In particular, the light shift and collisional shift are important in our experiment. The cross-damping effect is studied theoretically in detail.

The last chapter presents the analysis of the data recorded during my Ph.D. After correcting from various systematic effects, a new value of the $1S-3S$ transition frequency is obtained, which is significantly more precise than our last published measurement. Furthermore, through a complete study of the velocity distribution for different pressure values, this work has allowed to answer the question raised during Sandrine Galtier's Ph.D. and fully analyze the data recorded at the time.

Chapter 1

Context and principle

The aim of this chapter is to give a general introduction to the historical and theoretical context of our experiment. Hydrogen is the simplest element, composed of one proton and one electron. This allows a good theoretical description of the electronic energy levels. The spectroscopy of hydrogen plays an important role in determining the Rydberg constant and in testing the quantum electrodynamics (QED) theory. In this context, a puzzle has recently arisen around the value of the proton charge radius. Finally, I will present the general principle and a short historical review of our $1S-3S$ experiment, which contributes to the ongoing search to solve this puzzle.

1.1 Theory of hydrogen energy levels

1.1.1 From the Bohr model to the Dirac equation

Let us start from the simple model, proposed by Niels Bohr in 1913, which describes an electron of charge $-e$ and mass m_e orbiting around a nucleus of infinite mass. This model predicts that the energy levels of this atom can be expressed in terms of a quantum number n as

$$E_n = -hcR_\infty \frac{1}{n^2}, \tag{1.1}$$

where h is the Planck constant, c the speed of light, and R_∞ the Rydberg constant

$$R_\infty = \frac{m_\mathrm{e} e^4}{8\epsilon_0^2 h^3 c}, \tag{1.2}$$

with ϵ_0 the vacuum permittivity.

In order to take into account the "recoil" of the nucleus, that is the motion of the nucleus due to its finite mass m_p, one can simply replace, in eq. (1.1), the electron mass by the reduced mass

$$m_\mathrm{r} = \frac{m_\mathrm{e} m_\mathrm{p}}{m_\mathrm{e} + m_\mathrm{p}}, \tag{1.3}$$

where m_p is the mass of the proton.

The Schrödinger equation, which describes the evolution of a wavefunction depending on three quantum numbers (n, L, m), can be applied to the case of an electron experiencing the attractive Coulomb potential of an infinitely massive proton. It yields the same energy levels as the Bohr model.

The theory was refined by Paul Dirac in 1928. The general equation which bears his name takes into account the relativistic motion of the electron. The spin of the electron appears naturally in this equation. The coupling of the magnetic moment associated to this spin with the orbital angular momentum (described by L) of the electron contributes to the fine structure.

The Dirac energy levels, solutions of this equation, depend on two quantum numbers: n and J, the latter corresponding to the total angular momentum of the electron. Including the rest energy of the electron into the total energy, they can be written in the approximation of an infinitely massive nucleus as

$$E_D = m_\mathrm{e}c^2 f(n, J), \tag{1.4}$$

where

$$f(n, J) = \left[1 + \frac{(Z\alpha)^2}{(n-\delta)^2}\right]^{-1/2}, \tag{1.5}$$

with $Z = 1$ the charge number of the nucleus, α the fine structure constant and

$$\delta = J + \frac{1}{2} - \sqrt{\left(J + \frac{1}{2}\right)^2 - (Z\alpha)^2}. \tag{1.6}$$

The fine structure constant α is linked to the Rydberg constant R_∞ through the relation

$$hcR_\infty = \frac{1}{2} m_\mathrm{e} c^2 \alpha^2. \tag{1.7}$$

To take into account the recoil of the proton due to its finite mass, it is not sufficient to simply replace the electron mass in eq. (1.4) by the reduced mass m_r defined in eq. (1.3), as we have done for the Bohr levels.

Actually, the general expression of the Dirac energy levels, taking into account this recoil correction as well as the rest energies of the proton and electron, is defined in [Barker1955, Sapirstein1990] as

$$\begin{aligned} E_M &= Mc^2 + [f(n,J) - 1]m_\mathrm{r}c^2 - [f(n,J)-1]^2 \frac{m_\mathrm{r}^2 c^2}{2M} + \frac{(Z\alpha)^4}{2n^3} \frac{m_\mathrm{r}^3 c^2}{m_\mathrm{p}^2} \frac{1 - \delta_{L0}}{\kappa(2L+1)} \\ &\quad + \ldots \end{aligned} \tag{1.8}$$

with $M = m_\mathrm{e} + m_\mathrm{p}$ and $\kappa = (-1)^{J-L+\frac{1}{2}}(J + \frac{1}{2})$.

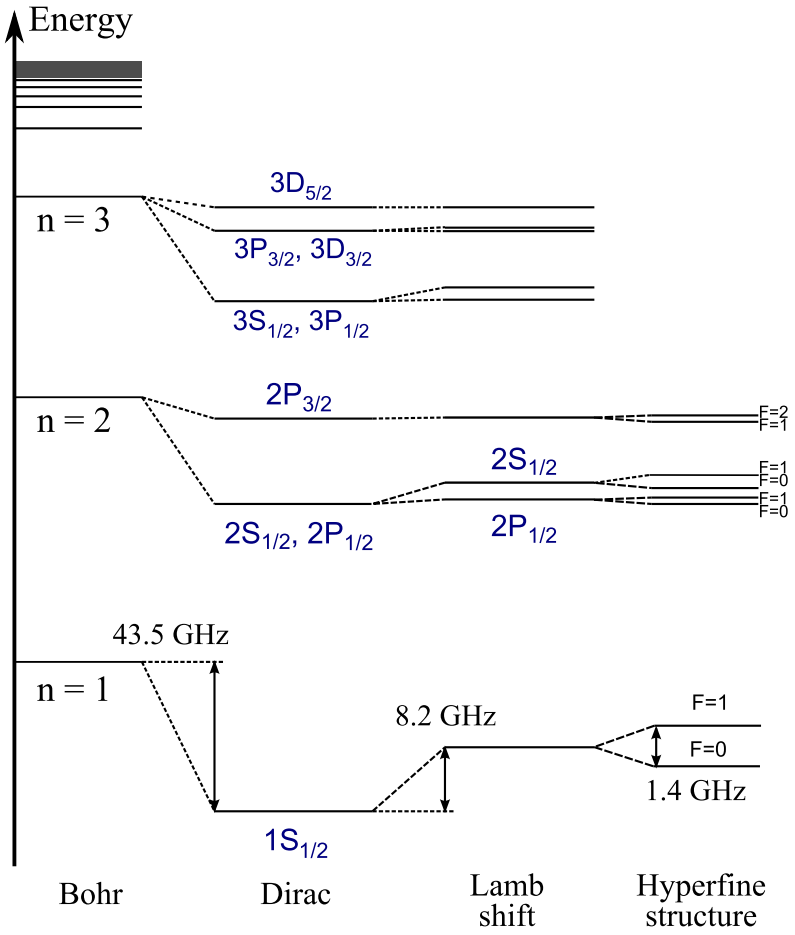

Figure 1.1: Structure of the lowest hydrogen energy levels ($n = 1, 2, 3$). The drawing is not to scale. The Lamb shift (see part 1.1.2) lifts the degeneracy of Dirac levels with same n and J. Moreover, because of the hyperfine structure (see part 1.1.3), each level is actually split in two.

Figure 1.1 shows the lowest energy levels of hydrogen. On the left hand side, the Bohr energy levels depend only on n. The Dirac energy levels are represented in spectroscopic notation as nL_J, with the orbital momentum quantum number L denoted by a letter $(S, P, D, \ldots)$.

Up to first order in recoil correction, the Dirac energy levels with different L but same n and J are degenerate and have the same energy, as shown in Fig. 1.1. However, in practice this degeneracy is broken.

In fact, the $2S_{1/2} - 2P_{1/2}$ splitting was first observed experimentally in 1947 by W. E. Lamb and R. C. Retherford [Lamb1947]. These levels are about 1 GHz apart. Actually, all levels are shifted with respect to the Dirac energy. This shift, which has become known as the Lamb shift, is more important for S levels ($L = 0$) and varies approximately as $1/n^3$. It will be explained in the next part.

1.1.2 The Lamb shift

It is now a fairly common convention to define, as in [Eides2007], the total hydrogen energy levels (averaging over or neglecting the hyperfine structure which is quite decoupled from other effects and will be presented later) as

$$E_{nLJ} = E_{nJ}^{DR} + L_{nLJ}, \tag{1.9}$$

where E_{nJ}^{DR} takes into account the solution of the Dirac equation and the first-order recoil correction (second and third terms of eq. (1.8)), and the Lamb shift L_{nLJ} includes the higher-order relativistic recoil corrections, radiative terms described by quantum electrodynamics (QED) as well as the finite nuclear size effect.

Apart from this last term, all contributions to the Lamb shift can be written as power series of α, $Z\alpha$ and/or m_e/m_p. In first approximation, the Lamb shift contributions vary as $1/n^3$. In the following I will give a brief overview of the different terms, which are presented in detail elsewhere, for instance in [Eides2007, Mohr2016].

Radiative corrections

These corrections, described by the quantum electrodynamics (QED) theory, can be expressed as power series of α and $Z\alpha$. It should be noted that the coefficients of the power series may themselves be slowly varying functions (logarithms) of these parameters.

Self-energy The self-energy is the most important QED contribution in electronic hydrogen. It is due to the emission and reabsorption of virtual photons by the electron, as illustrated in Fig. 1.2. It tends to reduce the binding energy of the electron in S states ($L = 0$), for which the probability of presence inside the nucleus is highest. This increases the energy of the S levels. The leading order contribution scales as $\alpha(Z\alpha)^4$.

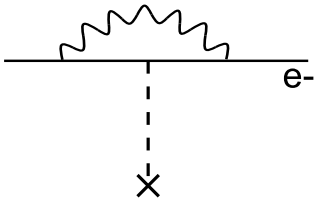

Figure 1.2: Feynman diagram of the one-loop (or one-photon) contribution to self-energy. The electron emits and reabsorbs a virtual photon. The dashed line symbolizes the Coulomb interaction between the electron and the proton, represented by a cross.

Vacuum polarization This term is due to the spontaneous creation of positron-electron (e^+e^-) pairs between the proton and electron (see Fig. 1.3). These virtual

pairs become polarized, as the positron is repelled by the nucleus while the virtual electron is attracted. This induces an additional attractive potential at short distance. Hence, the electron has a higher binding energy, so that the energy levels are lowered. For S states, as the electron is closer to the nucleus, the negative correction is more important, with leading order $\alpha(Z\alpha)^4$.

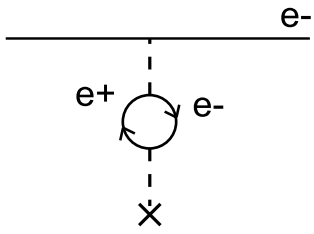

Figure 1.3: Feynman diagram of the one-loop contribution to vacuum polarization. A virtual electron-positron pair appears in the Coulomb propagator.

There are also smaller contributions due to the creation of $\mu^+\mu^-$ and hadronic pairs.

Two-photon corrections The two-photon or two-loop corrections are second-order QED corrections. For instance, in the two-loop contribution to self-energy, the electron would emit, and reabsorb, two photons. These terms involve many complicated integrals and are very hard to calculate precisely. The leading-order two-photon correction is proportional to $\alpha^2(Z\alpha)^4$. Three-loop corrections can also be calculated, but four-loop contributions are considered negligible [Mohr2016].

Recoil corrections

The first-order recoil correction has already been taken into account in the Dirac energy levels via eq. (1.8). Higher-order recoil corrections are described by a relativistic two-body problem. They can be written as power series of $Z\alpha$ and $m_\mathrm{e}/m_\mathrm{p}$, with leading order $(Z\alpha)^5(m_\mathrm{e}/m_\mathrm{p})$. There are also radiative recoil corrections, which depend on all three parameters α, $Z\alpha$ and $m_\mathrm{e}/m_\mathrm{p}$. These terms are complicated but small, as the leading order is $\alpha(Z\alpha)^5(m_\mathrm{e}/m_\mathrm{p})$.

Finite nuclear size

There are several non-electromagnetic contributions due to weak and strong interactions. The largest contribution arises from the fact that the proton is not a point-like elementary particle, but is composed of three quarks interacting with a sea of gluons. Hence, it has a spatial charge distribution $\rho_E(\mathbf{r})$. The "proton charge radius" r_p is

defined as the square root of the second moment of the charge distribution,

$$r_{\mathrm{p}} = \sqrt{\langle r^2 \rangle} \text{ with } \langle r^2 \rangle = \frac{\int r^2 \rho_E(\mathbf{r}) d^3\mathbf{r}}{\int \rho_E(\mathbf{r}) d^3\mathbf{r}}. \tag{1.10}$$

Because of this spatial distribution, the Coulomb potential of the nucleus is screened at short distance, so that the electron feels a less attractive potential. This effect is large only for S states where the wavefunction overlap of the proton and electron is the largest: the binding energy is reduced as the electron penetrates the volume of the nucleus.

The leading order contribution for S states is

$$E_{\mathrm{NS}}^{(0)} = \frac{2}{3} \left(\frac{m_{\mathrm{r}}}{m_{\mathrm{e}}}\right)^3 \frac{(Z\alpha)^2}{n^3} m_{\mathrm{e}} c^2 \left(\frac{2\pi Z\alpha r_{\mathrm{p}}}{\lambda_{\mathrm{c}}}\right)^2 \delta_{l0}, \tag{1.11}$$

where λ_{c} is the Compton wavelength of the electron defined by $\lambda_{\mathrm{c}} = h/m_{\mathrm{e}}c$.

Nuclear structure also gives rise to other, much smaller effects such as the nuclear self-energy and polarizability, and nuclear corrections to self-energy and vacuum polarization.

1.1.3 Hyperfine structure

A final contribution to the hydrogen energy levels is the hyperfine structure, which induces an additional splitting. It is due to the coupling between the electronic total angular momentum $\mathbf{J} = \mathbf{L} + \mathbf{S}$ and the spin $\mathbf{I}$ of the nucleus. As the proton has a spin $I = 1/2$, each energy level is actually split in two sublevels described by an additional quantum number F, with $F = J - 1/2, J + 1/2$. The energy difference between these sublevels is called the hyperfine splitting. Each hyperfine level can itself be decomposed in $2F + 1$ sublevels, distinguished by the quantum number m_F, which have the same energy in the absence of external perturbations.

The hyperfine splittings of the $1S_{1/2}$ and $2S_{1/2}$ energy levels of hydrogen have been experimentally measured, and are listed in Table 1.1. These experimental measurements are much more precise than the theoretical calculations which are limited by the nuclear structure effects [Karshenboim2002].

Level	Hyperfine splitting (Hz)	Reference
H, $1S_{1/2}$	1 420 405 751.768(1)	[Hellwig1970]
H, $2S_{1/2}$	177 556 785(29)	[Rothery2000]
H, $2S_{1/2}$	177 556 834.3(6.7)	[Kolachevsky2009]

Table 1.1: Experimental measurements of hyperfine splittings. For these S levels, this corresponds to the energy difference between the $F = 0$ and $F = 1$ sublevels.

The hyperfine splitting of S levels scales approximately as $1/n^3$. To calculate the $3S$ hyperfine splitting, one could naively multiply the experimental value[1] of the $2S$ splitting by 8/27 to obtain

$$\Delta E_{\mathrm{HFS}}(3S_{1/2}) = 52.609\,432 \text{ MHz}. \tag{1.12}$$

As detailed in [Galtier2014a], the hyperfine splitting includes relativistic and radiative corrections and can be written more accurately as

$$\Delta E_{\mathrm{HFS}} = \frac{E_F}{n^3}(1+\epsilon), \tag{1.13}$$

where E_F is the Fermi energy, and ϵ is a correction whose main relativistic contribution has been calculated by Breit [Erickson1965] as

$$\begin{aligned} \epsilon_{Br}(nS) &= \frac{11n^2+9n-11}{6n^2}(Z\alpha)^2 \\ &\quad + \frac{203n^4+225n^3-134n^2-330n+189}{72n^4}(Z\alpha)^4 + \dots \end{aligned} \tag{1.14}$$

We can determine the $3S$ hyperfine splitting more accurately by using eqs. (1.13) and (1.14). This yields

$$\Delta E_{\mathrm{HFS}}(3S_{1/2}) = 52.609\,445 \text{ MHz}, \tag{1.15}$$

which differs by 13 Hz from the previous value (eq. (1.12)). This is the value that we should use thereafter, with an uncertainty of about 10 Hz.

1.2 Hydrogen spectroscopy and the proton radius puzzle

1.2.1 High-resolution spectroscopy

As we have seen, hydrogen energy levels can be well described theoretically. Differences between these levels can be experimentally investigated with great precision through spectroscopy, the measure of transition frequencies.

The electron can jump from one level to another by emitting or absorbing photons. Due to parity relations, only some transitions are allowed, while others are forbidden. The selection rules for one-photon (electric dipole) transitions require for instance that the levels verify $\Delta L = \pm 1$. Excited states, which can decay spontaneously to lower energy levels, have very different lifetimes depending on the possible transitions.

For instance, the $2S_{1/2}$ state cannot decay spontaneously through a one-photon

[1] The weighted mean of the two values in Table 1.1.

transition, since there is no lower energy state with $L = 1$. It is so-called metastable, with a lifetime of about 120 ms. By contrast, the $2P$ levels have a lifetime of only 1.6 ns. To the lifetime τ is associated a natural spectral linewidth $\Gamma = 1/2\pi\tau$.

In practice, the transitions are usually broadened. In particular, the Doppler effect due to the thermal agitation of the atoms induces a Gaussian broadening which can be very large, limiting the measurement precision. To go beyond this limit, several spectroscopy techniques have been developed.

Saturated absorption spectroscopy relies on a velocity-selective method. Atoms in a cell are illuminated by two counter-propagating laser beams of same frequency: an intense pump beam and a weaker probe beam. The pump induces a saturation of the transition, depopulating the lower energy state for a given longitudinal velocity class which depends on the laser frequency. The absorption of the probe beam is monitored while the laser frequency is scanned. When the laser is resonant with the transition, the pump and probe beams address the same velocity class (null longitudinal velocity) and the probe beam is less absorbed. As an example, the saturated absorption spectroscopy of the Balmer-α hydrogen line ($n = 2 \rightarrow n = 3$) enabled the first optical observation of the $2S - 2P$ Lamb shift [Hänsch1972].

Another important technique is the two-photon Doppler-free spectroscopy. In two-photon transitions which link energy states of same parity ($\Delta L = 0, \pm 2$), the atom absorbs two photons at the same time. If an atom is illuminated by two counter-propagating laser beams of same frequency (for instance inside a power build-up cavity), it can absorb one photon from each beam and the first-order Doppler effect cancels out. Thanks to this technique, it is possible to achieve tremendous precision.

For instance, one of the most precise optical frequency measurements is the $1S-2S$ two-photon transition frequency, measured since 1975 by the group of T. W. Hänsch in Garching. Over the years, the experiment has been refined to reach an uncertainty of 10 Hz, or a relative uncertainty of 4×10^{-15} [Parthey2011]. This is rendered possible by the long lifetime of the $2S$ level, which gives this transition a very narrow natural linewidth of 1.3 Hz.

In Paris, our group has studied the $2S - nS/D$ two-photon transitions between 1985 and 2000 [deBeauvoir2000]. These transitions are crucial to the determination of the Rydberg constant.

1.2.2 Determining the Rydberg constant

Every four years, the CODATA[2] Task Group on Fundamental Physical Constants performs a global adjustment of the fundamental constants, based on the latest experimental and theoretical results. The Rydberg constant, in particular, is obtained

[2]Committee on Data for Science and Technology

by a least squares adjustment that takes into account all the available data from hydrogen and deuterium spectroscopy, as well as QED calculations. The value of the Rydberg constant obtained by the latest CODATA adjustment [Mohr2016] is

$$R_\infty = 10\,973\,731.568\,508(65)\ \mathrm{m}^{-1}, \tag{1.16}$$

with a relative uncertainty of 5.9×10^{-12}.

In this section I would like to give a flavor of how the Rydberg constant can be determined, in a simple manner, from hydrogen spectroscopy. Let us go back to eq. (1.9), which we can rewrite as

$$E_{nLJ} = a_{nJ} hcR_\infty + L_{nLJ}, \tag{1.17}$$

where $a_{nJ} \simeq -1/n^2$ is an exactly known function of α and $m_\mathrm{e}/m_\mathrm{p}$.

Spectroscopy gives us access to differences between energy levels. For instance, one could wish to determine R_∞ directly from the $1S-2S$ transition frequency, which is very precisely known. The precision on the Rydberg constant obtained in this way is limited by the knowledge of the theoretical Lamb shifts $L_{1S_{1/2}}$ and $L_{2S_{1/2}}$, or more accurately by that of the proton radius, which would have to be determined from scattering experiments (see next section).

Combining two transition frequencies allows to circumvent this drawback. For instance, one could use two of the most well-known transition frequencies ($1S-2S$ and $2S-8D$) which can be written, using eq. (1.17), as

$$\nu_{1S_{1/2}-2S_{1/2}} \simeq \frac{3}{4} cR_\infty + (L_{2S_{1/2}} - L_{1S_{1/2}})/h, \tag{1.18}$$

$$\nu_{2S_{1/2}-8D_{5/2}} \simeq \frac{15}{64} cR_\infty + (L_{8D_{5/2}} - L_{2S_{1/2}})/h. \tag{1.19}$$

At the same time, we can take advantage of the fact that many contributions to the Lamb shift L_{nLJ} follow a $1/n^3$ scaling law, so that the deviation from this law,

$$\Delta_n = n^3 L_{nS_{1/2}} - L_{1S_{1/2}}, \tag{1.20}$$

can be very precisely calculated [Czarnecki2005]. Besides, the Lamb shift for high n and L is known theoretically with sufficient precision.

This set of equations (eqs. (1.18) to (1.20)) can be solved for three unknowns: the Rydberg constant and the $1S$ and $2S$ Lamb shifts. A judicious linear combination of these equations,

$$7\nu_{2S_{1/2}-8D_{5/2}} - \nu_{1S_{1/2}-2S_{1/2}} \simeq \frac{57}{64} cR_\infty + 7L_{8D_{5/2}}/h - \Delta_2/h, \tag{1.21}$$

allows to directly determine the Rydberg constant.

1.2.3 The proton radius puzzle

Using the type of calculation sketched above, we can deduce an experimental value of the $1S$ Lamb shift. In this way, a value of the proton charge radius r_p can be inferred from hydrogen spectroscopy, if we assume that the QED calculations are correct. To test the bound-state QED calculations, an independent determination of the proton radius r_p is needed.

Such a value can be obtained from electron-proton scattering experiments. In a typical experiment, electrons are sent onto a thin dihydrogen target and the scattering cross-section is measured. This scattering cross-section can be expressed in terms of form factors from which the proton radius is deduced. The data analysis is very complicated. An equivalent definition of the proton radius involves the derivative of the electric form factor at zero momentum transfer, but the electrons must have sufficient energy to go through the target and avoid multiple scattering. This requires to extrapolate the form factor to low energy with an unknown function, and the difficulty of this analysis leads to a large uncertainty (about 2 %) on the resulting proton radius. The current CODATA value of the proton radius was obtained by including the latest results from e-p scattering into the global adjustment, along with hydrogen and deuterium spectroscopic data.

Another way to determine r_p is the spectroscopy of muonic hydrogen. A muon is exactly similar to an electron except for its mass m_μ which is 207 times higher than that of the electron. For S states, the wavefunction of the muon is more localized and has a greater overlap with that of the proton, so that proton size effects are magnified. In fact, the proton size contribution represents 1.8 % of the $2S-2P$ Lamb splitting in muonic hydrogen, as compared to a proportion of 0.014 % in electronic hydrogen. This fact makes it possible to obtain a very precise determination of the proton charge radius without requiring as much effort on the precision of the spectroscopy as in electronic hydrogen. Direct spectroscopy of the muonic hydrogen $2S-2P$ splitting at 6 µm yields a value of the proton radius that is independent from the Rydberg constant determination.

An experiment to this purpose was set up starting in 1999 at the Paul Scherrer Institute in Switzerland by an international collaboration called CREMA (Charge Radius Experiment on Muonic Atoms) which includes members of our group. After several beam times in 2002, 2003, and 2007, the $2S_{1/2}^{F=1}-2P_{3/2}^{F=2}$ transition was finally observed in 2009. However, it was strangely shifted from the value predicted by the

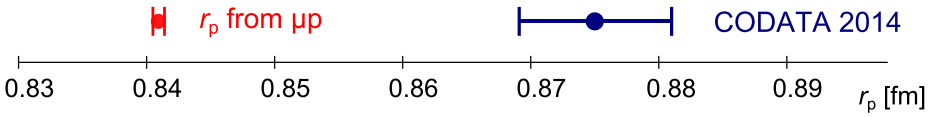

Figure 1.4: The proton charge radius puzzle.

theory [Pohl2010]. The resulting proton charge radius [Antognini2013],

$$r_\mathrm{p} = 0.84087(39)\ \mathrm{fm}, \tag{1.22}$$

is an order of magnitude more precise, but about 4 % smaller, than the current CODATA value[3] [Mohr2016],

$$r_\mathrm{p} = 0.8751(61)\ \mathrm{fm}. \tag{1.23}$$

Conversely, this "small" value of the proton radius can be used to infer a determination of the Rydberg constant. The Rydberg constant obtained in this way is about 105 kHz smaller that the value from the latest CODATA adjustment.

This discrepancy, which has become known as the "proton radius puzzle", has not been explained yet, despite an intense research activity both in theory and experiment [Carlson2015]. The results of the muonic deuterium spectroscopy, which had also been performed in 2009, have recently been published [Pohl2016], deepening the puzzle by introducing a similar discrepancy on the deuteron radius.

Several transitions of muonic helium ions ($\mu^3\mathrm{He}^+$ and $\mu^4\mathrm{He}^+$) have also been measured by the same collaboration in 2013, but the results have not yet been published. The spectroscopy of these hydrogenoid systems is useful to test theories that attempt to explain the proton radius discrepancy.

Solving this puzzle requires new data from electronic hydrogen spectroscopy and e-p scattering. On the spectroscopy side, several experiments are under way for this purpose. The group of E. A. Hessels in Toronto aims at a new[4] direct measurement of the $2S_{1/2} - 2P_{1/2}$ Lamb splitting of hydrogen. In Garching, the group of T. W. Hänsch now studies the $2S - 4P$ transition [Beyer2017], as well as the $1S - 3S$ transition [Yost2016]. Our current $1S - 3S$ experiment also pursues this goal.

The $1S - 3S$ transition frequency predicted by the theory differs by about 7 kHz depending on whether the proton radius from the CODATA adjustment, or from the muonic experiments, is used in the calculations. Therefore, we need to measure this frequency with an uncertainty in the kHz range in order to contribute to the resolution of the proton puzzle.

[3] Because of this discrepancy, the CODATA task group decided not to include the results from the muonic hydrogen experiment in the 2014 global adjustment.

[4] The most precise direct measurement of this transition dates back to 1981 [Lundeen1981].

1.3 Our $1S-3S$ experiment

After measuring the $2S - nS/D$ transitions with great precision, our team turned to the $1S - 3S$ two-photon transition in the middle of the 1990's. What began as a comparison of the $1S - 3S$ and $2S - 6S$ transition frequencies to measure the Lamb shift [Bourzeix1995] turned into a long-term experiment, refined and improved over time to increase the precision. We are now able to measure the frequency of the $1S - 3S$ hydrogen transition with an uncertainty of a few kHz.

Our experiment is based on the following setup. A 205-nm continuous-wave excitation laser is resonant with a build-up cavity whose axis is collinear with an effusive beam of $1S$ hydrogen atoms. The two-photon $1S - 3S$ transition is detected through the Balmer-α fluorescence ($3S - 2P$) at 656 nm.

1.3.1 The second-order Doppler effect

As previously noted, two-photon transitions are particularly suited for spectroscopy because there is no first-order Doppler effect. However, we need to take into account the second-order Doppler effect.

Imagine a photon of frequency ν encountering an atom moving with velocity v along the same axis. Taking into account relativistic time dilatation, the Doppler-shifted frequency $\nu_\pm$ seen by the atom is

$$\nu_\pm = \frac{1 \pm v/c}{\sqrt{1 - v^2/c^2}}\ \nu, \tag{1.24}$$

where the $\pm$ sign depends on the relative directions of the atom and photon.

Assuming that $v \ll c$, the above equation reduces to

$$\nu_\pm = \left(1 \pm \frac{v}{c} + \frac{v^2}{2c^2}\right)\nu. \tag{1.25}$$

Thus, in the case of two-photon spectroscopy with counter-propagating laser beams, an atom will absorb one photon from each beam and the resonance condition is

$$\nu_0 = \nu_+ + \nu_- = 2\,\nu\left(1 + \frac{v^2}{2c^2}\right). \tag{1.26}$$

The first-order Doppler effect has canceled out but there remains the second-order Doppler shift

$$\delta_{\text{Dop.2}} \simeq -\frac{\nu_0 v^2}{2c^2}. \tag{1.27}$$

As we will see in Chapter 3, the velocity distribution of atoms in an effusive beam

can in principle be written as

$$f(v) \propto v^3 \exp(-\frac{v^2}{2\sigma^2}), \tag{1.28}$$

where $\sigma = \sqrt{k_B T/m}$, with T the temperature and m the atomic mass. The most probable velocity in a beam of hydrogen atoms at room temperature ($T \sim 300$ K) is given by $v = \sqrt{3}\sigma \simeq 2.7$ km/s. An atom moving with this velocity would experience a second-order Doppler shift of about 120 kHz. In our experiment, this Doppler shift can thus be expected to be on the order of a hundred kHz and greatly dependent on the velocity distribution, which has to be estimated experimentally.

Several methods could be used to this purpose. One possibility is to directly probe the velocity distribution by monitoring the Doppler broadening of a one-photon transition. This would however be difficult to implement in our case. The lowest one-photon transition from the ground state ($1S - 2P$) requires a 121-nm laser, the building of which represents quite a feat in itself. One could also perform the Doppler spectroscopy measurement from the $2S$ level after populating this state by two-photon excitation of the $1S - 2S$ transition. This solution would also require lasers that are not currently available for our experiment. Another possible method would be to use a beam chopper in order to perform velocity-selective spectroscopy, but this would imply rebuilding the entire experimental setup.

Eventually, in order to characterize the velocity distribution of our atomic beam, we use an original method [Biraben1991] which consists in applying a transverse magnetic field in the interaction region.

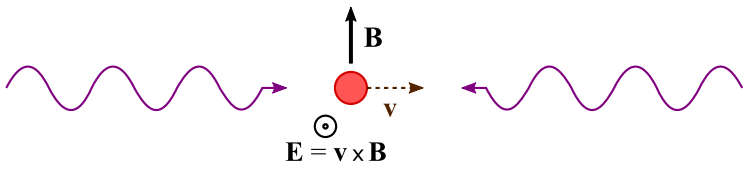

Figure 1.5: The magnetic field **B** and motional electric field **E**.

In the reference frame of the moving atom, the magnetic field **B** creates a motional electric field $\mathbf{E} = \mathbf{v} \times \mathbf{B}$, as shown in Fig. 1.5. The quadratic Stark effect due to this electric field shifts the transition frequency of a quantity

$$\delta_{\text{Stark}} \propto \frac{E^2}{\Delta_{SP}} = \frac{v^2 B^2}{\Delta_{SP}}, \tag{1.29}$$

where Δ_{SP} is the energy difference between the levels coupled by the electric field, which are in our case the $3S_{1/2}$ level and nearest $3P_{1/2}$ level.

This effect is proportional to v^2, like the Doppler shift. The two shifts could thus apparently cancel each other for a well-chosen value of the magnetic field.

However, the magnetic field has another, larger effect on the energy levels: the Zeeman splitting, which lifts the degeneracy of levels of same n, L, J, F quantum numbers and different m_F. This splitting is shown on Fig. 1.6. In our experiment, we study the $1S - 3S(F = 1)$ transition, because the $1S_{1/2}^{F=1}$ level is more populated. Due to the selection rules $\Delta F = 0$ and $\Delta m_F = 0$ for two-photon transitions between levels of same $J = 1/2$ [Grynberg1976], only three sub-transitions are allowed between $F = 1$ levels, as shown on the diagram (Fig. 1.6).

As the $m_F = 0$ sublevels are not shifted in the same way by the Zeeman effect, the transition $1S_{1/2}(F = 1, m_F = 0) \to 3S_{1/2}(F = 1, m_F = 0)$ is much shifted and is used to calibrate the magnetic field.

On the other hand, the other transitions, between levels of $m_F = \pm 1$, are only slightly shifted by the magnetic field. In fact, the Landé factor g_S of the bound electron, which appears in the Zeeman hamiltonian (eq. (3.6) in Chapter 3), differs from the free-electron g-factor g_e because of relativistic effects. It is given by [Bethe1957, Cesar2001] as

$$g_S(n) = g_e \left(1 - \frac{3\alpha^2}{n^2}\right), \tag{1.30}$$

yielding for the $1S$ and $3S$ levels:

$$\begin{aligned} g_S(1S) &= 2.00228376, \\ g_S(3S) &= 2.00231535. \end{aligned} \tag{1.31}$$

Figure 1.7 shows the theoretical position of the $1S - 3S(F = 1, m_F = \pm 1)$ transitions, as a function of the magnetic field. For a magnetic field of about 180 G (18 mT), the Zeeman effect causes a level crossing between the $3S_{1/2}(F = 1, m_F = -1)$ and $3P_{1/2}(F = 1, m_F = 0)$ sublevels. The quadratic Stark effect is thus large for the $1S - 3S(F = 1, m_F = -1)$ sub-transition and compensates the second-order Doppler shift for two values of the magnetic field, labeled A and B on curve (c) of Fig. 1.7. For the same magnetic field, the $3S_{1/2}(F = 1, m_F = +1)$ sublevel is far from any level of opposite parity and is not displaced by the quadratic Stark effect (curve (a)).

However, both the Doppler and Stark shifts are much smaller than the natural linewidth of the transition (1 MHz), so that the two sub-transitions are not distinguished in our experiment. Hence, the apparent displacement (curve (b)) is the average of the two former curves, and the Doppler effect is only partially compensated.

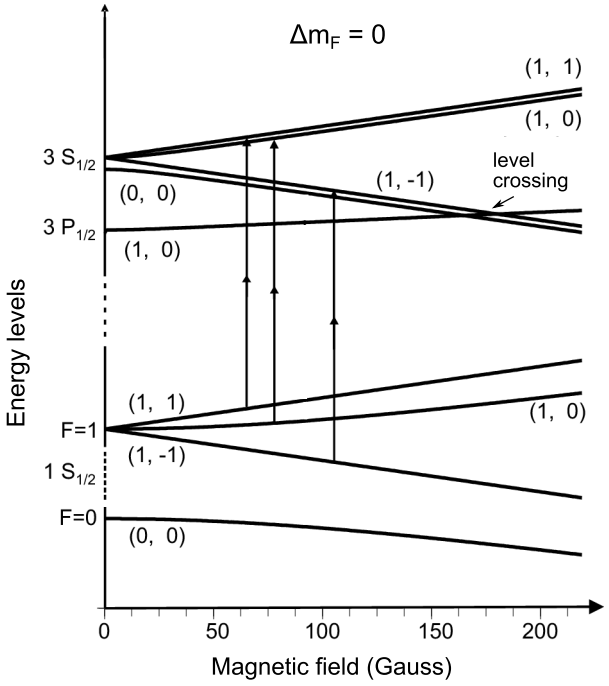

Figure 1.6: Zeeman splitting diagram. The levels are labeled by the quantum numbers (F, m_F). The $3S_{1/2}(F = 1, m_F = -1)$ sublevel crosses the $3P_{1/2}(F = 1, m_F = 0)$ sublevel for a magnetic field of about 180 G.

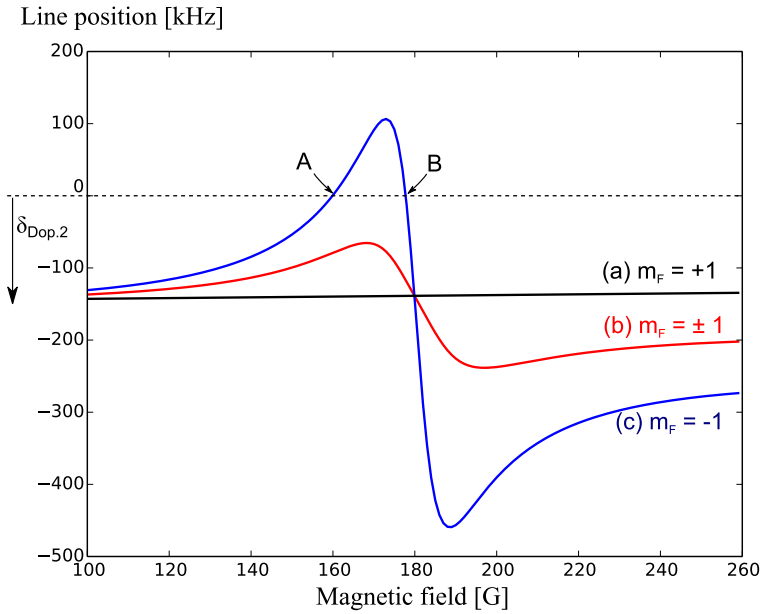

Figure 1.7: Theoretical position of the $1S - 3S(F = 1, m_F = \pm 1)$ lines as a function of the magnetic field, calculated for an atomic velocity of $v = 3$ km/s. Thanks to the motional Stark effect, the second-order Doppler effect is compensated at points A and B for the $m_F = -1$ sub-transition (curve c). However, the $m_F = +1$ sub-transition is not shifted by the Stark effect (curve a). In practice we observe both sub-transitions (curve b).

To estimate the velocity distribution of the atoms, we record transition signals for various values of the magnetic field, and fit them with a theoretical line profile that takes into account both the second-order Doppler shift and the Stark effect used to compensate it [Hagel2001].

1.3.2 Experimental improvements

Since it began in 1995, our $1S-3S$ experiment has evolved over time, each Ph.D. student bringing new improvements to the setup. Two of the most striking recent changes involve the excitation laser source and the frequency measurement system.

In order to measure a frequency, it has to be compared to a reference, the absolute frequency reference being the cesium clock transition at 9 192 631 770 Hz which defines the second (hyperfine ground state transition frequency of ^{133}Cs). Moreover, one can more easily compare frequencies separated by a few GHz. Hence, to measure the optical frequency of a laser, it has to be somehow down-converted to the micro-wave domain. In the 1990's, this was done by means of complicated frequency chains. These included several stages in which standard lasers stabilized on atomic transitions were painstakingly frequency-doubled to link the optical domain to the longer wavelengths.

Nowadays, the creation of optical frequency combs, for which J. L. Hall and T. W. Hänsch received the Physics Nobel prize in 2005, has made it much easier to measure optical frequencies. A frequency comb is generated from a pulsed laser, which delivers pulses at a regular period. In the frequency domain, the spectrum presents regularly spaced modes which depend on this period and an offset frequency. The spacing between modes, called the repetition rate, is equal to the inverse of the period. Both the repetition rate and the offset frequency can be stabilized to a frequency reference. To measure an optical laser frequency, one simply has to measure the frequency of the beat note between the unknown laser and one of the comb modes.

Olivier Arnoult implemented such a laser during his Ph.D. [Arnoult2006]. We now use another, similar frequency comb to measure the frequencies of the various lasers in our experiment. The principle of this measurement will be described in part 2.3.

Another major improvement to the setup concerns the excitation laser source. Creating a powerful continuous light source at 205 nm is a challenge in its own right. Until 2010, the team used two successive doubling stages, starting from a continuous-wave titanium-sapphire laser at 820 nm. This infrared laser was first frequency doubled to 410 nm by second harmonic generation (SHG) in a lithium

triborate (LBO) crystal. The blue light was itself doubled again in a β-baryum borate (BBO) crystal to generate the 205-nm excitation light.

The first doubling stage was quite efficient [Bourzeix1993]. However, the second doubling stage had a very low conversion efficiency because the BBO crystal was used at the limit of its phase-matching angle for SHG. In fact, due to photo-refractive effects in the crystal, it could only be used in quasi-continuous operation, producing less than 0.1 mW of 205-nm radiation [Bourzeix1997]. The resulting power modulation created a distorted signal that was hard to analyze [Hagel2002].

During her Ph.D. work starting in 2012, Sandrine Galtier built a new 205-nm laser source based on sum frequency generation (SFG), which will be presented in detail at the beginning of Chapter 2. Light from the same titanium-sapphire laser, modified to emit 894-nm radiation, is combined with 266-nm laser radiation in a BBO crystal to generate a 205-nm beam. For SFG, the phase-matching angle limit of the BBO crystal is further in the ultraviolet. This setup is thus more favorable than SHG and enables continuous-wave operation. Hence, we can now obtain more than 10 mW of continuous-wave 205-nm light.

This new source has another advantage: it will allow us to reach the $1S-4S$ two-photon transition, which lies even further in the UV, at 194 nm. To produce this wavelength, we will simply have to shift the titanium-sapphire operating wavelength to 724 nm.

1.3.3 Previous results and perspectives

The $1S-3S$ transition frequency was measured in 2010 [Arnoult2010] with a relative uncertainty of 4.4×10^{-12}, with the following centroid value,

$$\nu_{1S-3S} = 2\,922\,743\,278.678(13)\ \text{MHz}. \tag{1.32}$$

Major improvements on the 205-nm laser source allowed Sandrine Galtier to record new data in 2013-2014. The analysis yielded an encouraging statistical uncertainty of 2.1 kHz, but it was hindered by the determination of the velocity distribution. A correct estimation of this distribution, and thus of the second-order Doppler effect, is essential to our measurement.

One of the important systematic effects in the experiment is the pressure shift. Determining it involves measuring the transition frequency for several pressure values and extrapolating to zero pressure. Unfortunately, the magnetic field analysis to estimate the velocity distribution was done only for one value of the pressure. The model used to describe this distribution was refined during the data analysis, and

could include a possible pressure dependence (see Chapter 3, part 3.1.2 for more details).

Therefore, one could either assume that the velocity distribution did not depend on the pressure, or that it did. In the first case, one obtained a frequency value in agreement with the CODATA theoretical value; in the pressure-dependent case, the result agreed fairly well with the prediction of the muonic proton radius [Galtier2015]. It was impossible to conclude without better knowledge of the velocity distribution of the atomic beam.

At the beginning of my Ph.D., the first thing to do was thus to estimate the atomic velocity distribution for different pressure values in order to validate the pressure-(in)dependent model. This has been done successfully, along with a complete study of other systematic effects, and the results will be presented in this manuscript. Another possible research direction is to cool the hydrogen atoms down to cryogenic temperatures in order to reduce their velocity. This would render our measurement much less sensitive to the second-order Doppler effect. The cooling system has been installed at the very end of my Ph.D.

I will describe the experimental setup in detail in Chapter 2, then give in Chapter 3 a theoretical presentation of the systematic effects that must be taken into account, before the data analysis and results in the last chapter.

Chapter 2

The $1S-3S$ experimental setup

In the first chapter I have presented our experiment from a historical and theoretical point of view. The present chapter is devoted to the experimental setup currently used to measure the $1S-3S$ transition frequency. The overall goal of this experiment is to determine this frequency with the smallest uncertainty, which is achieved with the best signal-to-noise ratio for the observed atomic transition.

The setup, represented very schematically in Fig. 2.1, comprises two laser sources which provide, through second-harmonic generation (SHG) and sum frequency generation (SFG), the 205-nm radiation for the two-photon excitation of the hydrogen atoms. The frequency of the lasers is stabilized and can be measured with the help of a frequency comb. The $1S-3S$ transition is detected by collecting the Balmer-α ($3S-2P$) fluorescence.

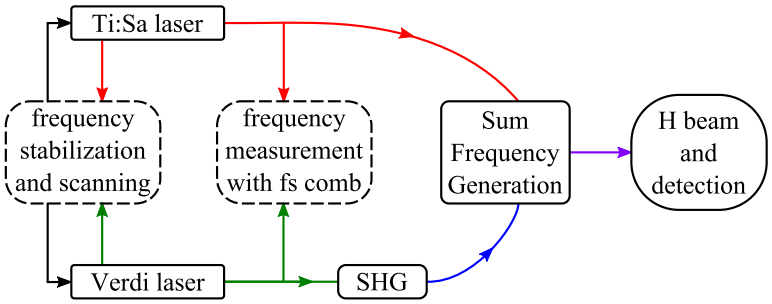

Figure 2.1: Schematic diagram of the laser setup.

I will first describe our 205-nm laser source, and how its frequency can be stabilized and measured. Then we will turn to the atomic hydrogen beam and fluorescence detection. I will also present the coils used to produce the magnetic field necessary for the determination of the second-order Doppler shift. A final part is devoted to the data acquisition and observed signals.

2.1 The 205-nm laser source

Our experiment requires a continuous-wave, tunable, frequency-stabilized laser source at 205 nm. The current excitation laser source at 205 nm was build by Sandrine Galtier [Galtier2014a]. The continuous 205-nm light is obtained by sum frequency generation (SFG) from a titanium-sapphire laser at 894 nm and a 266-nm radiation provided by the frequency doubling of a 532-nm laser.

2.1.1 The titanium-sapphire laser

Our continuous-wave (cw) tunable titanium-sapphire (Ti:Sa) laser is a home-made laser developed in our team following a scheme proposed by François Biraben [Biraben1982]. It has been well described in [Bourzeix1993]. Here I will present its main characteristics.

The amplifying medium is a Brewster-cut Ti:Al_2O_3 crystal, which is pumped by 13 W of 532-nm light from a frequency-doubled Nd:YVO_4 laser (Millennia® XV from Spectra Physics). It has great versatility, and can be used over a wide range of wavelengths. In its current configuration, this Ti:Sa laser delivers about 1.6 W of 894-nm radiation.

Figure 2.2 shows the optical ring cavity of this laser. The infrared light is linearly polarized in the horizontal direction. In a ring cavity, both directions of light propagation are in principle allowed. To ensure that only one direction of lasing is allowed, this cavity contains two elements which rotate the polarization of the laser beam. One is a Faraday rotator. This birefringent plate, placed in a magnetic field, turns the polarization of an angle independent from the direction of propagation, because the rotation direction is imposed by the magnetic field. The other element is the mirror system M4-5-6, with mirror M5 placed above the two others, that generates a polarization rotation of an equivalent angle but whose sign depends on the propagation direction. The two polarization changes compensate for one lasing direction but add up for the other. The presence of other polarization-selective elements in the cavity (e.g. plates placed at Brewster angle) creates losses for the latter direction, thus preventing the laser from operating in that direction.

To enable single-mode operation, the Ti:Sa cavity also contains three frequency-selective elements, which are listed here in order of increasing selectivity:

- the Lyot filter, composed of three birefringent plates that can be rotated via a servo motor, selecting a 0.5 Å wavelength range;
- the thin etalon, a silica plate that acts like an interferometer and whose orientation with respect to the laser beam can be adjusted with a servo motor;

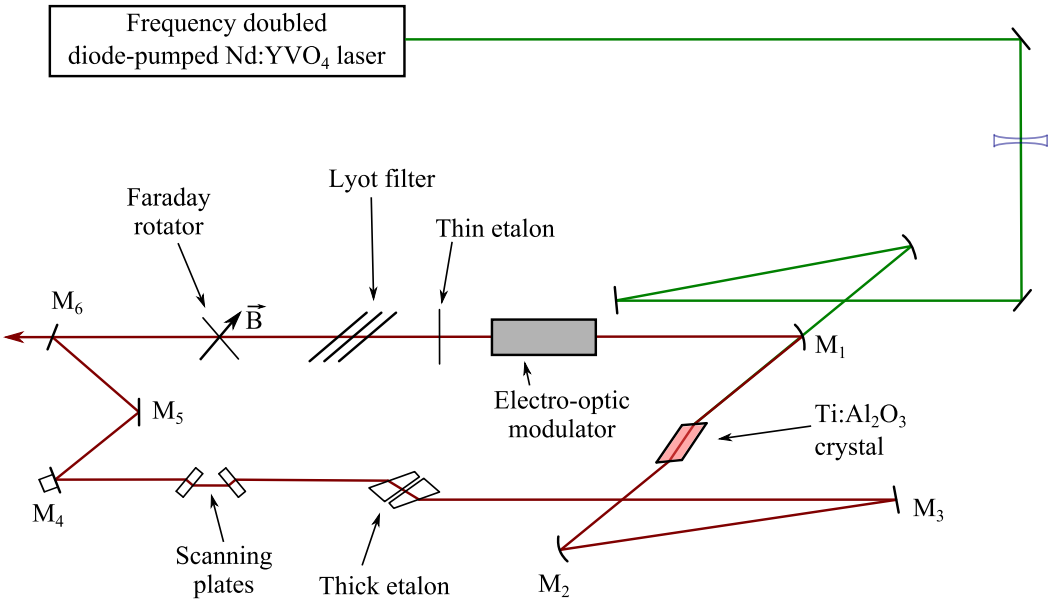

Figure 2.2: The optical setup of the Ti:Sa laser.

- and the thick etalon, a Fabry-Perot cavity formed by the air gap between two prisms. One of these prisms is piezo-mounted, allowing to tune the frequency range selected by this etalon.

Finally, the scanning plates, which can be moved symmetrically, are used to modify the optical length of the laser cavity and tune the laser frequency on a large range. It can also be tuned using the piezo-mounted M4 mirror, and an electro-optic modulator is used for more rapid frequency control (see stabilization description in part 2.2.2).

2.1.2 The frequency-doubled Verdi laser

Our 532-nm laser is a frequency-doubled Nd:YVO_4 laser developed by Coherent® (Verdi V6 model). The frequency of this single-longitudinal-mode laser can be controlled by means of a piezo-mounted mirror in the laser resonator. This mirror is actually mounted on a piezoelectric stack with two channels, a slow one for large translations and a rapid one for smaller fluctuations. We have added a double-pass acousto-optic modulator (AOM) at the output of the Verdi laser to further correct the rapid frequency fluctuations of the laser, as explained in part 2.2.2.

We use an off-the-shelf doubling cavity (MBD266, also from the Coherent firm) to perform second harmonic generation in a β-baryum borate (BBO) crystal. The length of this cavity is locked on the laser frequency by the method of Hänsch-Couillaud [Hänsch1980], which will be described in the next section. We have been using the same BBO crystal since the beginning of Sandrine Galtier's Ph.D. However, we have

recently removed the output monitoring plate of the MBD266 cavity in order to increase the output power.

Injecting 1.2 W of 532-nm light into the cavity, we obtain about 250 mW of radiation at 266 nm.

2.1.3 Sum frequency generation

The sum frequency generation (SFG) system consists in two ring cavities that overlap in a β-baryum borate (BBO) crystal [Berkeland1997, Galtier2014b]. The actual geometry of the cavities is shown in Fig. 2.3.

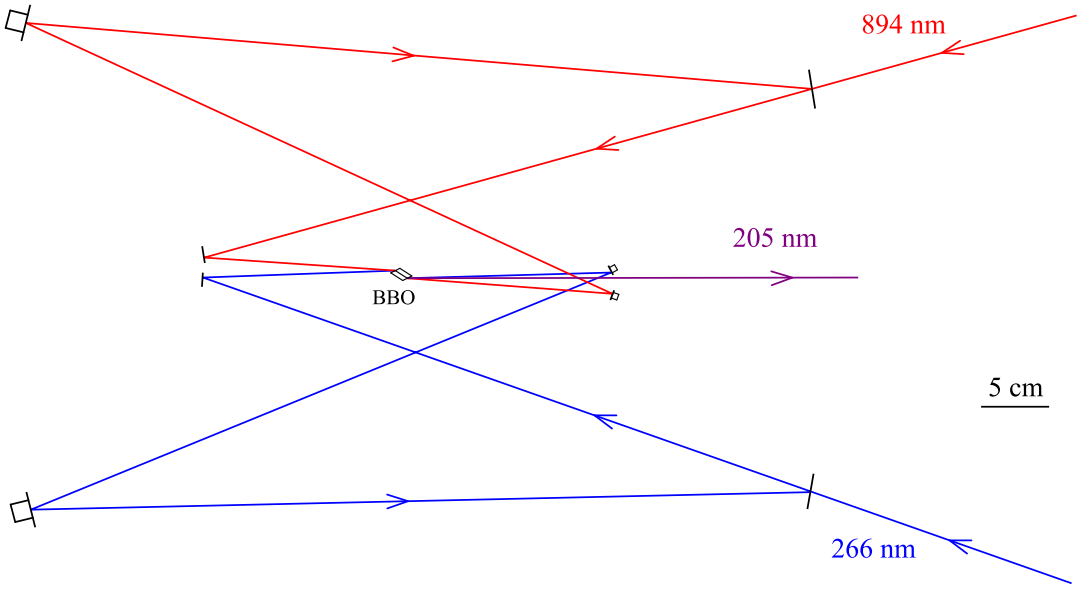

Figure 2.3: Geometry of the sum frequency generation cavities. Two mirrors of each cavity are piezo-mounted to lock the cavity length on the laser frequency.

The initial beams at 894 nm and 266 nm are shaped using lenses to improve the mode-matching to their respective cavity. The BBO crystal is Brewster-cut for the 894-nm beam in order to minimize the losses for this frequency. Its temperature is stabilized at 40 °C to prevent water absorption. At the output, a cylindrical lens corrects the asymmetry of the 205-nm beam profile.

Both cavities are locked on the laser frequencies through a Hänsch-Couillaud locking scheme [Hänsch1980]. This method relies on the presence of a polarization-selective element inside the cavity, in our case the Brewster-cut BBO crystal which creates losses for vertically-polarized light. The polarization of the incoming light is slightly tilted from the horizontal direction. The vertically-polarized part of the laser beam is reflected by the input mirror of the cavity, whereas the horizontally-polarized beam propagates inside the cavity and the phase of the outgoing beam depends on the cavity length. If the cavity is resonant with the laser frequency, the reflected and

outgoing light beams are in phase. By comparing the respective phases of the those two beams, we can build a dispersion-shaped error signal to perform a retroaction on two piezo-mounted mirrors in each cavity: a small one for rapid length fluctuations and a large one for slower, larger corrections. The advantage of this method is that it does not imply modulating the frequency of the radiation inside the cavity, thus avoiding an unwanted broadening.

Any absorbing substance in the cavity has a large impact on the power enhancement and the SFG efficiency. Sandrine Galtier pointed out that water molecules absorb the 894-nm light from the Ti:Sa laser. Preventing this absorption required the use of a dry air flow. Moreover, I discovered fortuitously that acetone vapor absorbs 266-nm light. Indeed, by placing an acetone-soaked tissue near the 266-nm light beam, we can even see the acetone fluorescence, which has been studied elsewhere [Bryant2000]. We now avoid cleaning the 266-nm mirrors with acetone, and prefer *n*-hexane, that we also use to clean the BBO crystal. Also, to avoid the presence of unwanted molecules, we replaced the dry air flow by a nitrogen flow, recycling the nitrogen evaporating from the liquid-nitrogen trap of our diffusion pump.

Day to day we obtain more than 10 mW of 205-nm radiation. The power sometimes drops sharply due to a photorefractive effect in the BBO crystal. A similar effect was observed during the Ph.D. of Gaëtan Hagel when the 205-nm light was produced by second harmonic generation in a BBO crystal, but it was even more hindering since it prevented continuous-wave operation [Hagel2001]. The 266-nm light triggers the formation of color centers in the crystal. Any stray reflection can cause the formation of a refractive index grating in the crystal, that diffracts the 266-nm beam. The 266-nm light starts propagating in the wrong direction around the ring cavity, reducing the power enhancement and thus the efficiency of the SFG process. In an attempt to prevent the apparition of this effect, we place the BBO crystal in a flow of oxygen. Besides, the effect is localized and partly reversible, so that moving the crystal laterally for a few minutes allows to recover a more normal output power. However, the BBO crystal ages nonetheless and has to be changed every few months.

2.2 Frequency stabilization and scanning

In order to achieve frequency stability of this 205-nm source, it is necessary to ensure the stability of both initial lasers (Ti:Sa and Verdi). The stabilization scheme involves sequential locks onto several Fabry-Perot cavities, and requires the presence of an additional standard laser used as a frequency reference. I will first present this standard laser, then turn to the description of the locking process for the Ti:Sa and Verdi lasers.

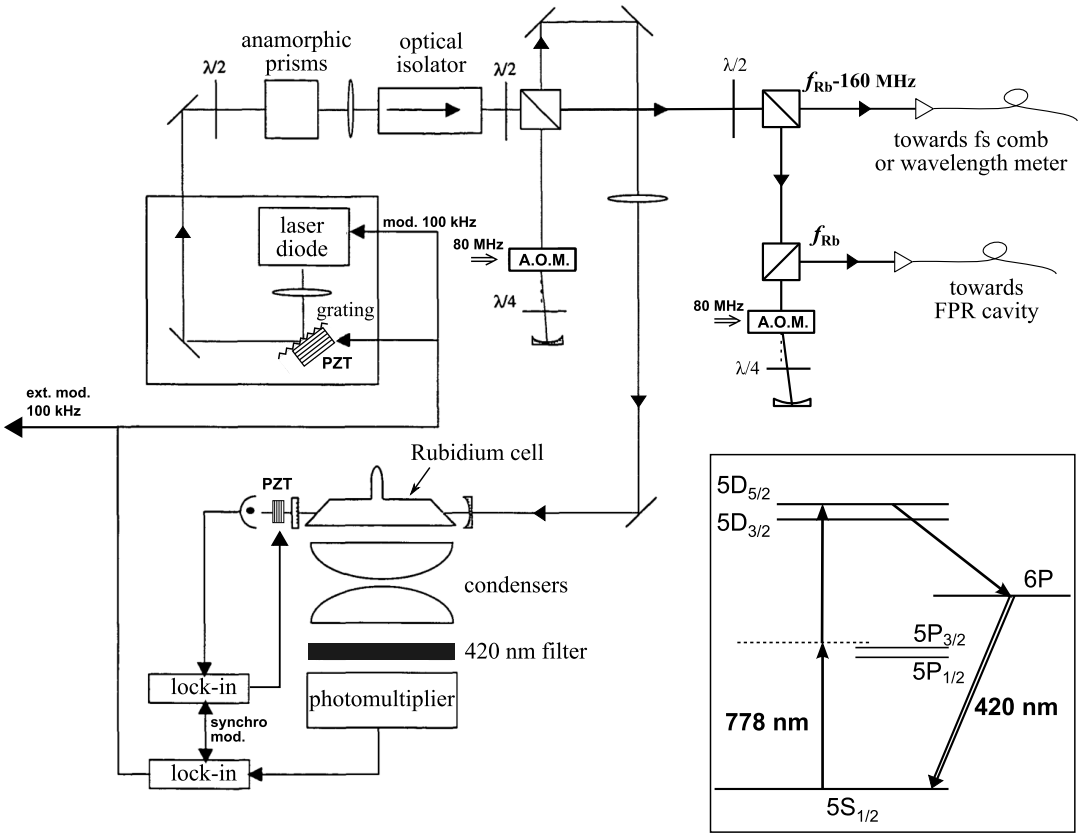

Figure 2.4: Optical setup of the standard laser. The inset shows the $n = 5$ rubidium energy levels and the relevant transitions. The 778-nm diode drives the two-photon $5S_{1/2}^{F=3} - 5D_{5/2}^{F=5}$ transition of ^{85}Rb. The atoms subsequently decay via the $6P$ level, and the $6P - 5S$ fluorescence at 420 nm is detected by the photomultiplier. The laser diode represented in this drawing is in an extended-cavity configuration using a piezo-mounted grating as the tuning element. It was replaced during my Ph.D. by a new diode whose extended cavity consists in a piezo-mounted mirror and an interference filter [JANNIN2015].

2.2.1 The rubidium-stabilized standard laser

The standard laser was developed, partly by our team, at the end of the 1990's, and is well described in [DEBEAUVOIR1997]. This 778-nm tunable extended-cavity laser diode is stabilized on the two-photon $5S_{1/2}^{F=3} - 5D_{5/2}^{F=5}$ hyperfine transition of ^{85}Rb. The drawing of Fig. 2.4 gives an overview of the optical setup of this laser.

Part of the laser beam is injected in a Fabry-Perot cavity after passing through a double-pass acousto-optic modulator (AOM), which acts as an optical isolator between the cavity and the diode. Initially, this AOM served a more important role: it was used to stabilize the light power seen by the Rb atoms in order to control the light shift. Nowadays, this power control is not needed anymore. Since we are able to measure the frequencies very precisely thanks to our frequency comb (part 2.3), the absolute frequency of this laser does not matter, only its long-term stability.

The cavity contains a rubidium cell, and the length of the cavity is locked onto the incident laser frequency to keep it resonant. The 420-nm fluorescence resulting from the decay of the ^{85}Rb atoms (see Fig. 2.4) is monitored via a photomultiplier. The frequency of the diode is locked to maximize the fluorescence signal, using both the diode current and the piezo-actuator of the grating forming the extended cavity.

Both locks (cavity length and diode frequency) use lock-in amplifiers that share the same 100-kHz modulation.

The other part of the laser beam is then separated in two by a polarizing beam-splitter. One beam is used for frequency measurement, either using a wavelength meter or making a beat with the frequency comb, as described in section 2.3.3. The other beam passes through another double-pass AOM before being sent, via an optical fiber, to the reference Fabry-Perot cavity (FPR), the use of which is explained in the following section.

2.2.2 Ti:Sa and Verdi frequency stabilization

Figure 2.5 offers a general view of the stabilization scheme. The Ti:Sa and Verdi laser frequencies are both stabilized in a similar manner.

First, to correct rapid frequency fluctuations (jitter), the laser cavity length is locked on a resonance of an auxiliary Fabry-Perot cavity. There are two such cavities, one for each laser, that we will call $\mathrm{FPA_{Ti:Sa}}$ and $\mathrm{FPA_{V6}}$.

Both cavities are composed of a 25-cm-long invar bar and two mirrors, one of which is piezo-mounted. They are placed inside heavy cylinders to reduce acoustic perturbations. The finesse of the $\mathrm{FPA_{Ti:Sa}}$ cavity is on the order of 100, that of the $\mathrm{FPA_{V6}}$ cavity is about 400 [Galtier2014a].

The stabilization is done using a Pound-Drever-Hall scheme [Drever1983]. This locking method uses an electro-optic modulator (EOM) to apply a frequency modulation to the light beam before the entrance of the cavity. The two sidebands thus created are not resonant with the cavity, but are reflected in phase if the laser is resonant. We monitor the reflected light using a photodiode and, by mixing its signal with the modulation driving the EOM, we obtain an error signal which presents a very steep dispersion shape.

For the Ti:Sa laser, this error signal is used to perform a retroaction on the piezo-mounted M4 mirror and the electro-optic modulator in the Ti:Sa cavity. For the Verdi laser, it acts on the two piezo-actuators in the Verdi laser cavity.

In the case of the Verdi laser, the error signal is also used to modulate the frequency applied to the double-pass acousto-optic modulator (AOM) placed at the output of the laser. This additional correction, having a greater bandwidth than the piezo actuators, allows to reduce the rapid frequency fluctuations and the spectral width of the laser.

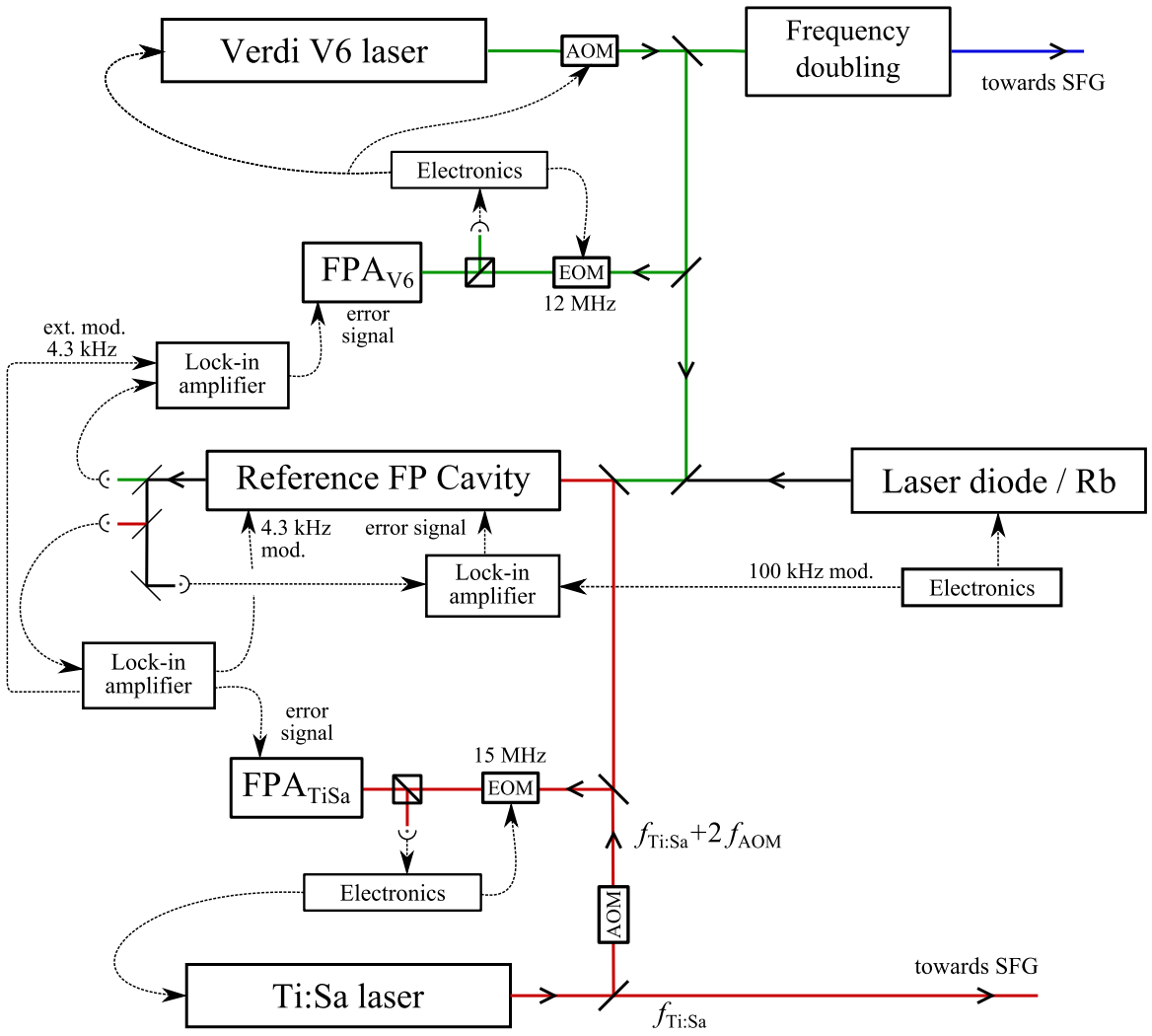

Figure 2.5: General scheme of the frequency stabilization system. Three different laser beams are injected in the FPR cavity. At the output of the cavity, the transmitted light beams are separated using both polarization and wavelength properties. The 778-nm beam is vertically polarized while the others are horizontally polarized. The 532-nm light is first separated from the longer wavelengths using a dichroic mirror. Then the 894-nm and 778-nm radiations are distinguished using a polarizer and a mirror.

Secondly, the length of both FPA cavities is servo-locked on a third Fabry-Perot cavity (reference Fabry-Perot or FPR) to prevent long-term drifts. The FPR cavity, which is maintained under vacuum, is composed of two mirrors separated by a 50-cm-long zerodur bar. The silver-coated metallic mirrors are reflecting for a large range of wavelengths, in the visible and near-infrared. Both mirrors are optically adhered. The input spherical mirror is adhered directly onto the zerodur bar, but the output plane mirror is mounted on a deformable parallelogram system which is piezo-actuated. This allows to tune finely the length of this cavity.

Finally, in order to achieve long-term stability, the FPR cavity length is itself stabilized by maintaining it at resonance with the Rb-stabilized standard laser described in the previous section, also using a lock-in amplifier, thus transferring the high stability of the standard laser to our source lasers. The transmission signals at 778 nm, 894 nm and 532 nm are separated with a combination of dichroic mirrors and polarizing cubes.

2.2.3 Frequency scanning

The presence of a double-pass acousto-optic modulator, operating at frequency f_{AOM}, between the Ti:Sa laser and the Fabry-Perot cavities entails a frequency difference of $2 \times f_{\mathrm{AOM}}$ between the direct laser beam and the frequency $f_{\mathrm{Ti:Sa}}^{\mathrm{FPR}}$ of the FPR resonance on which it is locked. If f_{AOM} varies, the Ti:Sa laser frequency is corrected accordingly to keep it resonant with the FPR cavity of fixed length. This allows to modify the UV frequency of a few MHz by changing the value of f_{AOM}, while keeping all lasers stabilized.

More concretely, the frequency of the $1S-3S$ transition can be related to the Ti:Sa and Verdi laser frequencies in the following way:

$$f_{1S-3S} = 2 \times \left[2 \times f_{532} + \left(f_{\mathrm{Ti:Sa}}^{\mathrm{FPR}} - 2 \times f_{\mathrm{AOM}} \right) \right], \tag{2.1}$$

where the first factor of two comes from the two-photon transition, the second from the frequency doubling of the 532-nm laser and the third from the double-pass acousto-optic modulator.

The FPR cavity has a free spectral range (FSR) of about $f_{\mathrm{FSR}} \simeq 299.59$ MHz. Its transmission peaks can be labeled by an integer N, corresponding to a resonance frequency of $N f_{\mathrm{FSR}} + \Phi$, where $\Phi \simeq 110$ MHz is the Fresnel dephasing of the cavity, due to the curvature of the mirrors [Garreau1989].

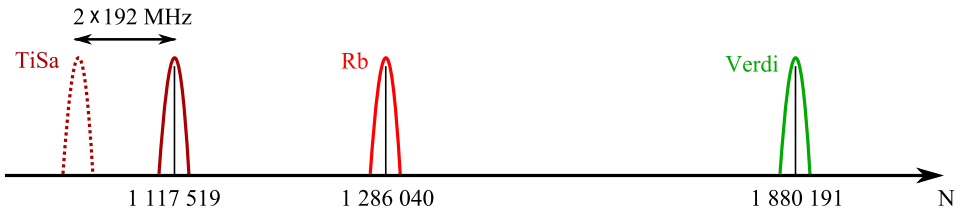

Figure 2.6: Position of the FPR transmission peaks used when aiming at the $1S-3S$, $F=1$ transition of hydrogen. Here N is the number of the FPR transmission peak. The length of the cavity is fixed by maintaining the peak no. 1 286 040 at resonance with the Rb-stabilized standard laser. The frequency of the AOM is set at about $f_{\mathrm{AOM}} \simeq 192$ MHz.

Figure 2.6 shows the respective position, and numbering, of the FPR resonances used for stabilization, when aiming at the hydrogen $1S_{1/2}^{F=1} - 3S_{1/2}^{F=1}$ transition. In this case, the AOM frequency is set at about 192 MHz.

During my Ph.D. work, I also had the opportunity to observe the deuterium $1S-3S$, $F=1/2$ and $F=3/2$ transitions, which are about 800 GHz away from the hydrogen transition. In order to reach these transitions, it is necessary to lock the lasers using other FPR resonances. In practice, we must find the nearest FPR peaks, then adjust the frequency more finely by tuning the AOM frequency. This AOM is optimized for $f_{\mathrm{AOM}} = 200$ MHz, but its frequency can be tuned over a few tens of MHz below this value.

We can also take advantage of the fact that the FPR cavity is itself tunable. Indeed, two adjacent peaks (nos. 1 286 040 and 1 286 041) can be used to lock its length at resonance with the Rb-stabilized standard laser. When aiming at the hydrogen $1S-3S$ transition, the standard laser is at resonance with the FPR resonance no. 1 286 040. For the deuterium transitions, we use peak no. 1 286 041 instead. This corresponds to a change in the cavity length of about 0.39 µm, or a change in FSR of 233 Hz. The Verdi laser is locked on its usual FPR peak no. 1 880 191, whose frequency has shifted by more than 400 MHz due to the FSR change. Figure 2.7 shows the position of the Ti:Sa FPR resonance and the value of the AOM frequency used to aim at the $F=1/2$ and $F=3/2$ transitions of deuterium. The frequency difference between these two transitions is about 315.2 MHz, corresponding to a change in the Ti:Sa frequency of $315.2/2 = 157.6$ MHz.

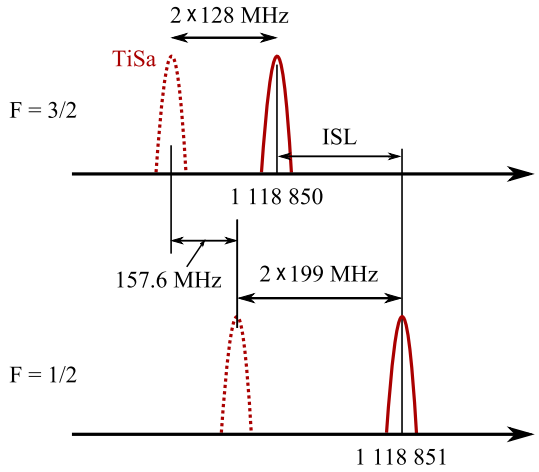

Figure 2.7: Modification of the FPR resonances for the deuterium transitions. The FPR length is now locked by maintaining the transmission peak no. 1 286 041 at resonance with the standard laser, thus changing the cavity length with respect to the configuration used for hydrogen. For each transition, we choose the most convenient configuration of transmission peak number and AOM frequency.

2.3 Frequency measurement

2.3.1 General principle

The frequencies of our cw lasers are measured by means of an optical frequency comb, which is a mode-locked pulsed laser, emitting a coherent train of short pulses. The spectrum of such a laser is composed of many regularly spaced modes, which can be used as a sort of "optical ruler" to determine the frequency of cw lasers.

The comb spectrum can be characterized by two frequencies: the repetition rate f_{rep}, which is the spacing between two adjacent modes, and the carrier-envelope offset (CEO) frequency f_0, which is an overall offset due to the phase difference between two successive pulses. The frequency of a given mode of the comb is given by $f_n = nf_{\mathrm{rep}} \pm f_0$, where n is a large ($\sim 10^6$) positive integer. The $\pm$ sign is due to the fact that the sign of the CEO is not known a priori; by convention, the quantity f_0 is positive. A beat between this mode and a cw laser of frequency f_{cw} will have the frequency

$$f_{\mathrm{beat}} = \pm(f_n - f_{\mathrm{cw}}) = \pm(nf_{\mathrm{rep}} \pm f_0 - f_{\mathrm{cw}}). \tag{2.2}$$

In practice we determine the signs in this equation by modifying the values of f_{rep} and f_0. Our HighFinesse WS7® wavelength meter provides a convenient determination of the cw frequency with a precision of a few tens of MHz. Plugging this into the above equation and inverting it allows us to obtain the value of the integer number n of the nearest mode. Once this is known, it is sufficient to measure the frequency of the beat note to determine the frequency of our cw laser.

2.3.2 The frequency comb

Our frequency comb is a commercial femtosecond (fs) laser made by MenloSystems. It is composed of a mode-locked erbium-doped fiber laser at 1560 nm, that is subsequently fed into two separate amplifiers.

One is a doubling amplifier, whose output at 780 nm is injected in a photonic crystal fiber. Non-linear effects in this fiber broaden the spectrum envelope. The spectral range then ideally spans from about 530 nm to 900 nm.

The other amplifier uses a highly nonlinear fiber to shift the center frequency of the comb spectrum, and provides a high-power (3 mW in 3 nm) fiber-coupled output at 1064 nm.

We benefit from a reference signal sent from the SYRTE[1] department at Observatoire de Paris via a 3-km-long optical fiber link. This 100-MHz signal, referenced to a cesium clock at SYRTE, is used in our laboratory to lock a 10-MHz quartz resonator that serves as an external reference for our frequency counters, synthesizers...

The repetition rate f_{rep} is simply the beat note between two adjacent modes and can be easily obtained using a fast-response photodiode. In order to determine the CEO frequency f_0, our comb uses an interferometric $f-2f$ self-referencing scheme. A non-linear fiber is used to broaden the spectrum so that it spans more than one octave (modes f_n and f_{2n} are contained in the spectrum). The lower-frequency end of the spectrum is then frequency-doubled ($2f_n = 2(nf_{\text{rep}} \pm f_0)$) to make a beat note with the upper end $f_{2n} = 2nf_{\text{rep}} \pm f_0$. The frequency of this beat note is equal to f_0.

The repetition rate and the CEO frequency are both stabilized and referenced to the SYRTE signal.

- The CEO frequency ($f_0 = 20$ MHz) is controlled by acting on the pump diode power. It is directly locked to the frequency-doubled reference signal.
- The repetition rate ($f_{\text{rep}} \simeq 250.1$ MHz) can be modified via the laser cavity length. The fourth harmonic of the repetition rate, down-mixed with a 980-MHz signal, is locked to a signal of about 20.4 MHz provided by a frequency synthesizer referenced to the SYRTE signal. We can thus tune the repetition rate by modifying the frequency of this synthesizer.

Contrary to some other laboratories using this frequency comb model, we use the electronic stabilization system provided by MenloSystems. This may be improved in the next few years to have a better stabilization.

[1] Systèmes de Référence Temps-Espace

2.3.3 The frequency beat notes

An overview of the optical setup used to realize the beat notes is shown in Fig. 2.8. In the following I describe each beat in turn. We measure the frequency of all beat notes using Racal-Dana 1998 frequency counters.

Rb-stabilized standard laser

It is not necessary to know the frequency of this laser for our $1S - 3S$ measurement, but its stable and well-known frequency makes it a good choice as a control of the femtosecond comb operation. The beat note is realized in an optical fiber coupler, with the spectrum-broadened 780-nm output of the frequency comb, narrowed by a very selective band-pass filter whose orientation is adjusted using the Rb standard laser.

The standard laser frequency, averaged over one day of recording (about 14500 1-second points), is given below with the corresponding standard deviation,

$$f_{\mathrm{Rb}} = 385\,285\,142\,370.5 \pm 0.5 \text{ kHz}. \tag{2.3}$$

It differs by a few kHz from previously published values [Touahri1997] because the light shift is no longer carefully controlled.

Ti:Sa laser

This beat is realized in open space using a 50/50 beamsplitter to combine the cw and pulsed beams. The combined beams are then diffracted by a grating to "select" the proper mode of the comb. The beat is made using the direct Ti:Sa laser beam, whose frequency depends on the value of f_{AOM}. In order to count a fix frequency, we mix the RF beat signal with $2 \times f_{\mathrm{AOM}}$. From this measurement, we can then extract the frequency $f_{\mathrm{Ti:Sa}}^{\mathrm{FPR}}$ of the FPR resonance onto which the Ti:Sa laser frequency is locked.

In order to make sure that the frequency is measured in a reliable way, we split the RF signal and measure it simultaneously in two different manners: directly and by using a tracking oscillator, made of a voltage-controlled oscillator (VCO) phase-locked on the beat signal, and measuring the frequency of this oscillator.

Over a typical day, the mean and standard deviation of this measurement is

$$f_{\mathrm{Ti:Sa}}^{\mathrm{FPR}} = 334\,797\,896\,031.2 \pm 1.6 \text{ kHz}. \tag{2.4}$$

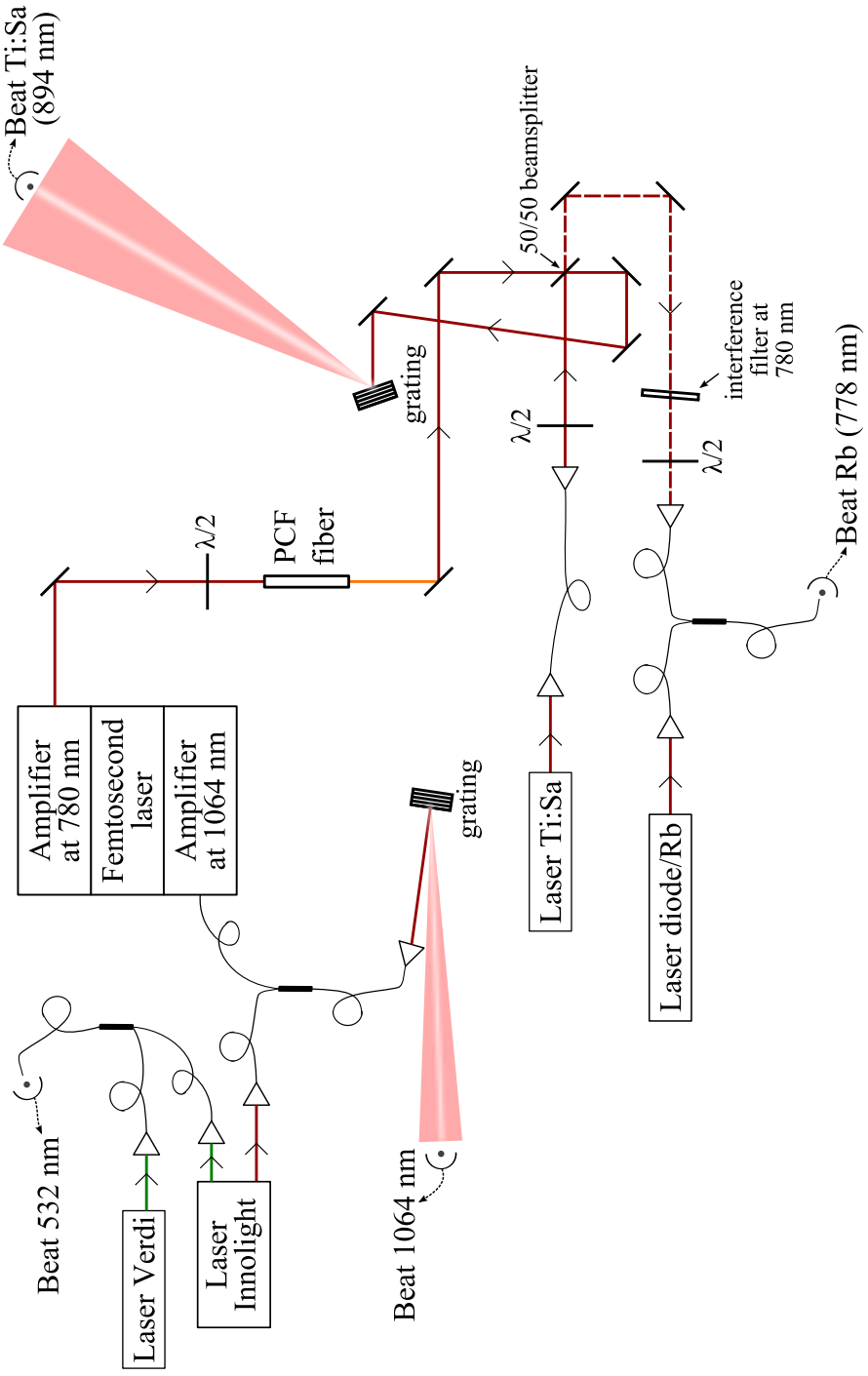

Figure 2.8: Optical system for beat note realization.

Verdi laser

During the Ph.D. work of Sandrine Galtier, one of the limitations of the experiment was the "green" frequency measurement. The frequency of the Verdi laser was measured in the same manner as the reference laser frequency, selecting the green part of the comb spectrum with a 532-nm interference filter and injecting it into a fiber coupler along with the cw beam. However, the beat note obtained in this way was inexplicably broad, and also rather weak (about 20 dB in 1 MHz at the most). Hence, it was difficult to measure its frequency reliably, as our tracking was not able to lock on the broad signal.

We made several attempts to improve the quality of the 532-nm beat note, but to no avail. This beat signal was weak because it was hard to produce enough comb light at 532 nm using the spectrum-broadening photonic crystal fiber (PCF). The same device had to be used simultaneously to produce 894-nm light. To tune the spectrum envelope of the PCF output, the only adjustable parameters are the comb light power and polarization. Since the 532-nm and 894-nm wavelengths are on opposite ends of this spectrum, it is hard to produce both efficiently at the same time. Besides, 532 nm is close to the lowest wavelength that can be reached by this device.

Since it appeared impossible to improve the magnitude of the beat signal, we explored ways of reducing its spectral width. Indeed, it seems that the "green" part of the comb spectrum presents an inherent frequency noise.

We bought a new module allowing to lock the repetition rate directly to a stable 1.55-µm signal, via an electro-optic modulator placed inside the femtosecond laser cavity. This "optical lock" should be more stable and less noisy than the usual "RF lock" (using a frequency synthesizer at 20 MHz). However, after various breakdowns and repairs, we realized that the optical lock of the repetition rate indeed improved the width of the Ti:Sa beat note a little, but had no effect on the green beat note!

We also tried unsuccessfully to obtain 532-nm light from the residual third harmonic produced by the 780-nm doubling amplifier.

As a last resort, we finally settled on a setup which requires the use of an additional "transfer" laser. This cw Nd:YAG laser (Prometheus from Innolight, on loan from Ouali Acef at SYRTE) has two outputs: one output at 1064 nm and another, frequency-doubled output at 532 nm. It has the advantage of having a naturally narrow spectral linewidth of about 1 kHz.

Using this laser, we can make two beat notes. On one hand, we measure the beat note between the 532-nm output of the transfer laser and our own Verdi laser. On the other hand, we also make a beat between the 1064-nm output and the fs comb. By recording simultaneously the frequency of the two beat notes, it is possible to measure

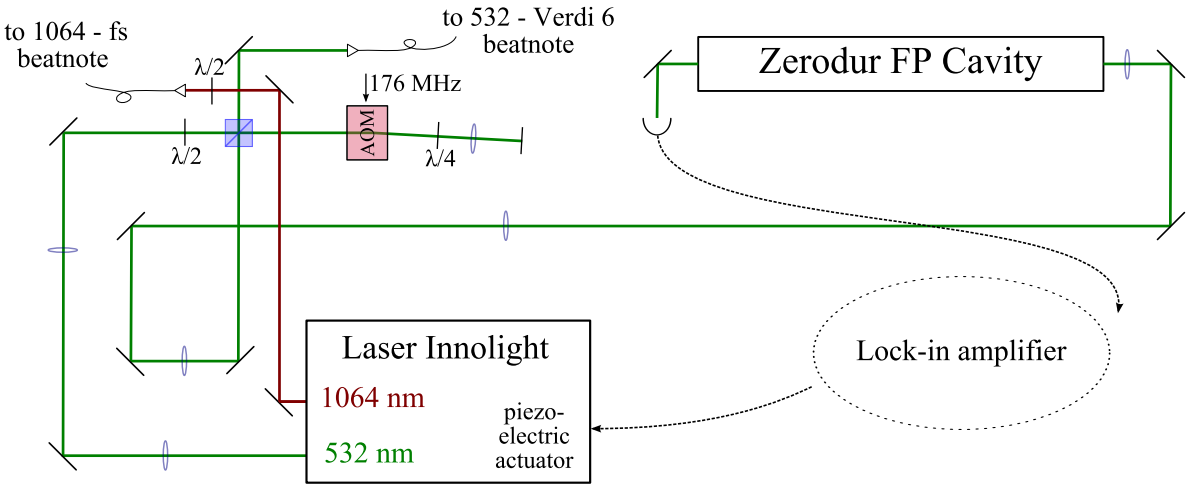

Figure 2.9: Optical setup of the 1064/532-nm transfer laser.

the frequency of our green laser, as can be seen in the following equations,

$$f_{532}^{\text{beat}} = 2f_{1064} - f_{\text{V6}}, \tag{2.5}$$

$$f_{1064}^{\text{beat}} = n_{1064}\ f_{\text{rep}} + f_0 - f_{1064}, \tag{2.6}$$

therefore

$$f_{\text{V6}} = 2\ (n_{1064} f_{\text{rep}} + f_0 - f_{1064}^{\text{beat}}) - f_{532}^{\text{beat}}. \tag{2.7}$$

At first, to check that this solution was feasible, we tried to obtain 1064-nm light from the 780-nm output of the frequency comb using a different spectrum-broadening photonic crystal fiber. We made a beat note between the tiny amount of 1064-nm light we managed to produce and the transfer laser, and were happy to see that this beat note was much narrower than the green beat note! We therefore decided to buy the high power 1064-nm amplifier for this purpose.

Figure 2.9 shows the optical setup of the transfer laser. In a first time, we stabilized its frequency on a 532-nm transition of molecular iodine by a saturated absorption scheme. To do this, I built a setup including a double-pass in an iodine cell (also on loan from SYRTE). However, we later modified this scheme so as to lock the frequency on a resonance of a zerodur Fabry-Perot (FPE) cavity instead. This cavity is very similar to the reference Fabry-Perot (FPR) described in section 2.2.2, except for the fact that its length is not tunable. Because of temperature changes, the frequency of the FPE resonance used in the locking process drifts slowly over a few MHz, but the exact frequency of this laser does not matter for its current purpose.

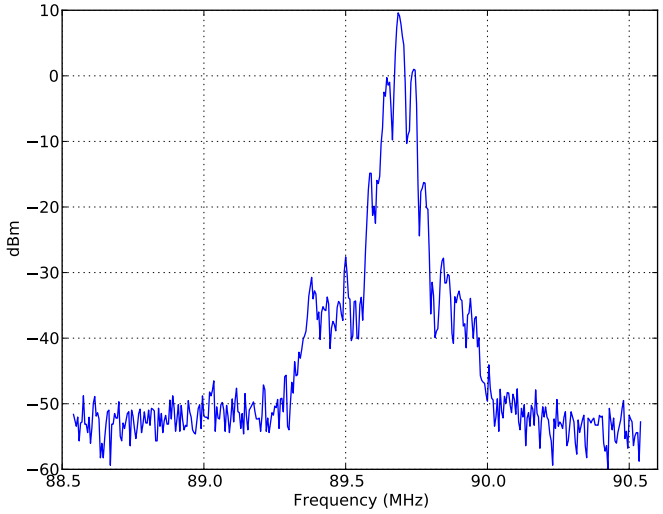

Figure 2.10: Screen shot of the beat note between the two 532-nm lasers (Span 2 MHz, RBW 10 kHz, VBW 10 kHz, no average).

The 532-nm beat note is realized in an optical fiber coupler. Since it involves only narrow cw lasers of reasonable power, this beat is strong and easy to measure. Also, as the transfer laser has a narrower spectral width than the Verdi laser, the beat shows the RF sidebands due to the locking process of the Verdi laser (see Fig. 2.10).

At the beginning of my Ph.D., the observed $1S - 3S$ signals were inexplicably broadened. Using this transfer laser, we saw that the 532-nm beat signal was also broad, indicating that the broadening was due to the spectral width of the Verdi laser. We then investigated and discovered that the piezo-mounted mirror of the $\mathrm{FPA}_{\mathrm{V6}}$ was not well glued and tended to wobble a little, inducing a jitter of the Verdi frequency. After repairing the $\mathrm{FPA}_{\mathrm{V6}}$ and adjusting the gains of the servo-loop, both the 532-nm beat note and the $1S - 3S$ signal recovered a smaller spectral width.

The 1064-nm beat is also done in a fiber coupler, the output of which is diffracted by a grating to select the wavelength. We additionally mix the beat signal with the CEO beat signal from the fs comb to reduce the noise due to the CEO.

Finally, the frequency of the Verdi laser averaged over one day of recording is

$$f_{\mathrm{V6}} = 563\,286\,978\,532.2 \pm 5.6 \text{ kHz}. \tag{2.8}$$

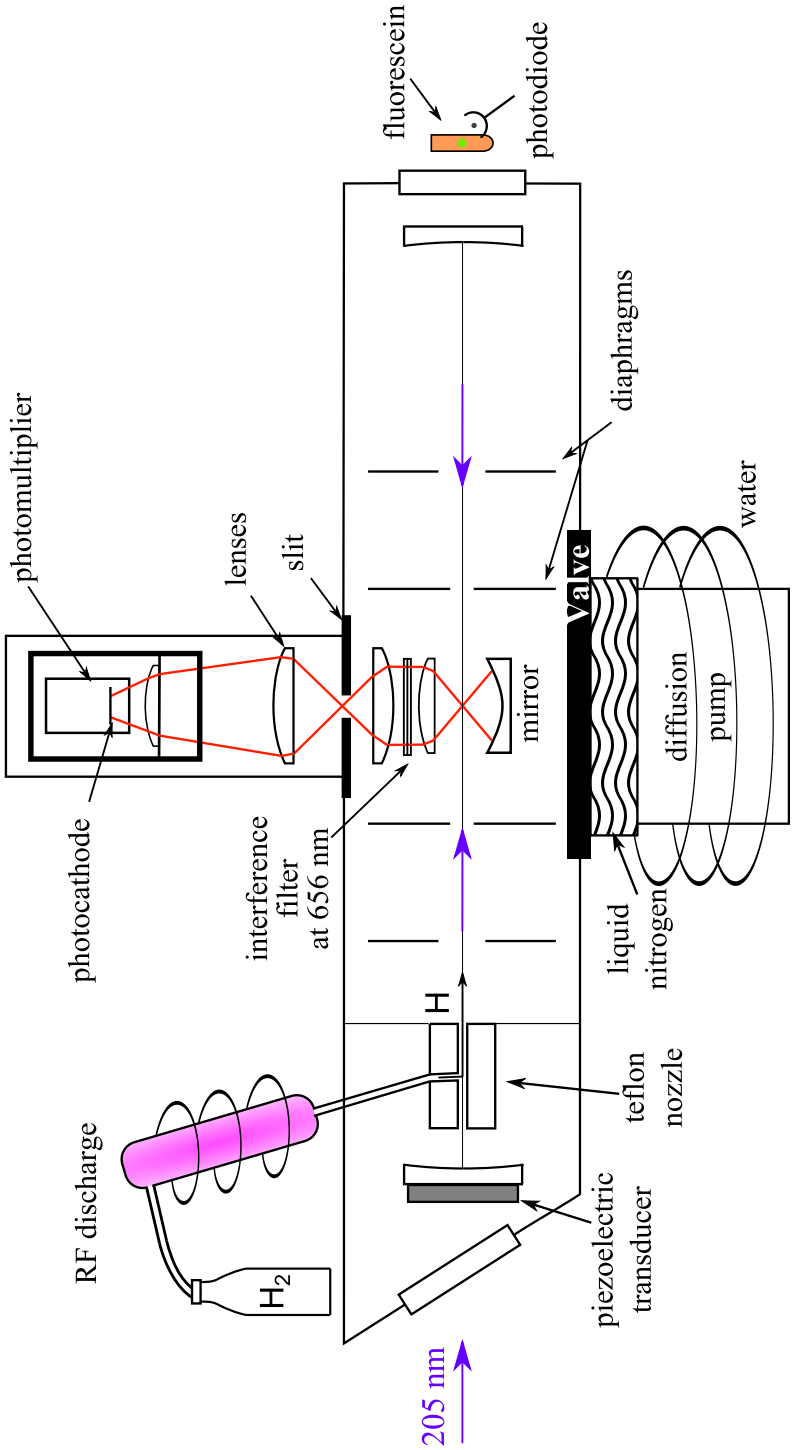

Figure 2.11: General view of the excitation and detection zone.

2.4 Excitation and detection

Figure 2.11 presents a general view of the excitation and detection zone. The frequency-stabilized 205-nm laser beam is injected in a power build-up cavity where it excites the $1S$ hydrogen atoms. The subsequent Balmer-α fluorescence at 656 nm, due to the $3S - 2P$ decay as shown on the level diagram at right, is detected by a photomultiplier.

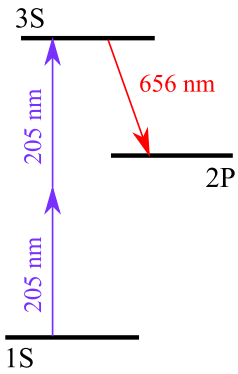

2.4.1 The atomic beam

The hydrogen atoms are produced by a 25-MHz, 40-W radio-frequency discharge in a dihydrogen gas. The highly excited atoms decay rapidly to the ground state and are led to the main vacuum chamber through a Teflon nozzle. The discharge takes place in a pyrex tube that is cooled by circulating water at 14 °C. As shown in Fig. 2.12, the edges of this tube have to be rounded so that the Teflon nozzle fits snugly onto it.

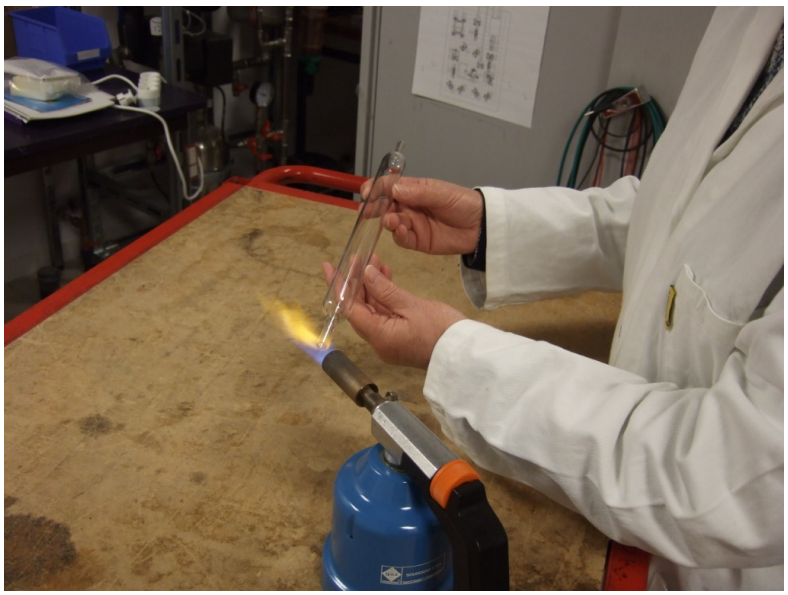

Figure 2.12: Lucile Julien heats the end of the pyrex discharge tube to give the edge a more rounded shape.

We use a Teflon nozzle in order to avoid recombination [Hagel2001]. This nozzle makes a right-angle turn to make the atomic beam collinear with the build-up cavity.

The vacuum chamber is pumped by an oil diffusion pump which is itself pumped by a primary rotary vane pump. A liquid-nitrogen cold trap prevents the oil vapor from reaching the cavity. The oil pump allows to pump hydrogen efficiently while avoiding vibrations which would perturb the lock of the build-up cavity.

The pressure in the vacuum chamber is measured using a Bayard-Alpert ionization gauge, placed on the side of the chamber near the interaction zone. In the absence of hydrogen atoms, we reach a ultimate vacuum of 2×10^{-6} mbar.

Cooling the atoms

The second-order Doppler frequency shift is proportional to the square of the atomic velocity, the average of which is proportional to the temperature. Thus, cooling the hydrogen atoms from room temperature ($\sim$ 290 K) down to liquid nitrogen temperature (77 K) would reduce the second-order Doppler shift by a factor of 4.

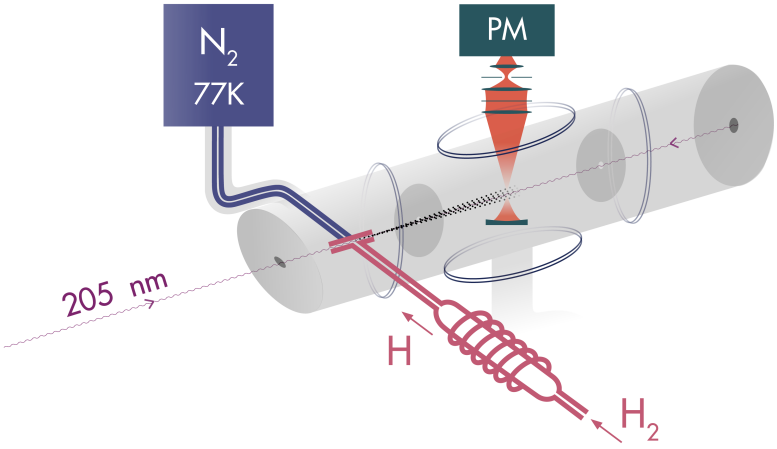

Figure 2.13: Schematic view of the cooling system and power build-up cavity.

We decided to cool the atoms by thermalization with a liquid-nitrogen-cooled nozzle. In the final months of my Ph.D., I installed with Simon Thomas (the following Ph.D. student) the cooling system, a schematic drawing of which is shown in Fig. 2.13. At the time of this writing, the cold nozzle is in place, and after vacuum tests, we have been able to observe the transition for the first time with cooled atoms (see Fig. 4.8 at the very end of this manuscript).

The surface reactions of hydrogen on the nozzle depend on the temperature. Near 77 K, the material that best avoids recombination is no longer Teflon but aluminum, thanks to the formation of a protective oxide layer [Walraven1982]. We also plan to test a copper nozzle, which according to the same reference works best at even lower temperatures.

All the frequency measurements described in the present manuscript were done at room temperature.

2.4.2 The power build-up cavity

The 205-nm excitation laser beam is vertically polarized and enters the vacuum chamber through a silica Brewster window. The two spherical mirrors forming the power build-up cavity have a curvature radius of 25 cm, and are placed 49.3 cm apart, in a quasi-concentric configuration.

The waist w_0 of this Fabry-Perot resonator, which is the beam radius at the center of the cavity, is defined by

$$w_0^2 = \frac{\lambda}{2\pi}\sqrt{d(2R_c - d)}, \tag{2.9}$$

where λ is the wavelength of the light, d the distance between the two mirrors and R_c their radius of curvature [KOGELNIK1966]. In our case, the waist is about 44 µm.

The transmission of the cavity is monitored using a photodiode. The signal from this photodiode is fed into a lock-in amplifier which provides a feedback loop to maintain the cavity on resonance with the laser beam: the error signal is amplified to drive the piezo-mounted input mirror.

This lock is not very stable, partly because it is very sensitive to vibrations. It also drifts with temperature. Indeed when we fill the liquid-nitrogen trap of the diffusion pump in the morning, the temperature of the whole structure slowly lowers and the cavity contracts. This induces a large drift on the cavity stabilization, which must then be manually corrected. I also devised a semi-automatic re-locking feature that allows to re-lock the cavity by applying an additional, remotely-controlled voltage offset on the piezo-mounted mirror. During the day, the drift slows, stabilizes then reverses as the structure heats up again. Therefore, there are usually a few hours in the afternoon when the cavity is more stable. To corroborate the link between cavity length and temperature drifts, we placed thermistors on the metallic structure of the cavity. They indeed indicated temperature changes of more than 1 °C over one day.

The surtension coefficient S, defined as the ratio of the light intensity inside the cavity to the incident intensity, can be expressed theoretically as

$$S = \frac{T_1}{(1 - \sqrt{R_1 R_2})^2}, \tag{2.10}$$

where T_1 is the transmission coefficient of the input mirror and R_1 and R_2 are the reflection coefficients of the input and output mirrors.

Plugging into this equation the specified transmission and reflection coefficients of our mirrors, we obtain a theoretical surtension coefficient of about 40. However, the actual surtension coefficient is lower, because of the degradation of the mirrors

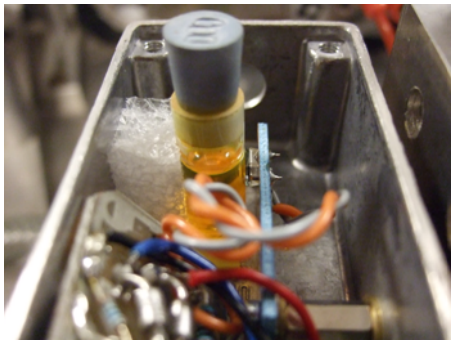

Figure 2.14: View of the fluorescein tube and photodiode placed at the output of the build-up cavity.

due to the UV light. In practice, it is quite hard to estimate accurately the actual intra-cavity power. Knowing this power is crucial for the light shift analysis.

In an attempt to improve the transmitted power measurement, we modified the photodiode, taking advantage of fluorescence properties of fluorescein. This red powder, diluted in water, emits green light when illuminated with UV. Placing a photodiode on the side of a small glass tube containing the fluorescein solution avoids the photodiode deterioration due to UV light that had been noted previously. Figure 2.14 shows a picture of the photodiode placed at the output of the build-up cavity. It allowed us to improve the magnitude of the signal used for locking, but day-to-day reproducibility is not so good and measuring the absolute transmitted power remains a difficult task.

We placed a silica plate at the output of the cavity to be able to measure directly the transmitted power with a power meter while maintaining the cavity at resonance. In principle, from this measurement, knowing the reflection coefficient of the plate and the transmission coefficient of the output mirror, we can derive the actual intra-cavity power. However, it is difficult to measure the exact transmission of the output mirror, because the UV light degrades the mirror coatings. In fact, when using a brand new mirror, the transmitted power decreases very rapidly over the first few days, then more slowly. And the impact point of the UV beam is clearly visible on “used” mirrors...

2.4.3 3S–2P fluorescence detection

The Balmer-α photons at 656 nm, resulting from the decay of the excited atoms to the 2P level, are collected by an imaging system as shown on Fig. 2.11, and detected by a photomultiplier (R943-02 model from Hamamatsu).

A first condenser guides the photons towards an interference filter at 656 nm. They are then focused by another condenser onto a slit, to reduce stray light. A third condenser images this slit, which is placed parallel to the atomic beam, on the photocathode of the photomultiplier. Furthermore, a spherical metallic mirror

situated below the cavity redirects photons emitted downwards, thus increasing the total opening angle of the detection system. Since the 656-nm interference filter has an acceptance angle of 11°, the detection region is a 12-mm-long segment of the atomic beam, at the center of the build-up cavity. A close-up view of the detection region will be given later (Fig. 3.5 in Chapter 3).

In order to count the number of fluorescence photons, the signal from the photomultiplier is filtered by a discriminator. This device compares the voltage of the photomultiplier signal to a threshold value, and emits a square voltage pulse of fixed height and duration if the signal is above the threshold. These pulses are recorded using a Racal-Dana 1992 universal counter.

2.5 Magnetic field production

In order to estimate the atomic velocity distribution and thus the second order Doppler shift, we apply a vertical magnetic field in the excitation region, following the method described in Chapter 1.

2.5.1 The Helmholtz coils

This magnetic field is produced by two coils, placed in Helmholtz configuration on either side of the detection region [Hagel2001]. The coils, of mean diameter 34.2 cm, are placed 11.6 cm apart. Each coil is formed of 23 turns of copper tube in which circulates a DC current on the order of a hundred amperes. To prevent overheating, closed-circuit cooling water flows inside the copper tubes.

In order to compensate the terrestrial magnetic field, smaller compensation coils are placed in the other two directions.

2.5.2 Calibration of the magnetic field

In order to calibrate the magnetic field created by the Helmholtz coil, we perform the spectroscopy of the $1S_{1/2}(F = 1, m_F = 0) \rightarrow 3S_{1/2}(F = 1, m_F = 0)$ transition. In fact, because the Zeeman shifting of these two sub-levels is different, this particular transition is much shifted by the magnetic field. Figure 2.15 shows the theoretical variation of the frequency of this transition as a function of the magnetic field applied to the atoms.

This displacement is on the order of 1 MHz/G, for a magnetic field of a few hundred gauss. To calibrate the magnetic field, we change the frequency of the Ti:Sa laser (by modifying f_{AOM}, see section 2.2.3) so as to aim at the expected position of the $1S_{1/2} \rightarrow 3S_{1/2}(F = 1, m_F = 0)$ transition, for several values of the electric current

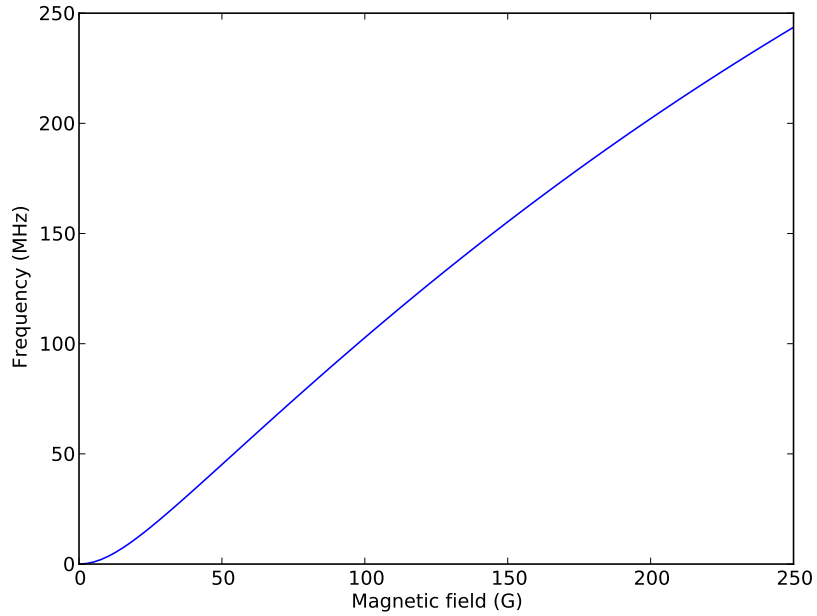

Figure 2.15: Theoretical frequency shift of the $1S_{1/2} \rightarrow 3S_{1/2}(F = 1, m_F = 0)$ transition as a function of magnetic field. This curve is used to convert the measured $m_F = 0$ frequency points into magnetic field values.

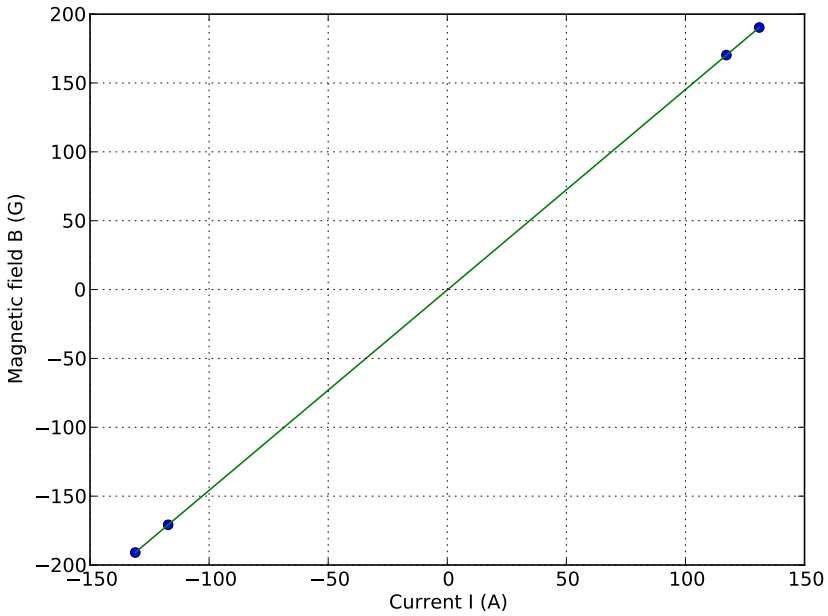

Figure 2.16: Magnetic field as a function of the electric current flowing in the Helmholtz coil. The experimental values (blue points), deduced from measurements of the $1S_{1/2} \rightarrow 3S_{1/2}(F = 1, m_F = 0)$ transition frequency using the curve of Fig. 2.15, are fitted by a linear model.

delivered by the power supply of the Helmholtz coils. Using the protocol described in detail in section 2.6, we measure the apparent frequency of this transition. From this observation, we can then deduce the value of the magnetic field using the curve of Fig. 2.15. As an example, for a current of 131 A, the position of the transition was shifted by 193.48 MHz, corresponding to a magnetic field of 190.3 G. The obtained data are shown in Fig. 2.16. A linear fit of this experimental data gives, with B in gauss and I in amperes,

$$B(I) = 1.455 \times I - 0.299. \tag{2.11}$$

The $m_F = 0$ frequency points we have measured have an uncertainty of about 10 kHz, yielding a measure of the magnetic field with a 10 mG uncertainty. However, the display of the power supply of the coils only has a 100 mA precision. Because of this, the actual magnetic field is only known in practice with a precision of about 100 mG.

2.6 Data acquisition and signals

2.6.1 Data acquisition

The data recording process is controlled by a computer program written in Python language. During a recording (colloquially called "run"), the frequency of the Ti:Sa laser is scanned using the acousto-optic modulator (f_{AOM}). A run is composed of 10 "scans", each of which contains N frequency points.

These frequency points, which are placed 40 kHz apart in units of the AOM frequency, follow a predefined back-and-forth sequence that has been optimized to avoid any unexpected drifts. We defined sequences for $N = 31$, 51 or 71 points, corresponding to a total scan width of 1.2, 2.0 or 2.8 MHz. This scan width is also in f_{AOM} units, and should be multiplied by 4 to get the atomic frequency scan width. Every other scan, the sequence is followed in reverse order so as to avoid slow drifts. The 31-point sequence is the following:
[1 ; 7 ; 13 ; 19 ; 25 ; 31 ; 26 ; 20 ; 14 ; 8 ; 2 ; 6 ; 12 ; 18 ; 24 ; 30 ; 27 ; 21 ; 15 ; 9 ; 3 ; 5 ; 11 ; 17 ; 23 ; 29 ; 28 ; 22 ; 16 ; 10 ; 4].

We recorded signals using the different scan widths. During her Ph.D., Sandrine Galtier always used a 1.2-MHz scan width. We initially defined the 2.8-MHz-wide sequence when the signal was unexpectedly broadened because of a bad stabilization of the 532-nm laser. When this problem was solved, we used the 2.0-MHz-wide sequence, which allows a better determination of the wings of the line profile. However, a run using this sequence lasts 10 minutes, as compared to 6 minutes using a 1.2-MHz scan width. It is thus rather time-consuming, so we decided to check whether the scan

width change had any effect on the determination of the central frequency. Having analyzed the 51-point signals, we removed the outer 20 points to simulate a 31-point sequence and re-analyzed the runs. The change in the average central frequency was less than 0.2 kHz. Therefore, we decided to use the 1.2-MHz-wide sequence for the remaining recording sessions.

For each frequency point, the computer records:

- the number of photons collected by the photomultiplier during one second;
- the frequency f_{AOM} of the signal applied to the AOM of the Ti:Sa laser;
- the frequencies of the various beat notes;
- the light power transmitted by the UV build-up cavity;
- the voltage delivered to the piezo-actuated input mirror of this cavity.

We also record manually other parameters, such as:

- the light power at the entrance of the cavity, between runs;
- the current applied to the Helmholtz coils, from which we can deduce the magnetic field using eq. (2.11);
- and the pressure inside the vacuum cavity.

2.6.2 Observed signals

Using the experimental protocol described above, we are able to observe the $1S-3S$ transition, both in hydrogen and in deuterium. However, only the hydrogen, $F=1$ transition was systematically studied during my Ph.D., varying the magnetic field applied to the atoms as well as the pressure in the cavity.

Hydrogen

Figure 2.17 shows the number of photons collected per second as a function of the frequency f_{AOM} of the AOM used to tune the Ti:Sa frequency. It is the mean of 47 runs recorded on the same day. The signal has been fitted here by a simple Lorentzian function,

$$f_{\mathrm{Lor}}(A,B,\Gamma,x_0;x) = A + \frac{B}{1+(\frac{x-x_0}{\Gamma/2})^2}. \tag{2.12}$$

The parameters are in the case of Fig. 2.17: $A=212$ counts/s, $B=272$ counts/s, $\Gamma=338$ kHz and $x_0=192.4$ MHz.

Note that the linewidth Γ, given above in units of the AOM frequency, corresponds to an atomic transition linewidth of about 1.35 MHz (as compared to the natural linewidth of 1.0 MHz). The different causes of broadening will be explored in Chapter 3.

We observe a large background of a few hundred to a thousand fluorescence counts per second. This background is strongly dependent on the 205-nm light power, and

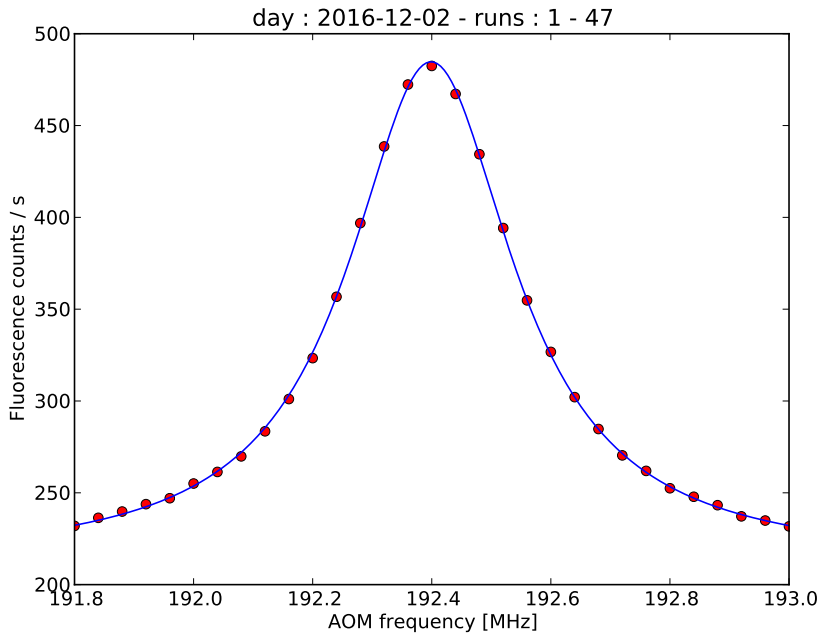

Figure 2.17: Hydrogen $1S - 3S$ signal. This is the mean over one day of recording using the 1.2-MHz (31 points) scan width, corresponding to an integration time of 4 hours. No magnetic field was applied to the atoms apart from the residual offset of -0.3 G, and the pressure was 2.7×10^{-5} mbar. Red points are experimental data, the blue line is a Lorenztian fit.

also on the power build-up cavity alignment. It is probably due to laser-induced fluorescence or photoelectric effects.

Deuterium

As explained in section 2.2.3, it is rather straightforward to modify the frequency of our laser source so as to reach the $1S - 3S$, $F = 1/2$ and $F = 3/2$ transitions of deuterium. I have been able to record signals of both transitions, as shown in Fig 2.18. At the time they were recorded, the frequency comb was under repair, so we were not able to measure the absolute frequency of these transitions.

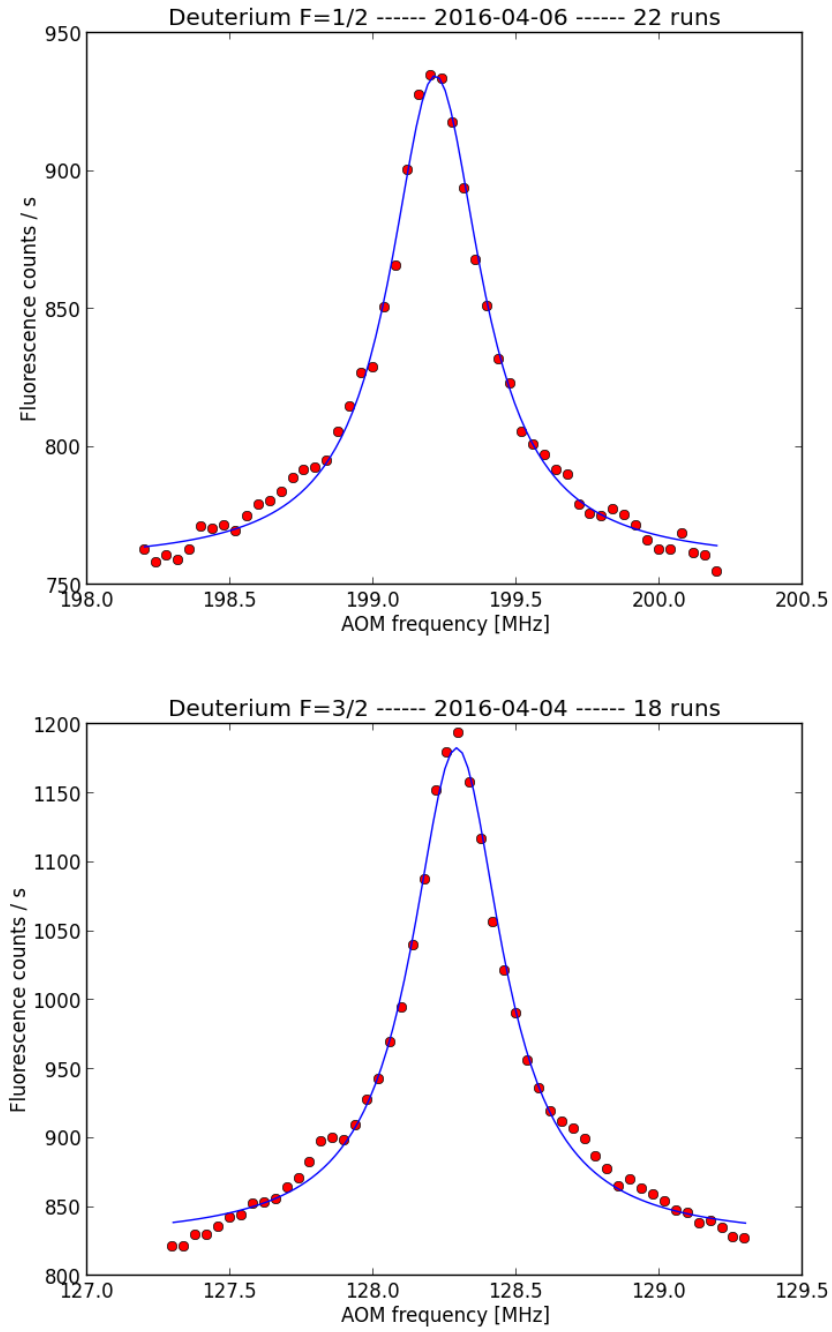

Figure 2.18: Deuterium $1S-3S$ signals. Each signal is the mean over one day of recording, corresponding to an integration time of around 3h for $F = 1/2$ (upper graph), and 2h15 for $F = 3/2$ (lower graph). They were recorded using the 51-point scan width (f_{AOM} scanned over 2 MHz). As in Fig. 2.17, the signals were fitted by Lorenztian functions (in blue).

Conclusion

In this chapter, I have presented the different parts of our experimental setup. The 205-nm excitation laser source built by S. Galtier is still very efficient, and the frequency measurement of our 532-nm laser has been improved. A point that remains difficult is the measurement of the excitation light intensity seen by the hydrogen atoms.

We have recently started building the cooling system that will enable us to perform the $1S-3S$ spectroscopy on a colder, and slower, atomic beam in the coming months. I was also able to record the first observation of the $1S-3S$ transition in deuterium since 1989 [Verkerk1989].

However, the present work is focused on an absolute frequency measurement of the $1S-3S(F=1)$ transition in hydrogen at room-temperature. I recorded many signals of this transition while varying parameters such as the pressure, the light intensity and the magnetic field, in order to characterize the various systematic effects that will be the subject of the next chapter.

Chapter 3

Systematic effects

The experimental signals presented in the last part of Chapter 2 are fitted using a theoretical line profile, which includes the second-order Doppler shift as well as the Zeeman and Stark shifts due to the magnetic field. Additional shifting effects should be evaluated and taken into account in the data analysis. In this chapter, I will present them theoretically, as well as broadening effects. The last part of the present chapter is devoted to the theoretical estimation of the cross-damping shifting effect, that is found to be small in our experiment.

3.1 The theoretical line profile

The theoretical fluorescence signal is calculated using a density matrix formalism, for given values of the magnetic field and atomic velocity. This calculation has been well described in [Hagel2001, Arnoult2010] and is presented in part 3.1.1.

The fluorescence, calculated for discrete values of the excitation frequency, is then integrated over the atomic velocity distribution. The models we have considered for this distribution will be detailed in part 3.1.2. Finally, I will explain how the full fitting function is created.

The entire line profile calculation is realized by a computer program written in the Python language.

3.1.1 Fluorescence calculation

In a first step, we calculate the $3S_{1/2}^{F=1} \rightarrow 2P_J$ fluorescence following the two-photon excitation, as a function of the frequency detuning, for fixed values of the atomic velocity and magnetic field. Because the Stark effect couples the $3S_{1/2}$ level to the $3P_J$ levels, the fluorescence from the $3P_J$ levels to the $2S_{1/2}$ also contributes to the observed signal. The magnetic field $\mathbf{B}$ is along the vertical z axis, which is chosen as the quantization axis. The polarization of the excitation laser is also along the z axis.

The evolution of the density matrix ρ follows the equation

$$\frac{\mathrm{d}\rho}{\mathrm{d}t} = \frac{1}{i\hbar}\left[(H + H_L + H_{Stark}), \rho\right] + \left\{\frac{\mathrm{d}\rho}{\mathrm{d}t}\right\}_{s.e.}. \tag{3.1}$$

The term $\left\{\frac{\mathrm{d}\rho}{\mathrm{d}t}\right\}_{s.e.}$ describes the relaxation due to spontaneous emission, and is of the form

$$\left\{\frac{\mathrm{d}\rho_{ij}}{\mathrm{d}t}\right\}_{s.e.} = -\frac{\Gamma_i + \Gamma_j}{2}\rho_{ij}, \tag{3.2}$$

where $\Gamma_i/2\pi$ is the natural width of level i. H_L describes the laser-atom interaction and H_{Stark} is the perturbation due to the motional electric field. H is the hamiltonian of a static hydrogen atom placed in a constant magnetic field and can be written as

$$H = H_0 + H_{hfs} + H_{Zeeman} + H_{diam}. \tag{3.3}$$

• H_0 is the unperturbed hamiltonian, which includes the fine structure. It has a diagonal form when written in the $|L, (S, I,)J, m_J, m_I\rangle$ basis, where its eigenvalues are the energy levels E_{nLJ} defined in Chapter 1.

• The hyperfine structure hamiltonian H_{hfs} describes the coupling between the angular momentum $\mathbf{J} = \mathbf{L} + \mathbf{S}$ and the proton spin $\mathbf{I}$. It is of the form [Bethe1957, Cohen-Tannoudji1973]

$$H_{hfs} = -\frac{\mu_0}{4\pi}\frac{\mu_B\mu_N g_N}{\hbar^2}\left[\frac{8\pi}{3}\delta^3(\mathbf{r})g_S\mathbf{S}\cdot\mathbf{I} + \frac{g_S}{r^3}\left(\frac{3}{r^2}(\mathbf{S}\cdot\mathbf{r})(\mathbf{I}\cdot\mathbf{r}) - \mathbf{S}\cdot\mathbf{I}\right) + \frac{2}{r^3}\mathbf{I}\cdot\mathbf{L}\right], \tag{3.4}$$

where μ_B is the Bohr magneton, μ_N the nuclear magneton, g_S and g_N the Landé factors of the electron and proton.

Making the approximation $g_S \simeq 2$, the matrix elements of this hamiltonian in the $|L, (S, I,)J, F, m_F\rangle$ basis can be written as [Julien1974]

$$\langle\Psi|H_{hfs}|\Psi'\rangle = \frac{3}{32}A\left[\frac{2}{J(J+1)(L+\frac{1}{2})}\langle\Psi|\mathbf{I}\cdot\mathbf{J}|\Psi'\rangle + \frac{1-\delta_{JJ'}}{L(L+1)(L+\frac{1}{2})}\langle\Psi|\mathbf{I}\cdot\mathbf{L}|\Psi'\rangle\right], \tag{3.5}$$

For the levels considered here, the constant A is equal to the $3S$ hyperfine splitting $\Delta E_{\mathrm{HFS}}(3S_{1/2})$, whose numerical value has been discussed in Chapter 1, part 1.1.3. For $L = 0$ levels, only the first term of eq. (3.5) is non-zero. For $L = 1$, a coupling term appears between terms of same m_J and different J.

• H_{Zeeman} corresponds to the Zeeman interaction of the magnetic moment of the atom with the vertical magnetic field $\mathbf{B}$. As this hamiltonian is diagonal in the $|L, (S, I,)m_S, m_L, m_I\rangle$ basis, it couples levels of same m_F but different F, and is

expressed as[1]

$$H_{Zeeman} = \mu_B B \left[g_S S_z + \left(1 - \frac{m_e}{m_p}\right) L_z - \frac{m_e}{m_p} g_N I_z \right]. \tag{3.6}$$

To this hamiltonian should be added the diamagnetic correction, due to the interaction between the magnetic moment induced by the magnetic field and the field itself. It can be written as

$$H_{diam} = \frac{q^2 B^2 r_\perp^2}{8 m_e}, \tag{3.7}$$

where $r_\perp$ is the projection of the position operator $\mathbf{r}$ on the plane perpendicular to the z quantization axis.

- H_{Stark} is the perturbation due to the motional Stark effect, defined as

$$H_{Stark} = q\mathbf{E} \cdot \mathbf{r}, \tag{3.8}$$

with $\mathbf{E} = \mathbf{v} \times \mathbf{B}$. This hamiltonian couples states of opposite parity ($\Delta L = \pm 1$). It has a simple form when written in the $|L, (S, I,)J, m_J, m_I\rangle$ basis, where it couples levels of same m_I with $\Delta m_J = \pm 1$. This last condition is due to the fact that the electric field is perpendicular to the quantization axis.

In the Python program that performs the calculation, we define each hamiltonian in the most convenient basis, then diagonalize the static hamiltonian H, yielding a specific, "coupled" basis for each value of the magnetic field. Finally, we convert the Stark perturbation to this new basis, in which the rest of the calculation is done.

- H_L is the hamiltonian of laser-atom interaction. Making the usual rotating wave approximation, we can define its matrix element as

$$\langle e|H_L|g\rangle = \frac{\hbar \Omega_e}{2} \exp(-2i\omega t), \tag{3.9}$$

where g and e denote the ground ($1S$) and excited ($3S$) states, $\omega/2\pi$ is the laser frequency and Ω_e the two-photon Rabi pulsation

$$\Omega_e = \frac{8\pi a_0^2 \, Q_{eg} \, I}{mc^2 \alpha}. \tag{3.10}$$

Here Q_{eg} is the matrix element of the two-photon excitation operator. For a laser

[1] As noted in Chapter 1 (eq. (1.31)), the Landé factor of the electron g_S depends on the considered level.

polarization along the z axis, it is defined as

$$Q_{eg} = \left| \sum_r \frac{\langle e|z|r\rangle\langle r|z|g\rangle}{\omega - \omega_{rg}} \right|^2 . \tag{3.11}$$

As explained in [ARNOULT2010], the rest of the calculation is done in the rotating frame, replacing the density matrix by the operator σ defined as $\sigma_{gg} = \rho_{gg}$, $\sigma_{eg} = \rho_{eg}\exp(2i\omega t)$ and $\sigma_{ge} = \rho_{ge}\exp(-2i\omega t)$. We assume that the transition is not saturated, in other words the atoms decay much more rapidly than they are excited ($\Omega_e \ll \Gamma_e$). In practice, this condition is indeed fulfilled, as will be explained in part 3.3.1. The populations of the excited states are thus much lower than that of the ground state, and we can neglect them in a first step for the purpose of deriving the following equations, where the indices g, e and f correspond respectively to the $1S_{1/2}$, $3S_{1/2}$ and $3P_J$ states,

$$\frac{\mathrm{d}\sigma_{gg}}{\mathrm{d}t} = -\frac{i}{2}\Omega_e(\sigma_{eg} - \sigma_{ge}), \tag{3.12}$$

$$\frac{\mathrm{d}\sigma_{eg}}{\mathrm{d}t} = \left(i\Delta_e - \frac{\Gamma_e}{2}\right)\sigma_{eg} - i\frac{\Omega_e}{2}\sigma_{gg} - \frac{i}{\hbar}\sum_f V_{ef}\sigma_{fg}, \tag{3.13}$$

$$\frac{\mathrm{d}\sigma_{fg}}{\mathrm{d}t} = \left(i\Delta_f - \frac{\Gamma_f}{2}\right)\sigma_{fg} - \frac{i}{\hbar}\sum_f V_{fe}\sigma_{eg}, \tag{3.14}$$

with $V_{ef} = \langle e|H_{Stark}|f\rangle$ and $\Delta_{e,f} = 2\omega - (\omega_{e,f} - \omega_g)$. We assume that σ_{eg} and σ_{fg} follow adiabatically the population of the ground state, that is, $\mathrm{d}\sigma_{ig}/\mathrm{d}t = 0$ for $i = e, f$. From the above set of equations, we can obtain the evolution of the population of the ground state and the transition probability, as well as an expression of σ_{eg} as a function of σ_{gg}.

From eq. (3.1) one can also derive the following set of equations

$$\frac{\mathrm{d}\sigma_{ee}}{\mathrm{d}t} = -\Gamma_e\sigma_{ee} + \frac{i}{2}\Omega_e(\sigma_{eg} - \sigma_{ge}) - \frac{i}{\hbar}\sum_f(V_{ef}\sigma_{fe} - \sigma_{ef}V_{fe}), \tag{3.15}$$

$$\frac{\mathrm{d}\sigma_{fe}}{\mathrm{d}t} = -\frac{\Gamma_e + \Gamma_f}{2}\sigma_{fe} - i(\omega_f - \omega_e)\sigma_{fe} + \frac{i}{2}\Omega_e\sigma_{fg} - \frac{i}{\hbar}V_{fe}(\sigma_{ee} - \sigma_{ff}), \tag{3.16}$$

$$\frac{\mathrm{d}\sigma_{ff}}{\mathrm{d}t} = -\Gamma_f\sigma_{ff} - \frac{i}{\hbar}(V_{fe}\sigma_{ef} - \sigma_{fe}V_{ef}). \tag{3.17}$$

Given the fact that the transition probability is very small compared to the natural width of the $3S$ level, we can assume a stationary regime, that is, $\mathrm{d}\sigma_{ii'}/\mathrm{d}t = 0$ for $i, i' = e$ or f. This allows to solve eqs. (3.14–16) in order to calculate the populations σ_{ee} and σ_{ff} of all excited states, as detailed in [ARNOULT2010].

The second-order Doppler shift is included at this point by multiplying the laser frequency by $(1 + v^2/2c^2)$.

The fluorescence due to the excitation of a particular $3S_{1/2}(F = 1, m_F)$ sublevel is

$$F(m_F; \omega, B, v) = \Gamma_e \sigma_{ee} + \sum_f \gamma_f \Gamma_f \sigma_{ff}, \tag{3.18}$$

where σ_{ee} is the population of this m_F sublevel, f denotes all $3P_J$ levels that are mixed with the $3S_{1/2}$ level by the Stark effect, and $\gamma_f = 0.11834$ is the branching ratio of the $3P - 2S$ decay.

Finally, we sum over $m_F = 0, \pm 1$ to calculate the total fluorescence

$$F_{tot}(\omega, B, v) = \sum_{m_F} F(m_F; \omega, B, v). \tag{3.19}$$

Note that the $m_F = 0$ sublevel only contributes to the signal for $B \sim 0$, as explained in Chapter 1.

3.1.2 The velocity distribution

The velocity distribution of atoms in a volume of gas follows a Maxwellian distribution

$$f_M(v) \propto v^2 \exp\left(-\frac{v^2}{2\sigma^2}\right), \tag{3.20}$$

with $\sigma = \sqrt{k_B T/m}$, where k_B is the Boltzmann constant, T the temperature and m the atomic mass. In the case of an effusive atomic beam, the above distribution should be multiplied by a factor of v, since the probability of an atom emerging from the source is proportional to its velocity [Ramsey1956].

In order to determine the experimental value of σ, we can analyze the data using line profiles that are integrated over given velocity distributions. The value of σ which allows to fit the data with the smallest uncertainty would then be retained as the optimal value.

However, the actual velocity distribution of our hydrogen atoms is more complicated. During the Ph.D. of Sandrine Galtier, several velocity distributions were tested. As a first step, the group explored the possibility of varying the exponent N of the following Maxwellian-type distribution,

$$f_N(v) \propto v^N \exp\left(-\frac{v^2}{2\sigma^2}\right), \tag{3.21}$$

with $N = 3$ for an effusive beam. The line profile integrated over this distribution fitted the experimental data better with N greater than 3.

Such a distribution, with an exponent $N > 3$, presents a depletion of slow atoms as compared to an effusive beam. This depletion could in part be explained by collisions

occurring within the nozzle. Such collisions would induce a velocity dependence of the mean free path of the atoms, reducing the number of slow atoms in the beam resulting from the nozzle or channel. Following an argument developed in [Olander1970], we can calculate the Knudsen number $\mathrm{Kn} = \lambda_c/L$, where λ_c is the mean free path in the reservoir and L is the channel length. If this number is small, the mean free path inside the channel has a large velocity dependence which can give rise to depletion effects. In our case, with a pressure of 0.3 Torr inside the discharge tube and a channel length of 3 cm, the Knudsen number is estimated at about 0.01.

According to [Olander1970], the velocity distribution of the effusive beam should then be multiplied by a perturbation function

$$P[\Psi(z), \mathrm{Kn}] = \frac{\sqrt{\pi}}{2}\sqrt{\frac{\mathrm{erf}[\Psi(z)/2\,\mathrm{Kn}]}{\Psi(z)/2\,\mathrm{Kn}}}, \tag{3.22}$$

where $\Psi(z)$ is defined as

$$\Psi(z) = \frac{z\exp(-z^2) + (\sqrt{\pi}/2)(1+2z^2)\mathrm{erf}(z)}{\sqrt{2\pi}z^2}, \tag{3.23}$$

with $z = v/\sqrt{2}\sigma$.

Furthermore, to describe an additional depletion due to collisions along the atomic beam, between the nozzle and the laser excitation, with the residual background gas, we multiply the distribution by another factor $\exp(-v_0/v)$ [Galtier2014a, Vigué2014]. During the Ph.D. of Sandrine Galtier, there was a serious doubt about a possible pressure dependence of the v_0 coefficient, which had a great incidence on the transition frequency. This dependence is directly investigated in this work (see Chapter 4). In fact, the velocity distribution does not seem to depend significantly on the pressure.

Finally, the velocity distribution model used in the line profile calculation is

$$f(v, \sigma, v_0) \propto v\ f_M(v, \sigma)\ P[\Psi(z), \mathrm{Kn}]\ \exp(-v_0/v). \tag{3.24}$$

This distribution depends on two parameters, σ and v_0. As explained in Sandrine Galtier's manuscript, it is somehow equivalent to use the above distribution or the one with a varying N exponent. Two adjustable parameters (σ and either N or v_0) are needed to correctly describe the velocity distribution.

When integrating the fluorescence over this distribution, two other coefficients have to be included. First, one should multiply the distribution by $1/v$ because slow atoms have a higher transition probability due to a greater interaction time with the laser.

Additionally, the model is multiplied by another coefficient $g(v)$ which describes a geometric effect due to the inhomogeneous light intensity seen by the atoms [Arnoult2006]. This correction is based on the fact that the light intensity the atoms experience when the excitation takes place is linked to the atomic velocity. Indeed, atoms are detected at the waist of the Gaussian beam, but the point at which they have been excited depends on their velocity. However, this does not have any significant effect on the line profile, as it modifies the center frequency of only a few Hz. It is nevertheless included in the calculation.

We can now integrate the fluorescence over the velocity distribution to obtain the line profile

$$R(\omega, B, \sigma, v_0) = \int_0^{+\infty} \frac{1}{v}\, g(v)\; f(v, \sigma, v_0)\; F_{tot}(\omega, B, v)\; \mathrm{d}v. \tag{3.25}$$

3.1.3 The complete fitting function

We calculate in this manner several profiles $R(\omega, B, \sigma, v_0)$ corresponding to different values of the magnetic field B and/or different velocity distribution parameters σ and v_0. Each profile, calculated for discrete frequency values, is converted into a continuous function $S_{B,\sigma,v_0}(\nu)$ of the atomic frequency detuning ν by means of a spline interpolation.

Moreover, the profile is convoluted with a Lorentzian function of width Γ to simulate broadening effects (see part 3.3), and amplitude and offset parameters are added to create the final fitting function,

$$F_{B,\sigma,v_0}(\nu_c, \Gamma, A, C; \nu) = A \times (S_{B,\sigma,v_0} * f_{\mathrm{Lor}})(\nu - \nu_c, \Gamma) + C, \tag{3.26}$$

where the convolution is defined as

$$(S_{B,\sigma,v_0} * f_{\mathrm{Lor}})(\nu, \Gamma) = \int S_{B,\sigma,v_0}(x)\, f_{\mathrm{Lor}}(\nu - x, \Gamma)\, \mathrm{d}x. \tag{3.27}$$

This function will be used in the next chapter to analyze the experimental data. For each signal, we perform a fit with four parameters (ν_c, Γ, A, C).

Here, the parameter ν_c is not the apparent transition frequency, but is automatically corrected from the Doppler, Zeeman and Stark effects which are already taken into account in the line profile. In the absence of any other systematic effect, it would correspond to the frequency of the unperturbed transition.

However, let us now take a look at the different systematic effects that are not included in this theoretical profile and could shift or broaden the observed line shape.

3.2 Shifting effects

Apart from the second-order Doppler shift, there are two main shifting effects in our experiment, the light shift and the pressure shift, which both induce shifts in the kHz range. The cross-damping effect, which is also a shifting effect but rather small in our case, has been studied theoretically in greater detail and will be described in part 3.4.

3.2.1 Light shift

The light shift, also called ac Stark shift, is due to a coupling of the atomic states with the excitation photons [Cohen-Tannoudji1962]. An electromagnetic field has two effects on the energy levels: on resonance it induces transitions, off resonance (or in the case of a two-photon transition, where each photon taken separately is far off resonance) it creates shifts. The frequency shift of a given energy level nL is of the form

$$\Delta\nu_{ac}(nL) = \beta_{ac}(nL) \times I, \tag{3.28}$$

where I is the light intensity seen by the atoms and β_{ac} is a coefficient tabulated for hydrogen two-photon transitions in [Haas2006].

The excitation takes place at the center of the cavity, where the waist of the laser beam is $w_0 = 44$ µm. Based on a surtension coefficient of 30, we can derive an estimate of the light intensity inside the build-up cavity. For an incident power of 10 mW, assuming that only about 70% of the incident light is successfully coupled in the cavity, the intra-cavity power P would be about 210 mW in each direction of propagation.

The intensity on the axis of a Gaussian laser beam of power P and waist w_0 is

$$I = \frac{2P}{\pi w_0^2} \simeq 69 \text{ MW/m}^2. \tag{3.29}$$

The values of the coefficient β_{ac} are given below,

Level	β_{ac} [Hz(W/m^2)$^{-1}$]
$1S$	-3.02104×10^{-5}
$3S$	9.80847×10^{-5}

The total shift of the $1S - 3S$ transition frequency would then be

$$\Delta\nu = [\beta_{ac}(3S) - \beta_{ac}(1S)] \times 2I \simeq 17.7 \text{ kHz}, \tag{3.30}$$

where we have multiplied the intensity by two to take into account the two counter-propagating beams.

This was calculated for the maximal intensity at the center of a Gaussian light beam. To take into account the light intensity distribution, we follow an argument developed in [Girard1983] for atoms at rest in a Gaussian beam. The atoms situated at the center of the beam experience a larger light shift and contribute more to the signal. Assuming an infinitesimal linewidth, the line profile can be approximated by a right triangle, with the highest point corresponding to the most shifted frequency. An average value of the light shift can obtained from the barycenter of this triangle, multiplying the result of eq. (3.30) by a factor of 2/3. This would give a light shift of about 11.8 kHz.

It is thus important to quantify the light shift experimentally in order to correctly take it into account in the data analysis. This will be done in Chapter 4.

3.2.2 Pressure shift

When an atom undergoes a collision with a perturbator (another atom, or a molecule of the residual background gas), its internal state is perturbed. The induced dephasing creates a pressure-dependent shift and broadening of the observed transition.

The sign of the pressure shift depends on the nature of the interaction potential: if the interaction is attractive, the frequency shift will be negative [Biraben1974]. In our experiment, it is crucial to determine the magnitude and sign of this shift, all the more so because of the questions that remained unresolved at the end of Sandrine Galtier's Ph.D.

At the time, the pressure dependence of the velocity distribution parameter v_0 had not yet been experimentally investigated.

Hence, the group first analyzed the data assuming that the velocity distribution did not depend on pressure, obtaining a negative pressure shift. Then it was assumed that v_0 depended linearly on the pressure. Surprisingly, using a pressure-dependent velocity distribution changed the sign of the pressure shift!

In the present work, we have estimated the velocity distribution for each pressure point. This has allowed us to determine the pressure shift with better confidence. The results will be presented in the next chapter, here I simply wish to point out that the pressure shift we observe is negative.

This sign is in agreement with a modelization performed by Arthur Matveev [Matveev2017, Yost2016], in which collisions between the $3S$ hydrogen atoms and either $1S$ atoms or H_2 molecules were simulated using an attractive Van-der-Waals potential. The pressure shift coefficient obtained from his model is on the order of -130 kHz/Pa, or -13 MHz/mbar, the pressure being calculated from the atomic concentration in the beam.

In our setup we can only measure the pressure in a relative way, so that the actual

pressure inside the atomic beam is unknown. Therefore, we determine the pressure shift experimentally by measuring the $1S-3S$ frequency for several pressure values. As will be seen in Chapter 4, the maximal pressure shift we have observed is about -16 kHz. It indeed needs to be carefully studied.

3.3 Broadening effects

I will now turn to the different broadening effects that can play a role in our experiment. As we have seen in Chapter 2, the width of the observed line shape is larger than the natural linewidth of the $3S$ level. The aim of this section is to find an explanation to this observed Lorentzian broadening.

3.3.1 Saturation broadening

If the excitation intensity is very high, the transition probability can become comparable to the natural linewidth; in this case, the transition is said to be broadened by saturation. In order to estimate this broadening, we can compare the two-photon Rabi pulsation to the natural linewidth of our transition.

The two-photon Rabi pulsation Ω is given in rad/s by

$$\Omega = 2(2\pi\beta_{ge})I, \tag{3.31}$$

where I is the laser intensity and β_{ge} is another coefficient tabulated in [Haas2006]. For the $1S-3S$ transition, the value of this coefficient is $\beta_{ge} = 1.00333 \times 10^{-5}$ Hz$(\mathrm{W/m^2})^{-1}$. There is an additional factor of 2 in the definition of Ω to take into account the two counter-propagating laser beams.

With a light intensity of $I = 69$ MW/m^2 as estimated in part 3.2.1, we find $\Omega/2\pi \simeq 1.4$ kHz; this value is very small compared to the 1-MHz natural linewidth of the $3S$ level.

The saturation broadening is thus small in our experiment.

3.3.2 Transit-time broadening

Another cause of broadening is due to the finite transit time of the atoms through the laser beam. This effect has been studied in detail by F. Biraben *et al.* [Biraben1979].

For a single atom of transverse velocity v_t with respect to the laser beam axis, the line profile becomes convoluted by a Gaussian function, giving rise to the broadening

$$\delta_{tt} = \frac{2\sqrt{\ln 2}v_t}{\pi w_0}, \tag{3.32}$$

where $w_0 = 44$ µm is the waist of the laser beam.

In practice, the atomic trajectories are constrained by diaphragms situated between the nozzle and the detection region. The maximal angle allowed by these diaphragms is $\theta \sim 0.6°$. The transverse velocity of an atom along such a tilted trajectory can be approximated by $v \sin\theta$, where v is the longitudinal velocity. Assuming a typical velocity of 3 km/s for this order of magnitude calculation, we obtain a broadening $\delta_{tt} \sim 380$ kHz.

This transit-time effect could thus partly explain the observed broadening. A more complete calculation of this effect would involve integrating over all possible atomic trajectories as well as over the velocity distribution. This has not been done yet because it is not necessary for our measurement, since there is no frequency shift associated to this effect.

3.3.3 Collisional broadening

As mentioned earlier when discussing the pressure shift, collisions between atoms also induce a broadening of the $1S-3S$ transition.

Indeed, we have experimentally observed a broadening of the line at higher pressure. Assuming a linear dependence of the broadening on the pressure, we estimate a broadening coefficient of about 1 GHz/mbar. This would correspond to a broadening of 30 kHz for a measured pressure of 3×10^{-5} mbar.

3.3.4 Observed broadening

Going back to Fig. 2.17 in Chapter 2, the observed linewidth of the $1S-3S$ transition, at a pressure of 2.7×10^{-5} mbar, was about 1.35 MHz, as compared to the natural linewidth of 1 MHz. This broadening can be explained in part by transit time broadening. Pressure broadening could also play a role.

Moreover, another source of broadening is the spectral width of the Verdi laser. Indeed, when the frequency of this laser was not well stabilized, the observed linewidth of the transition increased to more than 2 MHz.

3.4 Cross-damping effect

A version of this section has been published in Phys. Rev. A under the title *Cross-damping effects in* $1S-3S$ *spectroscopy of hydrogen and deuterium* [Fleurbaey2017].

Another effect which has to be estimated in our experiment is the so-called cross-damping effect, or quantum interference, which can occur when an optically induced atomic transition is detected via the ensuing fluorescence [Horbatsch2010]. It stems

from the presence of neighboring, off-resonant states than can be coherently excited along with the resonant transition, and whose decay is detected in a non-selective manner.

Interference then takes place between different radiative paths sharing the same initial and final states. The signal becomes the square modulus of a sum of amplitudes, instead of being simply a sum of intensities, or, to write it in a mathematical form,

$$\text{Signal} = \left| \sum_{\mathrm{i}} \mathrm{A_i} \right|^2 = \sum_{\mathrm{i}} |\mathrm{A_i}|^2 + \sum_{\substack{i,j \\ i \neq j}} \mathrm{A_i A_j^*}. \tag{3.33}$$

Hence, the observed line shape is not an incoherent sum of Lorentzian profiles but rather a coherent sum, in which cross terms appear. These cross terms, having a dispersion shape, induce an asymmetry of the line profile and a shift of the apparent center frequency of the transitions, that are not taken into account in our current line shape model. The shift of the transition frequency can be important if the off-resonant transitions are close enough [Brown2013].

Frequency shifts due to quantum interference have been estimated precisely for several transitions in muonic hydrogen, deuterium and helium by P. Amaro *et al.* [Amaro2015], and they have been found to be negligible. However, it is also necessary to evaluate these shifts in the case of electronic hydrogen, especially for the $2S - 4P$ [Beyer2017] and $1S - 3S$ transitions.

Besides our own experiment, the $1S - 3S$ transition of electronic hydrogen is also studied by the group of T. W. Hänsch in Garching [Yost2016]. In both experiments, the transition is detected through the Balmer-α fluorescence at 656 nm ($3S - 2P$). The cross-damping effect is caused by the presence of the $3D$ levels, a few GHz away from the $3S$ level, that can be off-resonantly excited and will also decay to the $2P$ levels while emitting photons at 656 nm. In Garching, the hydrogen atoms are excited by a picosecond pulsed laser. Evaluating the quantum interference shift for their measurements [Yost2014] required the use of a density matrix formalism, leading to complex calculations with many coupled equations. In our experiment, on the contrary, the excitation laser at 205 nm is a continuous-wave laser. This allows us to use a simpler method, similar to the one developed by P. Amaro *et al.*, to estimate the magnitude of the cross-damping effect.

Since it is possible, with our experimental setup, to observe the $1S - 3S$ transition in hydrogen and deuterium, both isotopes will be studied in this section.

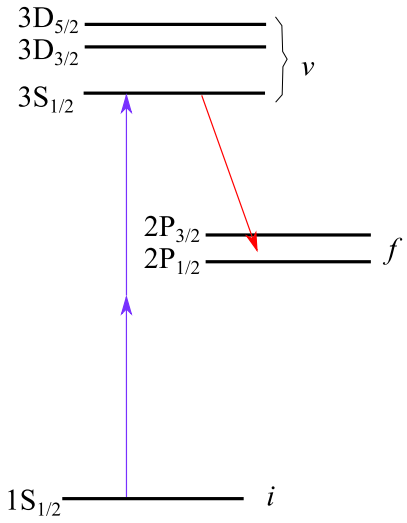

Figure 3.1: The relevant fine-structure energy levels of hydrogen ($I = 1/2$) or deuterium ($I = 1$).

	Hydrogen		Deuterium	
Level	F	Freq.(MHz)	F	Freq.(MHz)
$3S_{1/2}$	0	−39.457	1/2	−8.084
	1	13.152	3/2	4.042
$3D_{3/2}$	1	2927.249	1/2	2929.542
	2	2931.458	3/2	2930.027
			5/2	2930.835
$3D_{5/2}$	2	4011.639	3/2	4013.498
	3	4014.344	5/2	4013.844
			7/2	4014.329

Table 3.1: Energies of the $n = 3$ hyperfine sublevels relative to the fine structure $3S_{1/2}$ level, for hydrogen and deuterium. The linewidth $\Gamma_\nu/2\pi$ is 1.0 MHz for the $3S$ level and 10.3 MHz for the $3D$ levels.

3.4.1 Method

In order to evaluate the shift due to this quantum interference effect, we follow the method described in [Amaro2015], adapting it for a two-photon transition and our experimental geometry. In the same manner, we can consider the spectroscopy as a two-step process equivalent to Raman Stokes scattering, albeit with a two-photon excitation.

As detailed in Fig. 3.1, we will denote i the initial energy level ($1S$), ν the intermediate level ($3S$ or $3D$) of natural linewidth Γ_ν, and f the final level ($2P$). Table 3.1 gives the relative energies of the relevant hyperfine sublevels. To calculate these energy levels, I used fine structure data from the NIST database [Jentschura2005]. The hyperfine splitting was calculated in Chapter 1 for hydrogen (see also eq. (3.5)), and has been obtained in a similar manner for deuterium [Karshenboim2002].

Assuming a near-resonant excitation, this scattering process can be described by an equation of the Kramers-Heisenberg type, similar to eq. (2) of [Amaro2015], in which the excitation operator has been replaced by a two-photon operator:

$$\frac{d\sigma}{d\Omega} \propto \sum_f \left| \sum_\nu \frac{Q_{\nu i}(D_{f\nu})^*}{\omega_{\nu i} - 2\omega - i\Gamma_\nu/2} \right|^2 . \tag{3.34}$$

In this equation, $d\sigma/d\Omega$ is the differential cross section of the scattering amplitude, $\omega_{\nu i}$ the transition angular frequency, ω the laser angular frequency, $Q_{\nu i}$ the matrix element of the two-photon excitation operator, and $D_{f\nu}$ the dipole matrix element corresponding to the one-photon decay.

The cross-damping effect involves transitions from the same initial state ($J_i = 1/2$, F_i). For a given F_i, the sum over ν can be restricted to the $3S$ and $3D$ sublevels allowed by the selection rules [Grynberg1976],

- for the $3S_{1/2}$ level: $F_\nu = F_i$, due to the selection rule $\Delta F = 0$ for two-photon transitions between $J = 1/2$ states;
- for the 3D levels: $\Delta F \leq 2$, with $F_i = 0 \to F_\nu = 1$ and $F_i = 1/2 \to F_\nu = 1/2$ forbidden.

In this chapter, we estimate the cross-damping shift for all possible $1S - 3S$ hyperfine transitions ($F_i = 0$ and 1 for hydrogen, $F_i = 1/2$ and 3/2 for deuterium).

Our experimental situation

We define here the geometry of the scattering process in accordance with our experimental situation. The excitation cw laser at 205 nm is resonant in a Fabry-Perot cavity whose axis is horizontal and collinear with the atomic beam. The laser polarization is vertical. The $3S - 2P$ fluorescence at 656 nm is collected by an imaging system situated directly above the excitation region, and detected by a photo-multiplier. We do not detect the polarization of this fluorescence.

Figure 3.2 shows the relevant vectors and angles. The two incident photons have the same polarization $\boldsymbol{\varepsilon}_1$ (parallel to the z axis), and opposite wave-vectors $\mathbf{k}_1 = -\mathbf{k}'_1$ along the x axis. The wave-vector $\mathbf{k}_2$ of the scattered photon makes an angle θ with the vertical z axis, which is chosen as the quantization axis. As mentioned in [Brown2013] and [Amaro2015], the quantum interference effect depends only on this angle θ between the incident polarization and the scattering direction. Without any loss of generality, we will assume that this wave-vector $\mathbf{k}_2$ is in the plane xOz. We also define χ_2 as the angle between the scattered photon's polarization $\boldsymbol{\varepsilon}_2$ and the plane xOz.

The following calculation is done first in the case of a point-like detector situated at an angle θ from the z axis. In order to simulate more closely our experimental

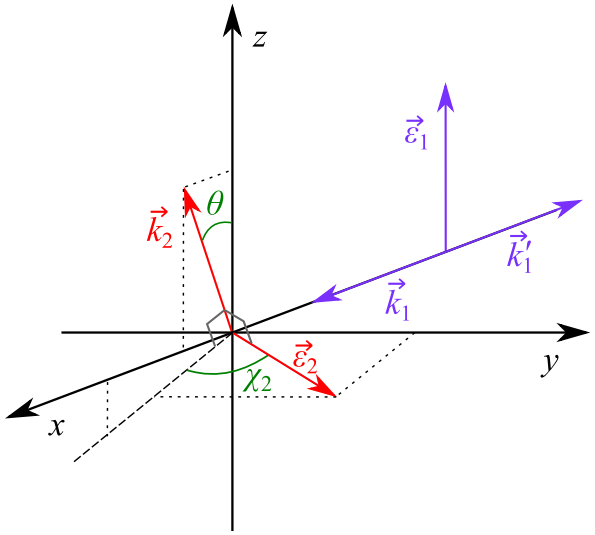

Figure 3.2: The incident photons have opposite wave-vectors $\mathbf{k}_1 = -\mathbf{k}'_1$ and the same polarization $\boldsymbol{\varepsilon}_1$. The direction of the wave-vector $\mathbf{k}_2$ of the scattered photon defines the angle θ. This photon's polarization $\boldsymbol{\varepsilon}_2$, which lies in a plane perpendicular to $\mathbf{k}_2$, makes an angle χ_2 with the scattering plane xOz.

situation, we will then evaluate the effect for a finite angular aperture of the detection system.

3.4.2 Details of the calculation

The polarization vectors of the incident ($\boldsymbol{\varepsilon}_1$) and scattered ($\boldsymbol{\varepsilon}_2$) photons, as defined above, can be written in a standard basis [CAGNAC2002].

The unit vectors $\mathbf{e}_\lambda$ of this basis are defined as a function of the cartesian unit vectors $(\mathbf{u}_x, \mathbf{u}_y, \mathbf{u}_z)$ as

$$\mathbf{e}_0 = \mathbf{u}_z, \quad \mathbf{e}_{\pm 1} = \mp \frac{\mathbf{u}_x \pm i\mathbf{u}_y}{\sqrt{2}}, \tag{3.35}$$

and the coordinates a_λ of a vector $\mathbf{a}$ in this basis verify

$$\mathbf{a} = \sum_\lambda (-1)^\lambda a_{-\lambda} \mathbf{e}_\lambda. \tag{3.36}$$

Furthermore, the inner product in this basis (equivalent to the scalar product in the cartesian basis) is

$$\mathbf{a} \cdot \mathbf{b} = \sum_\lambda (-1)^\lambda a_{-\lambda} b_\lambda = \sum_\lambda a^*_\lambda b_\lambda. \tag{3.37}$$

The coordinates of the polarization vectors in this basis are then

$$\begin{aligned} &\varepsilon_1^{(\pm 1)} = 0, \quad \varepsilon_1^{(0)} = 1, \\ &\varepsilon_2^{(\pm 1)} = \mp \frac{(\cos\chi_2 \cos\theta \pm i \sin\chi_2)}{\sqrt{2}}, \quad \varepsilon_2^{(0)} = -\cos\chi_2 \sin\theta. \end{aligned} \tag{3.38}$$

The dipole matrix element is defined as $D_{f\nu} = \boldsymbol{\varepsilon}_2 \cdot \mathbf{D}_{f\nu} = \langle f|\boldsymbol{\varepsilon}_2 \cdot \mathbf{r}|\nu\rangle$. We can expand the scalar product in the spherical basis, while taking into account the hyperfine structure:

$$D^{F_\nu m_\nu J_\nu}_{F_f m_f J_f} = \sum_{\lambda=-1}^{1} (-1)^\lambda \varepsilon_2^{(-\lambda)} \langle n_f L_f F_f m_f J_f | r_\lambda | n_\nu L_\nu F_\nu m_\nu J_\nu \rangle. \tag{3.39}$$

The two-photon matrix element is expressed as

$$Q_{\nu i} = \left| \sum_r \frac{(\boldsymbol{\varepsilon}_1 \cdot \mathbf{D}_{\nu r})(\boldsymbol{\varepsilon}_1 \cdot \mathbf{D}_{ri})}{\omega - \omega_{ri}} \right|^2 = \left| \sum_r \frac{\langle \nu|\boldsymbol{\varepsilon}_1 \cdot \mathbf{r}|r\rangle\langle r|\boldsymbol{\varepsilon}_1 \cdot \mathbf{r}|i\rangle}{\omega - \omega_{ri}} \right|^2. \tag{3.40}$$

It can also be written as the matrix element of a k^{th}-order tensor operator $\mathbf{T}^{(k)}$, with $k = 0$ for $1S-3S$, $k = 2$ for $1S-3D$ [Grynberg1976]. Since the incident polarization $\boldsymbol{\varepsilon}_1$ is along the quantization axis (this implies $m_\nu = m_i$), we simply have

$$Q^{F_i m_i J_i}_{F_\nu m_\nu J_\nu} = \langle n_\nu L_\nu F_\nu m_\nu J_\nu | T^{(k)}_0 | n_i L_i F_i m_i J_i \rangle. \tag{3.41}$$

Defining $\mathbf{T}^{(1)} = \mathbf{r}$, the matrix elements on the right-hand side of eqs. (3.39) and (3.41) can be simplified by introducing the reduced matrix element, then successively decoupling the angular momenta to separate radial and angular parts, using the following usual relations [Edmonds1957]:

$$\begin{aligned}
\langle n'L'F'm'J'|T^{(k)}_\lambda|nLFmJ\rangle &= (-1)^{F'-m'} \begin{pmatrix} F' & k & F \\ -m' & \lambda & m \end{pmatrix} \langle n'L'F'J'||\mathbf{T}^{(k)}||nLFJ\rangle, \\
\langle n'L'F'J'||\mathbf{T}^{(k)}||nLFJ\rangle &= (-1)^{J'+I+F+k} \sqrt{[F,F']} \begin{Bmatrix} J' & F' & I \\ F & J & k \end{Bmatrix} \langle n'L'J'||\mathbf{T}^{(k)}||nLJ\rangle, \\
\langle n'L'J'||\mathbf{T}^{(k)}||nLJ\rangle &= (-1)^{L'+S+J+k} \sqrt{[J,J']} \begin{Bmatrix} L' & J' & S \\ J & L & k \end{Bmatrix} \langle n'L'||\mathbf{T}^{(k)}||nL\rangle,
\end{aligned} \tag{3.42}$$

with the notation $[J, J'] = (2J+1)(2J'+1)$. One obtains

$$\begin{aligned}
D^{F_\nu m_\nu J_\nu}_{F_f m_f J_f} &= \langle n_f L_f||\mathbf{r}||n_\nu L_\nu\rangle \times \sum_{\lambda=-1}^{1} (-1)^\lambda \varepsilon_2^{(-\lambda)} A^{f\nu}_\lambda(1), \\
Q^{F_i m_i J_i}_{F_\nu m_\nu J_\nu} &= \langle n_\nu L_\nu||\mathbf{T}^{(k)}||n_i L_i\rangle \times A^{\nu i}_0(k),
\end{aligned} \tag{3.43}$$

where we introduced the angular coefficient $A_\lambda(k)$ for a k^{th}-order tensor operator $\mathbf{T}^{(k)}$,

$$\begin{aligned} A_\lambda(k) = (-1)^{F'-m'} & \begin{pmatrix} F' & k & F \\ -m' & \lambda & m \end{pmatrix} \\ \times(-1)^{J'+I+F+k} & \sqrt{[F,F']} \begin{Bmatrix} J' & F' & I \\ F & J & k \end{Bmatrix} \\ \times(-1)^{L'+S+J+k} & \sqrt{[J,J']} \begin{Bmatrix} L' & J' & S \\ J & L & k \end{Bmatrix}. \end{aligned} \tag{3.44}$$

It should be noted that $A_0(0) = 1$, as there is no angular coefficient for the $1S - 3S$ excitation.

One can then rearrange the terms to separate radial and angular parts:

$$Q^{F_i m_i J_i}_{F_\nu m_\nu J_\nu} \left(D^{F_\nu m_\nu J_\nu}_{F_f m_f J_f}\right)^* = S_{f\nu i}\ \Omega^{F_i F_\nu F_f}_{J_i J_\nu J_f}, \tag{3.45}$$

with

$$S_{f\nu i} = \langle n_f L_f || \mathbf{r} || n_\nu L_\nu \rangle \langle n_\nu L_\nu || \mathbf{T}^{(k)} || n_i L_i \rangle, \tag{3.46}$$

$$\Omega^{F_i F_\nu F_f}_{J_i J_\nu J_f} = \sum_{m_\nu, \lambda} \varepsilon_2^{(\lambda)} A_0(k) A_\lambda(1). \tag{3.47}$$

Replacing in eq. (3.34), one obtains:

$$\frac{d\sigma}{d\Omega} \propto \sum_{\substack{F_f, J_f, \\ m_i, m_f, \boldsymbol{\varepsilon}_2}} \left| \sum_{F_\nu, J_\nu} \frac{S_{f\nu i}\ \Omega^{F_i F_\nu F_f}_{J_i J_\nu J_f}}{\omega_{\nu i} - 2\omega - i\Gamma_\nu/2} \right|^2. \tag{3.48}$$

It is necessary to sum over $\boldsymbol{\varepsilon}_2$ because the polarization of the scattered photon is not detected.

As in [Amaro2015], the terms can be further rearranged to show direct and cross terms:

$$\begin{aligned} \frac{d\sigma}{d\Omega} \quad \propto \quad & \sum_{F_\nu, J_\nu} \frac{S^2_{f\nu i}\ \Lambda^{F_i F_\nu}_{J_i J_\nu}}{(\omega_{\nu i} - 2\omega)^2 + (\Gamma_\nu/2)^2} \\ & + \mathrm{Re}\left[\sum_{(F'_\nu, J'_\nu) > (F_\nu, J_\nu)} \frac{S_{f\nu i}\ S_{f\nu' i}\ \Xi^{F_i F_\nu F_{\nu'}}_{J_i J_\nu J_{\nu'}}}{(\omega_{\nu i} - 2\omega - i\Gamma_\nu/2)(\omega_{\nu' i} - 2\omega + i\Gamma_{\nu'}/2)} \right] \end{aligned} \tag{3.49}$$

where we have defined

$$\Lambda_{J_i J_\nu}^{F_i F_\nu} = \sum_{\substack{F_f, J_f, \\ m_i, m_f, \varepsilon_2}} \left| \Omega_{J_i J_\nu J_f}^{F_i F_\nu F_f} \right|^2 \quad \text{and} \quad \Xi_{J_i J_\nu J_{\nu'}}^{F_i F_\nu F_{\nu'}} = 2\mathrm{Re} \left[\sum_{\substack{F_f, J_f, \\ m_i, m_f, \varepsilon_2}} \Omega_{J_i J_\nu J_f}^{F_i F_\nu F_f} \left(\Omega_{J_i J_{\nu'} J_f}^{F_i F_{\nu'} F_f} \right)^* \right]. \tag{3.50}$$

Radial part

The two matrix elements in eq. (3.46) can be evaluated in the following way.

$\langle n_f L_f || \mathbf{r} || n_\nu L_\nu \rangle$ is the well-known reduced matrix element of the radial operator $\mathbf{r}$ and can be easily calculated using the Wigner-Eckart theorem

$$\langle nLm | r_\lambda | n'L'm' \rangle = (-1)^{L-m} \begin{pmatrix} L & 1 & L' \\ -m & \lambda & m \end{pmatrix} \langle nL || \mathbf{r} || n'L' \rangle. \tag{3.51}$$

For example, defining ψ_{nLm} as the usual electronic wave function of hydrogen, one has

$$\begin{aligned} \langle 2P(m=0) | z | 3D(m=0) \rangle &= (-1)^{1-0} \begin{pmatrix} 1 & 1 & 2 \\ 0 & 0 & 0 \end{pmatrix} \langle 2P || \mathbf{r} || 3D \rangle \\ &= \int \psi_{210}^*(\mathbf{r})\ z\ \psi_{320}(\mathbf{r})\ d^3\mathbf{r}, \end{aligned} \tag{3.52}$$

where the integral is calculated over the whole space.

The two-photon matrix element has been calculated by M. Haas *et al.* [Haas2006]. It is given by

$$\langle n_\nu L_\nu || \mathbf{T}^{(k)} || n_i L_i \rangle = -\frac{2hc\epsilon_0}{e^2} \beta_{ge}^{(k)}, \tag{3.53}$$

where the coefficients $\beta_{ge}^{(k)} = \beta_{ge}$ for $1S - 3S$ and $\beta_{ge}^{(2)}$ for $1S - 3D$ are given in tables II and III of [Haas2006]. These coefficients are given in $\mathrm{Hz(W/m^2)^{-1}}$.

In our case, the radial part is

$$\begin{aligned} \langle 3S || \mathbf{T}^{(0)} || 1S \rangle &= 1.00333\ C, \\ \langle 3D || \mathbf{T}^{(2)} || 1S \rangle &= -6.16579\ C, \\ \langle 2P || \mathbf{r} || 3S \rangle &= 0.938404\ a_0, \\ \langle 2P || \mathbf{r} || 3D \rangle &= -6.71467\ a_0, \end{aligned} \tag{3.54}$$

where $C = -10^{-5} \times \frac{2hc\epsilon_0}{e^2}$ and a_0 is the Bohr radius. Both constants are global factors and we do not take them into account.

In the numerical calculations, we then simply used

$$S_{f\nu i} = \begin{cases} 1.00333 \times 0.938404 & \text{for } \nu = 3S \\ -6.16579 \times (-6.71467) & \text{for } \nu = 3D \end{cases} \tag{3.55}$$

Angular part

As noted earlier, the quantum interference effect depends only on the angle θ between the incident polarization and the scattering direction. In fact, the coefficients Λ and Ξ have a simple angular dependence and can be parametrized as follows,

$$\begin{aligned} \Lambda^{F_i F_\nu}_{J_i J_\nu}(\theta) &= a_0 + a_2 P_2(\cos\theta), \\ \Xi^{F_i F_\nu F_{\nu'}}_{J_i J_\nu J_{\nu'}}(\theta) &= b_2 P_2(\cos\theta), \end{aligned} \tag{3.56}$$

where P_2 is the second-order Legendre polynomial $P_2(x) = (3x^2 - 1)/2$.

Table 3.2 gives the coefficients of this parametrization for hydrogen: direct terms for each hyperfine transition, and cross terms between the $1S - 3S$ transition and the $1S - 3D$ transitions. In deuterium, the hyperfine structure is different but the method developed above can be directly applied: the radial part is the same (eq. (3.55)), and the angular part should be changed accordingly (Table 3.3).

Table 3.4 presents the coefficient b_2, as defined in eq. (3.56), for the cross terms between the different $3D$ hyperfine sublevels. These cross terms play a negligible role in the distortion and shifting of the $1S - 3S$ line.

F_i	L_ν	F_ν	J_ν	a_0	a_2	b_2
0	0	1	1/2	2/3	0	
	2	2	3/2	4/375	-7/1875	$4\sqrt{2}/75$
	2	2	5/2	2/125	-4/625	$2\sqrt{2}/25$
1	0	1	1/2	2	0	
	2	1	3/2	2/125	-7/2500	$2\sqrt{2}/25$
	2	2	3/2	2/125	-7/2500	$2\sqrt{2}/25$
	2	2	5/2	4/375	-4/1875	$4\sqrt{2}/75$
	2	3	5/2	14/375	-8/625	$14\sqrt{2}/75$

Table 3.2: Angular coefficients for hydrogen, $F_i = 0$ and 1.

F_i	L_ν	F_ν	J_ν	a_0	a_2	b_2
1/2	0	1/2	1/2	4/3	0	
	2	3/2	3/2	8/1875	-14/46875	$8\sqrt{2}/375$
	2	5/2	3/2	32/1875	-224/46875	$32\sqrt{2}/375$
	2	3/2	5/2	32/1875	-224/46875	$32\sqrt{2}/375$
	2	5/2	5/2	28/1875	-184/46875	$28\sqrt{2}/375$
3/2	0	3/2	1/2	8/3	0	
	2	1/2	3/2	4/375	0	$4\sqrt{2}/75$
	2	3/2	3/2	32/1875	0	$32\sqrt{2}/375$
	2	5/2	3/2	28/1875	-14/9375	$28\sqrt{2}/375$
	2	3/2	5/2	8/1875	0	$8\sqrt{2}/375$
	2	5/2	5/2	32/1875	-436/459375	$32\sqrt{2}/375$
	2	7/2	5/2	16/375	-16/1225	$16\sqrt{2}/75$

Table 3.3: Angular coefficients for deuterium, $F_i = 1/2$ and 3/2.

F_i	F_ν	J_ν	$F_{\nu'}$	$J_{\nu'}$	b_2
0	2	3/2	2	5/2	-2/625
1	1	3/2	2	3/2	-7/1250
	1	3/2	2	5/2	-7/1875
	1	3/2	3	5/2	-2/1875
	2	3/2	2	5/2	1/625
	2	3/2	3	5/2	-4/625
	2	5/2	3	5/2	-8/1875
1/2	3/2	3/2	5/2	3/2	-112/46875
	3/2	3/2	3/2	5/2	-112/46875
	3/2	3/2	5/2	5/2	52/46875
	5/2	3/2	3/2	5/2	-16/15625
	5/2	3/2	5/2	5/2	-64/15625
	3/2	5/2	5/2	5/2	-64/15625
3/2	1/2	3/2	3/2	3/2	-56/9375
	1/2	3/2	5/2	3/2	-14/9375
	1/2	3/2	3/2	5/2	-14/9375
	1/2	3/2	5/2	5/2	-16/9375
	1/2	3/2	7/2	5/2	0
	3/2	3/2	5/2	3/2	-56/9375
	3/2	3/2	3/2	5/2	0
	3/2	3/2	5/2	5/2	-208/65625
	3/2	3/2	7/2	5/2	-128/65625
	5/2	3/2	3/2	5/2	2/3125
	5/2	3/2	5/2	5/2	32/21875
	5/2	3/2	7/2	5/2	-144/21875
	3/2	5/2	5/2	5/2	-64/21875
	3/2	5/2	7/2	5/2	-32/65625
	5/2	5/2	7/2	5/2	-1152/153125

Table 3.4: Angular coefficients of cross terms between $3D$ sublevels of hydrogen ($F_i = 0, 1$) and deuterium ($F_i = 1/2, 3/2$).

3.4.3 Results

In order to estimate the frequency shift due to the cross-damping effect, we calculate a simulated signal taking into account the direct and cross terms using eq. (3.49). We then fit the $1S - 3S$ line with a simple Lorentzian function, leaving all fit parameters (position, width, amplitude) free. The shift is defined here as the difference between the position given by the fit and the theoretical position used in the calculation.

We do not add any noise to the simulated spectrum. As we have seen in part 2.6.2, our experimental signal presents a rather large background so the noise can be approximated by a white noise. We have checked that adding a white noise to the simulated signal does not significantly change the result of the fit.

Point-like detector

Figure 3.3(a) shows the simulated signal for hydrogen, $F_i = 1$, in the case of a point-like detector situated directly above the excitation point ($\theta = 0$). The second term on the right-hand side of eq. (3.49) is the signature of quantum interference, and is represented in Fig. 3.3(b). Its dispersion shape is responsible for the shift of the transition frequency. All the results given below are shifts of the laser frequency $\omega/2\pi$, and differ from the atomic transition frequency shifts by a factor of two.

Figure 3.4 shows the frequency shift as a function of the position of a point-like detector. The shift is maximal for $\theta = 0$, and is proportional to $P_2(\cos\theta)$, having the same angular dependence as the amplitude of the cross terms. This fact is not surprising, since the shift is very small compared to the natural linewidth, and can be expected to vary linearly with the amplitude of the cross terms.

This figure is comparable to the results of D. Yost *et al.* (Fig. 5 of [Yost2014]), that were calculated using a completely different method in which the continuous excitation was treated as a special case.

	F_i	Shift (Hz)
H	0	−440
	1	−446
D	1/2	−444
	3/2	−445

Table 3.5: Calculated shift for $\theta = 0$, in Hz.

Table 3.5 gives the maximal shift, calculated for $\theta = 0$, for the four possible hyperfine transitions. It is interesting to notice that we find very similar shifts for the different cases. This is due to the fact that the hyperfine structure of the $3D$ levels is not resolved because it is smaller than the natural linewidth of these levels. The laser frequency shift is thus at most of −0.45 kHz for all $1S - 3S$ transitions, corresponding

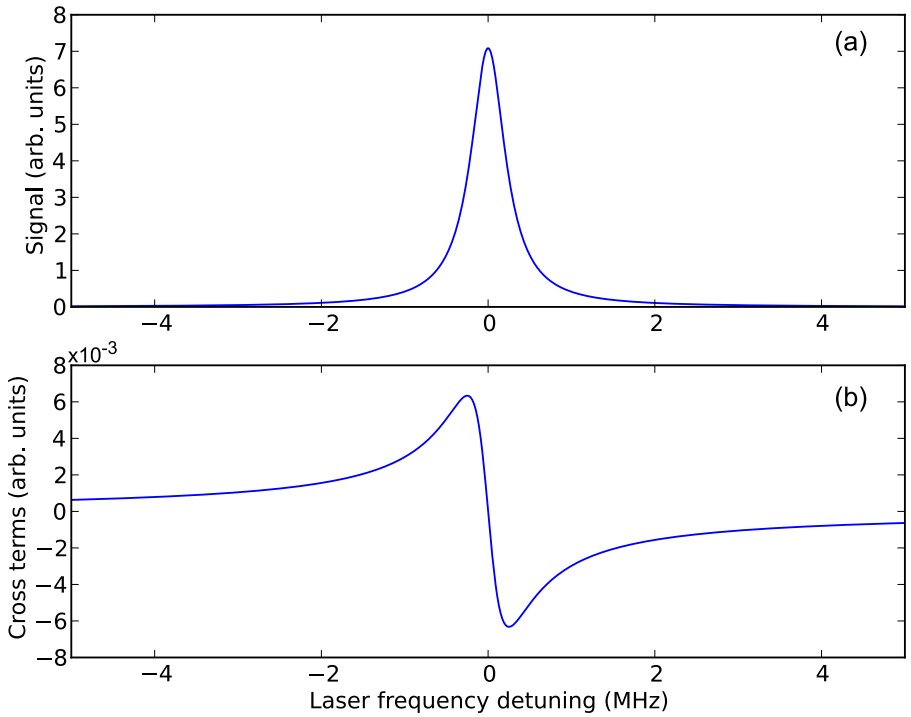

Figure 3.3: (a) Simulated $1S - 3S$ signal for hydrogen, $F_i = 1$, $\theta = 0$. (b) Sum of the cross terms; the arbitrary units are the same as in (a), but the vertical scale is amplified by a factor of 500.

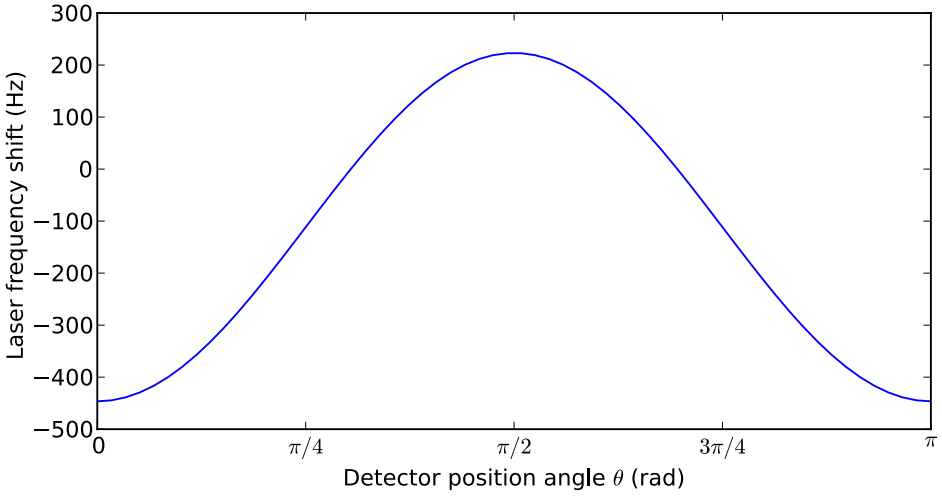

Figure 3.4: Shift of the laser frequency as a function of detector position angle θ.

to an atomic frequency shift of less than 1 kHz. We also find this result if we ignore the hyperfine structure in the calculations.

One can also compare this shift to a naive estimate derived from the simplified case of a three-level atom. The calculation of the first term in eq. (25) of [HORBATSCH2010] would give, with $\Gamma = 1$ MHz and $\Delta \approx 3000$ MHz,

$$\Gamma^2/4\Delta \approx 0.08 \text{ kHz}. \tag{3.57}$$

In fact, this equation, a derivation of which is provided in Appendix A, gives the atomic frequency shift due to a single cross term between excited levels of linewidth Γ and separated by Δ, assuming that $\Gamma \ll \Delta$. But the difference in amplitude between the direct and cross term is missing. In our case, there are several cross-terms, and as we can see in eq. (3.49), these cross terms all have different amplitudes; thus, as detailed in Appendix A, we should take into account the amplitude ratio between each cross term and the direct term, and sum over all $3D$ sublevels ν' interfering with the $3S$ level ν, in order to calculate the total atomic frequency shift

$$\delta \approx \sum_{\nu'} \left[\frac{\Gamma_\nu^2}{4(\omega_{\nu i} - \omega_{\nu' i})} \times \frac{S_{f\nu' i} \times \Xi_{J_i J_\nu J_{\nu'}}^{F_i F_\nu F_{\nu'}}(\theta)}{S_{f\nu i} \times \Lambda_{J_i J_\nu}^{F_i F_\nu}} \right]. \tag{3.58}$$

For $\theta = 0$, this equation gives $\delta/2\pi \approx -0.9$ kHz, which is indeed a very good estimate of the shift.

Extended detector

In order to simulate more closely our experiment, we can integrate the signal over the angular aperture of our imaging system. The point-like detector case for $\theta = 0$ gives an upper bound for the frequency shift; any integration over this angle will only reduce the effect. Furthermore, integrating over the whole space cancels the effect altogether.

The fluorescence collection system is shown in Fig. 3.5. The scattered photons are collected through an aspheric lens of radius 25 mm and an interference filter at 656 nm. A spherical metallic mirror, having the same radius as the lens and situated below the excitation region, increases the solid angle of detection by redirecting photons emitted downwards. The 10° acceptance angle of the interference filter limits the length of the detection region along the atomic beam, which is then a segment of length 12 mm centered on the waist of the 205 nm Fabry-Perot cavity. The center of this detection region is the focal point of the lens as well as the center of curvature of the spherical mirror.

Let us assume for now that the detection region is infinitesimal and centered: in

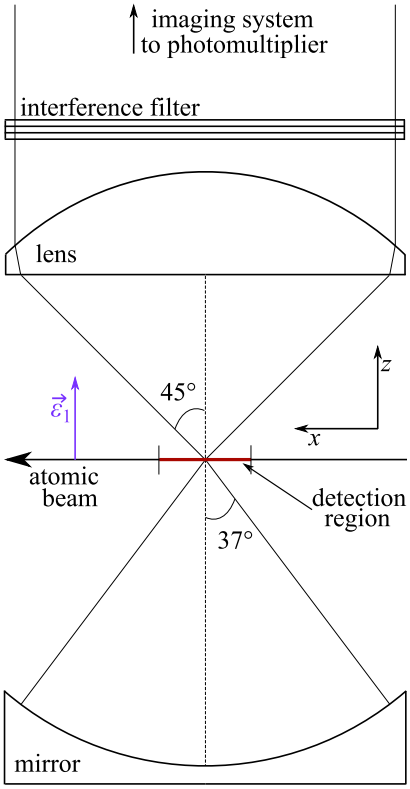

Figure 3.5: Side view of the fluorescence collection system.

this situation, only photons emitted at the center of the cavity are detected. We can first integrate the simulated signal over the upper part of the collection system:

$$Signal = \int_0^{\theta_{max}} f(\theta) 2\pi \sin(\theta) d\theta, \tag{3.59}$$

where $f(\theta)$ is the right-hand side of eq. (3.49), and θ_{max} is the half angle of the detection cone. With $\theta_{max} = 45°$ defined by the diameter of the lens, equation (3.59) leads to a laser frequency shift of -0.27 kHz.

Then, it is possible to calculate the signal for a given position of the emission point along the detection region. As this calculation is rather long, it is presented in Appendix B. The angular acceptance of the filter can be approximated by a step function of the incident angle, so that the distribution of the emission points is assumed to be uniform along the segment. Integrating over the length of the detection region does not change the result significantly (<1 Hz).

We can thus simply add to the previous signal of eq. (3.59) the integral over the downwards-emitted photons reflected by the spherical mirror, with an opening half-

angle of 37°, neglecting the losses due to the reflection on the mirror:

$$Signal = \int_0^{45^\circ} f(\theta) 2\pi \sin(\theta) d\theta \; + \; \int_0^{37^\circ} f(\theta) 2\pi \sin(\theta) d\theta. \tag{3.60}$$

This results in a laser frequency shift of -0.29 kHz.

For a given fluorescence emission direction, the propagation through the optical elements of our detection system could partially polarize the fluorescence light and lead to a polarization dependence of the detection. However, if we except the slanted photocathode, the detection system is cylindrically symmetric around a vertical axis. After integrating over the detection cone while assuming that the detection region is infinitesimal and centered with respect to the detection system, this effect would cancel as all the polarization directions become equally attenuated.

Actually, the photocathode of the photomultiplier makes an angle of 15° with the vertical axis. The effect is then not entirely canceled but very reduced when averaging over all directions. An additional polarization dependence could come from the fact that the detection region is not a point but a horizontal segment. Eventually, taking into account this polarization dependence would change the results obtained for the frequency shifts by less than 10 Hz.

Finally, we obtained a theoretical estimation of the cross-damping shift of the $1S-3S$ transition in H and D. The value of the frequency shift depends on the detector position. In the specific case of our experiment, the laser frequency shift is expected to be of about -0.29 kHz, corresponding to an atomic frequency shift of -0.58 kHz. This value is small compared to the current uncertainty of our measurements. We will nonetheless take into account a shift of $-0.6(2)$ kHz in the final result and the uncertainty budget. The uncertainty of 0.2 kHz that we have retained is much smaller than the other uncertainties in our measurement and has no incidence on the final result.

Conclusion

In this chapter, we have calculated the fitting function used to analyze the experimental data. Several frequency-shifting and broadening effects have been theoretically investigated. The light shift and pressure shift can be important and should be experimentally estimated. The cross-damping shift is small but will be taken into account nonetheless.

Chapter 4

Data analysis and results

In the present chapter, I will describe how the experimental data are analyzed. Each signal is fitted separately with the line profile described in the preceding chapter. The parameters characterizing the velocity distribution are subsequently determined.

To obtain the absolute frequency of the $1S - 3S$ transition, we must apply corrections due to the light shift, then perform a pressure extrapolation to estimate the collisional shift.

4.1 Experimental data

4.1.1 Recordings

From September 2016 to February 2017, we have recorded about 1700 signals ("runs") of the $1S_{1/2}^{F=1} - 3S_{1/2}^{F=1}$ transition during 59 days, following the protocol described in the last section of Chapter 2. Additional recordings of the $m_F = 0$ transition, used for magnetic field calibration, were carried out in November 2016.

We performed measurements for two different pressure values, evaluated as 2.7×10^{-5} mbar (low pressure) and 2×10^{-4} mbar (high pressure). As has been mentioned earlier, this pressure is only known in a relative way, as the gauge is placed on the side of the excitation chamber and not near the atomic beam. We decided to separate the recordings in three data sets: two sets at low pressure (LP1 and LP2) recorded before and after the high pressure set (HP).

For each pressure value, we recorded runs for zero applied magnetic field, and for various magnetic field values around the $3S - 3P$ anticrossing at 180 G (18 mT). We reversed the direction of the magnetic field from one day to the next to avoid any stray electric field. The magnitude B of the vertical magnetic field is deduced from the recorded current, as explained in Chapter 2 (eq. (2.11)). For the LP1 and HP

data sets, the values of the magnetic field B, in gauss, were the following

$$B \in \{-0.3, 170.2, -170.8, 190.3, -190.9\}\ G. \tag{4.1}$$

During the LP2 set, additional B values were used, reaching a total of 15 different magnetic field values after taking into account the offset:

$$B \in -0.3 \pm \{0, 160.1, 165.3, 170.5, 175.2, 185.1, 190.6, 195.0\}\ G \tag{4.2}$$

Each run contains 10 scans of N measurement points, as the AOM frequency is changed following a predefined sequence. As explained in Chapter 2, two different scan widths have been used, corresponding to a number of points $N = 31$ or 51. For each of the $10 \times N$ points, the frequency of the excitation laser is calculated using the different beat note frequencies and the AOM frequency.

Before using the data, we apply a filter to eliminate data points that are obviously wrong. There are two types of problematic points. First, the frequency measure can be inexact. This can occur if one of the laser stabilization loop unlocks, for example. We check that the different beat note frequencies are contained in given intervals. Besides, some beat notes are counted simultaneously on two different counters, so that we can also check that the difference between both counters is small enough, typically lower than 50 Hz.

Secondly, the fluorescence count can drop abnormally. An obvious reason for this is that the lock of the detection cavity length is not very stable and sometimes unlocks for a few seconds, so that the light intensity in the cavity drops. Another, more obscure reason is that for some time, the counter used to record the photomultiplier signal was not well parametered and did not always trigger correctly. This problem was later solved, so that only a few days of recording are concerned. To ensure that all causes are taken into account, we compare both the transmitted UV intensity and the fluorescence count to given thresholds that are redefined for each run.

Eventually, we calculate the average of the ten scans for each of the N frequency points. A "signal" now consists of N {frequency, photon count} points.

4.1.2 Fit with theoretical line profile

As a first step, all the signals are fitted separately with the theoretical line profile $F_{B,\sigma,v_0}(\nu_c, \Gamma, A, C; \nu)$. As a reminder, this profile has been defined in Chapter 3 as

$$F_{B,\sigma,v_0}(\nu_c, \Gamma, A, C; \nu) = A \times (S_{B,\sigma,v_0} * f_{\mathrm{Lor}})(\nu - \nu_c, \Gamma) + C. \tag{4.3}$$

Four parameters are adjusted: the center frequency ν_c, the Lorentzian broadening width Γ, the amplitude A and the background offset C.

The value of the magnetic field B is deduced from the measurement of the power supply of the Helmholtz coils, using eq. (2.11). The parameters σ and v_0 of the velocity distribution will be specified in the next section, for the time being they can remain undefined.

The fit is done using the *optimize.leastsq* routine of Python, which is based on the least-squares method. This method consists in minimizing the quantity

$$S = \sum_{i=1}^{N} [Y_i - F_{B,\sigma,v_0}(\nu_c, \Gamma, A, C; X_i)]^2, \tag{4.4}$$

where X_i are the N frequency points, and Y_i the fluorescence measured for each point. The fit yields the optimal parameters $\nu_{c,\mathrm{opt}}, \Gamma_{\mathrm{opt}}, A_{\mathrm{opt}}, C_{\mathrm{opt}}$ and the corresponding minimal value of S called S_0.

The parameter of interest here is the center frequency ν_c. To determine the uncertainty on the optimal frequency $\nu_{c,\mathrm{opt}}$ obtained by the fit, two methods can be used, giving equivalent results.

- One method makes use of the fractional covariance matrix $\mathscr{C}$ displayed by the Python routine. To take into account the dispersion of the measurements, the variance of the parameters is obtained by multiplying the diagonal terms of this matrix by the residual variance $(\delta Y_i)^2$, defined as

$$(\delta Y_i)^2 = \frac{S_0}{N-4} \tag{4.5}$$

  where S_0 is the minimal value of S as defined earlier, N the number of frequency points (31 or 51 depending on the scan width), and 4 corresponds to the number of parameters in the fit. Hence, the uncertainty on the fit parameter p_n is given by

$$\sigma(p_n) = \sqrt{\mathscr{C}_{nn} \times \frac{S_0}{N-4}} \tag{4.6}$$

  where $\mathscr{C}_{nn}$ is the diagonal term of the fractional covariance matrix corresponding to the parameter p_n.

- The other method consists in minimizing the sum S for different fixed values of the parameter p_n (of which we want the uncertainty) around its optimal value p_n^{opt}, while keeping all the other parameters free. We fit the obtained $S(p_n)$ by a parabolic function defined by

$$S(p_n) = a(p_n - b)^2 + c. \tag{4.7}$$

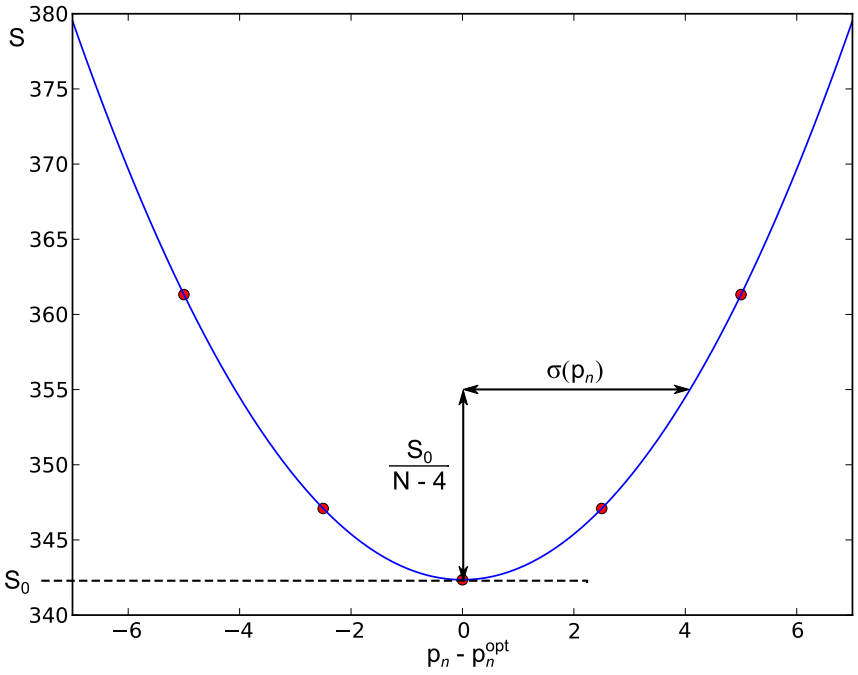

Figure 4.1: The variation of S around the optimal parameter is fitted by a parabolic function. The uncertainty is given by the value of the parameter for which S is increased by an amount of $S_0/(N-4)$.

The uncertainty $\sigma(p_n)$ is then given by

$$\sigma(p_n) = \sqrt{\frac{c}{a(N-4)}} \tag{4.8}$$

This value corresponds to the shift in p_n for which $S(p_n)$ is increased from its minimal value S_0 by an amount of $S_0/(N-4)$, as illustrated in Fig. 4.1. Here 4 is again the number of parameters in the fit. A generalization of this method will be used in the next section, see also Appendix C.

4.2 Determination of the velocity distribution

The velocity distribution, defined in part 3.1.2, depends on two parameters, σ and v_0. In a simplified form, it can be written as

$$f(v,\sigma,v_0) \propto v^3 \exp\left(-\frac{v^2}{2\sigma^2}\right) P[v/\sigma] \exp(-v_0/v). \tag{4.9}$$

We determine the velocity distribution separately for each data set (LP1, LP2, HP). To find the optimal values of the velocity distribution parameters σ and v_0, we perform a chi-square minimization.

4.2.1 Chi-square minimization

First, the fitting procedure described in the previous section is repeated for various values of the velocity distribution parameters σ and v_0, both given in km/s,

$$\begin{aligned} \sigma &\in \{1.2, 1.4, 1.6\}, \\ v_0 &\in \{0.1, 0.5, 1, 1.5, 2, 2.5, 3, 3.5, 4\}. \end{aligned} \tag{4.10}$$

For each pair of values (σ, v_0), we calculate the weighted mean of the center frequency

$$\nu_{\text{mean}} = \frac{\sum_{i=1}^{k} (\nu_i/\sigma_i^2)}{\sum_{i=1}^{k} (1/\sigma_i^2)}, \tag{4.11}$$

where ν_i is the center frequency of run i and σ_i its uncertainty. Here, k denotes the number of runs in a given data set. No distinction of applied magnetic field is made at this point. We then compute the chi-square

$$\chi^2 = \sum_{i=1}^{k} \left[\frac{(\nu_i - \nu_{\text{mean}})^2}{\sigma_i^2} \right]. \tag{4.12}$$

We fit $\chi^2(\sigma, v_0)$ by a polynomial function of degree 2 in σ and degree 3 in v_0, defined as

$$\mathcal{F}(o, a, ..., h; \sigma, v_0) = o + a\sigma + b\sigma^2 + cv_0 + dv_0^2 + e\sigma v_0 + f\sigma^2 v_0 + g\sigma v_0^2 + hv_0^3. \tag{4.13}$$

The surface thus obtained for $\chi^2(\sigma, v_0)$ is somewhat bowl-shaped. We should now find the minimum of this surface and the corresponding (σ, v_0) parameters. In practice, this is done in two steps: first we minimize χ^2 with respect to σ for fixed v_0, then we find the optimum with respect to v_0.

- For 200 fixed values of v_0 around the apparent minimum of χ^2, we calculate the value $\sigma_{\min}(v_0)$ that minimizes χ^2. To this purpose, we can rewrite $\chi^2(\sigma, v_0)$ as a function of the single variable σ,

$$\chi^2(\sigma) = A\sigma^2 + B\sigma + C \quad \text{with} \quad \left| \begin{aligned} A &= b + fv_0 \\ B &= a + ev_0 + gv_0^2 \\ C &= o + cv_0 + dv_0^2 + hv_0^3 \end{aligned} \right. \tag{4.14}$$

  We easily obtain the position and magnitude of the minimum of this parabola

for a given value of v_0,

$$\sigma_{\min}(v_0) = -\frac{B}{2A} = \frac{a + ev_0 + gv_0^2}{2(b + fv_0)} \tag{4.15}$$

$$\chi^2_{\min}(v_0) = \mathcal{F}(\sigma_{\min}(v_0), v_0) \tag{4.16}$$

- We then find the minimum of $\chi^2_{\min}(v_0)$ with respect to v_0. This gives the optimal value of v_0 that we will call $v_{\rm opt}$. From this we obtain the optimal value of σ: $\sigma_{\rm opt} = \sigma_{\min}(v_{\rm opt})$.
- Finally, we get the optimal frequency $\nu_{\rm opt}$ by fitting $\nu_{\rm mean}(\sigma, v_0)$ by a similar polynomial (eq. (4.13)) and calculating the value of this polynomial for the parameters $(\sigma_{\rm opt}, v_{\rm opt})$.

Eventually, all the runs of each data set are fitted with a profile calculated for the corresponding optimal velocity, in the manner described in section 4.1.2. We obtain for each data set, a set of k frequencies $\{\nu_i\}_{\rm opt}$. To double-check our calculation, we can verify that the weighted mean of these newly fitted frequencies is within 100 Hz of the optimal frequency $\nu_{\rm opt}$.

Data set	$\nu_{\rm opt}$	$\sigma_{\rm opt}$	$v_{\rm opt}$	$\chi^2_{\rm opt}$	k	R_B
LP1	734.2(3.9)	1.515(52)	1.23(55)	593	648	0.96
LP2	730.3(2.4)	1.495(32)	1.33(31)	845	636	1.15
HP	713.2(7.1)	1.521(85)	0.87(78)	445	406	1.05

Table 4.1: Optimal values of the frequency and velocity distribution parameters for each data set. Only the last four digits of the frequency are given in the table, $\nu_{\rm opt} = 2\,922\,742\,936\,{\rm xxx.x}$ kHz. $\sigma_{\rm opt}$ and $v_{\rm opt}$ are given in km/s. The table also gives the optimal value of the chi-square, the number of runs k, and the Birge ratio R_B defined below (eq. (4.17)).

The optimal values for each data set are summarized in Table 4.1. Before explaining how the uncertainties are evaluated, I would like to make a few remarks.

The last item in the table is the Birge ratio R_B, defined as

$$R_B = \sqrt{\frac{\chi^2_{\rm opt}}{k-2}} \tag{4.17}$$

where $\chi^2_{\rm opt} = \chi^2(\sigma_{\rm opt}, v_{\rm opt})$ and $k-2$ is the number of degrees of freedom. This ratio should be close to 1 if the data are consistent. As can be seen in Table 4.1, it is indeed the case. In the event when the Birge ratio is greater than 1, it will be used to correct the uncertainties on the optimal parameters.

Another fact I would like to mention is that in the above explanation, the χ^2 surface was fitted using the entire grid of parameters (eq. (4.10)). However, χ^2 can

be approximated by a polynomial close to its minimal value, but has no reason to behave as such for far-off values of σ and v_0. It would then seem preferable to fit the polynomial (4.13) on a reduced parameter grid. For instance, I tried not using the points calculated for $v_0 > 3$. Interestingly, the optimal velocity distribution parameters were both modified but the optimal frequency only changed by 200 Hz.

4.2.2 Uncertainties

The method used here, which is a generalization of the parabola method described earlier, is based on the fact that the uncertainty on a given fit parameter is given by the value of this parameter for which χ^2 is increased by an amount of 1 [Bevington2003]. An explanation of this in a simplified case is given in Appendix C.

Here, since the parameters σ and v_0 are correlated, the uncertainty is calculated simultaneously for the two parameters. In the (σ, v_0) plane, we plot the curve of equation

$$\chi^2(\sigma, v_0) = \chi^2_{\text{opt}} + 1, \tag{4.18}$$

which looks like an ellipse. The uncertainties are defined by the projections of this "ellipse" on the axes, as illustrated in Fig. 4.2.

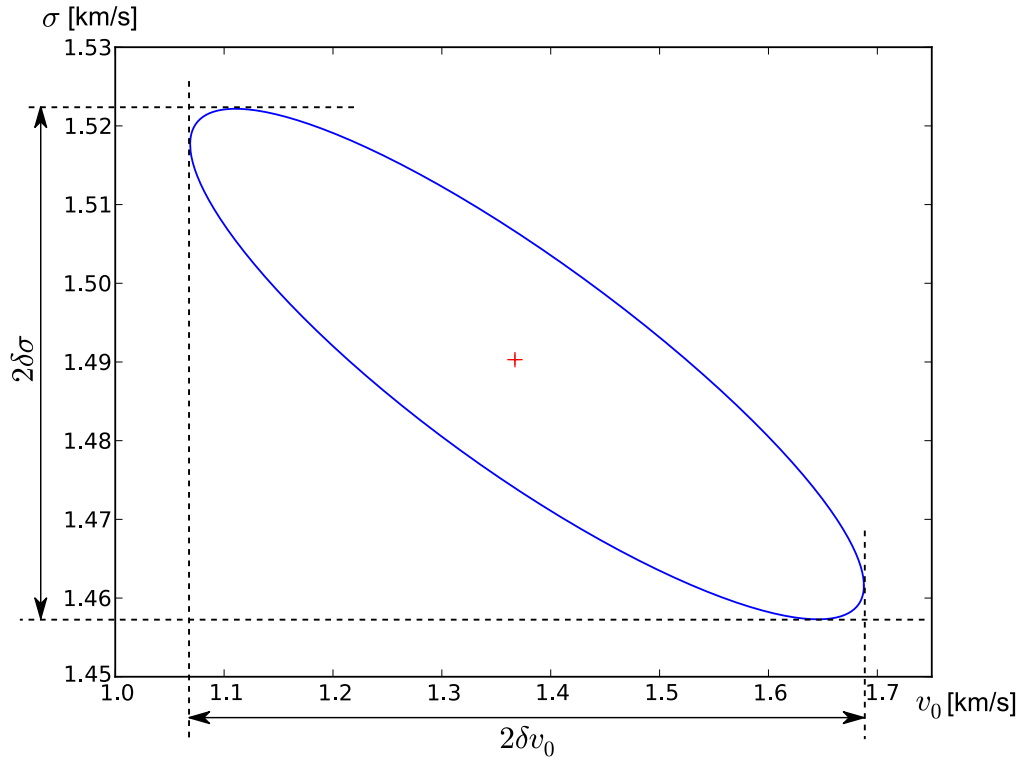

Figure 4.2: The $\chi^2 = \chi^2_{\text{opt}} + 1$ "ellipse" plotted in the (σ, v_0) plane. The projection of the ellipse on the axes defines the uncertainties on the parameters, here denoted $\delta\sigma$ and δv_0. The red cross indicates the optimal values $(\sigma_{\text{opt}}, v_{\text{opt}})$.

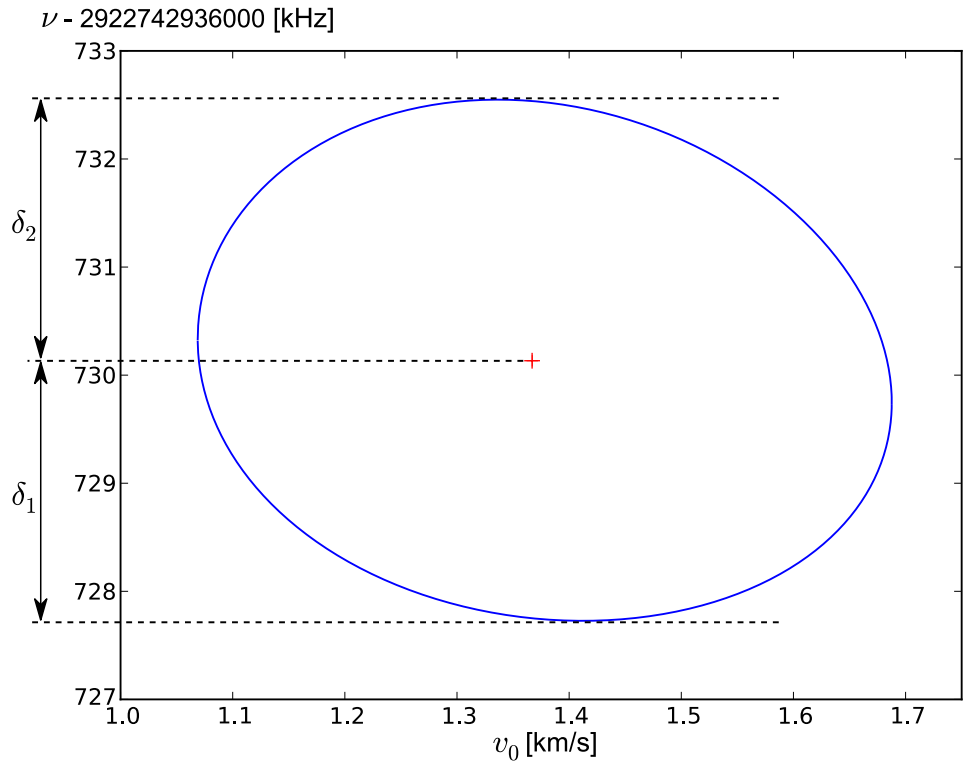

Figure 4.3: The frequency is calculated for each (σ, v_0) verifying eq. (4.18), corresponding to the ellipse on Fig. 4.2. The uncertainty on the frequency is $\delta\nu = \max(\delta_1, \delta_2)$ (this would be important if the curve were very asymmetric, in practice $\delta\nu \simeq \delta_1 \simeq \delta_2$).

In practice, the calculation is done as follows.

- From the 200 values of v_0 used earlier, we keep the values of v_0 for which $\chi^2_{\min}(v_0) < \chi^2_{\text{opt}} + 1$. This gives us the uncertainty on v_{opt}.
- For each v_0 meeting this condition, we calculate the values $\sigma_\pm(v_0)$ such that $\chi^2(\sigma_\pm(v_0), v_0) = \chi^2_{\text{opt}} + 1$.
- The uncertainty on σ_{opt} is then given by $\delta\sigma = \max(\sigma_+ - \sigma_-)/2$, which is simply the half projection of the "ellipse" on the σ axis.

If the Birge ratio R_B, defined in the previous section, is larger than 1, the uncertainties on σ_{opt} and v_{opt} obtained in this way are multiplied by R_B to take into account the experimental dispersion of measurements. That is equivalent to using the curve defined by $\chi^2 = \chi^2_{\text{opt}} + R_B^2$.

To determine the uncertainty on ν_{opt}, this ellipse is projected on the frequency surface. In other words, we calculate the frequency corresponding to the parameters (σ, v_0) along the ellipse, using the polynomial interpolation as before. The uncertainty on the frequency is given by the maximal distance of this curve from the optimal frequency. Figure 4.3 shows an example of this frequency "ellipse", calculated for each (σ, v_0) verifying eq. (4.18), and the definition of the uncertainty.

4.3 Correction of systematic effects

We have obtained the frequency for different values of the pressure. We should then realize an extrapolation to zero pressure to determine the frequency corrected from the collisional shift. Beforehand, it is however necessary to correct each frequency point from the light shift, which depends on the light intensity experienced by the atoms.

4.3.1 Light shift

To correct the values of table 4.1 from the light shift, we apply to the frequencies $\{\nu_i\}_{\text{opt}}$, obtained with the optimal velocity distribution, a correction based on a parameter linked to the light power inside the build-up cavity.

We have access to two such parameters. One of them is the voltage $\mathscr{A}_{UV}$ of the photodiode recording the transmitted UV power. The other is the height H of the transition profile, which is proportional to the square of the light intensity. We define this height, expressed in photon counts per second (cnts/s), as the difference between the maximal photon count and the background offset, for a null magnetic field.

For a given non-zero magnetic field, the height is corrected by taking into account its theoretical variation, which is due to two different reasons. First, the $m_F = 0$ sub-transition does not contribute to the signal for $B \neq 0$ because of the Zeeman effect. Secondly, near the anticrossing at 180 G, the Stark mixing of the $3S(m_F = -1)$ sublevel with the $3P$ level induces a broadening of the $m_F = -1$ sub-transition which further reduces the signal height.

Figure 4.4 shows the square root of the signal height as a function of the UV photodiode amplitude. Each point corresponds to one run. For the sake of clarity, I have represented only signals recorded at zero magnetic field and low pressure. If both parameters depended linearly on the light intensity, we would expect to see the points aligned diagonally. It appears that it is indeed the case, but with a slope which varies discontinuously every few days. The abrupt changes take place when the optical alignment of the power build-up cavity is modified.

The choice of colors underlines the different slopes for each group of days. For the first four groups (a to d), where the light intensity at the entrance of the cavity was rather stable, the photodiode amplitude varied widely between the subsets, whereas the height of the signal was more constant. The parameter $\sqrt{H}$ seems to be a more faithful indicator of the light intensity inside the build-up cavity.

For this reason, we decided to use the square root of the signal height, corrected from its theoretical variation with the magnetic field, as an indicator of the light intensity experienced by the atoms.

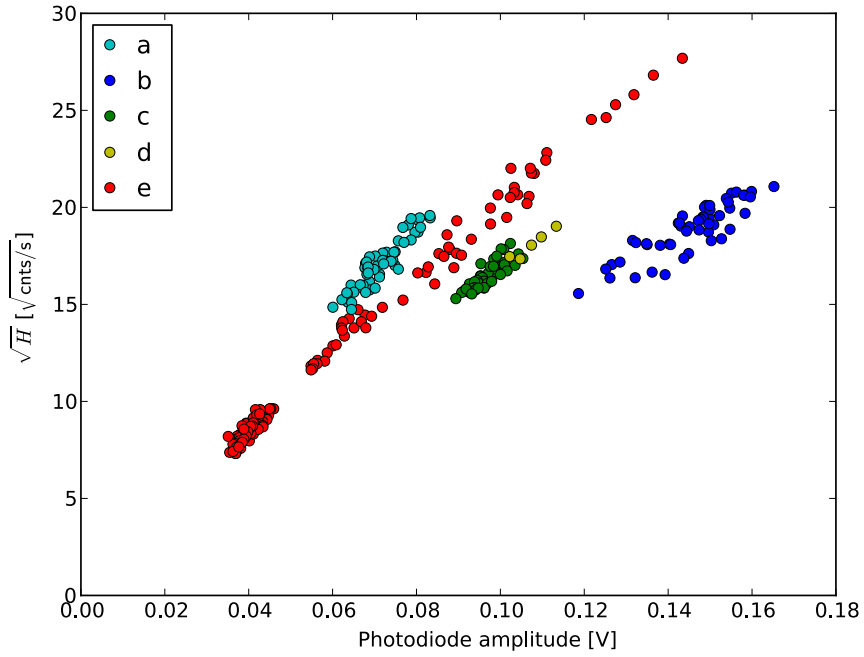

Figure 4.4: Square root of signal height as a function of the UV photodiode amplitude. Each point corresponds to a single run, recorded at zero magnetic field and low pressure. They have been grouped by day. a: first 2 days, b: next 3 days, c: last day before high pressure, d: first day after high pressure, e: four last days where the incoming light power was varied by hand to better quantify the light shift. The build-up cavity mirrors were cleaned just before these last four days, explaining the larger signal height.

For each data set, we must determine a light shift coefficient ξ and apply a correction to the frequencies $\{\nu_i\}_{\text{opt}}$,

$$\nu_i^{corr}(\xi) = \nu_i - \xi\sqrt{H}. \tag{4.19}$$

The weighted mean is calculated as in eq. (4.11),

$$\nu_{\text{mean}}^{corr}(\xi) = \frac{\sum_{i=1}^{k}(\nu_i^{corr}(\xi)/\sigma_i^2)}{\sum_{i=1}^{k}(1/\sigma_i^2)}, \tag{4.20}$$

and yields the corrected frequency for this data set.

To quantify the light shift and determine a correction coefficient, we varied manually the light intensity during the last four days of recording, which are part of the LP2 data set (red points labeled e on Fig. 4.4). Figure 4.5 shows, for each run of this subset, the center frequency with its uncertainty as a function of $\sqrt{H}$, the square root of the signal height. This data was fitted with a linear model. The slope of the linear fit gives the light shift coefficient $\xi_{\text{LP}} = 595 \pm 172$ Hz/$\sqrt{\text{cnts/s}}$.

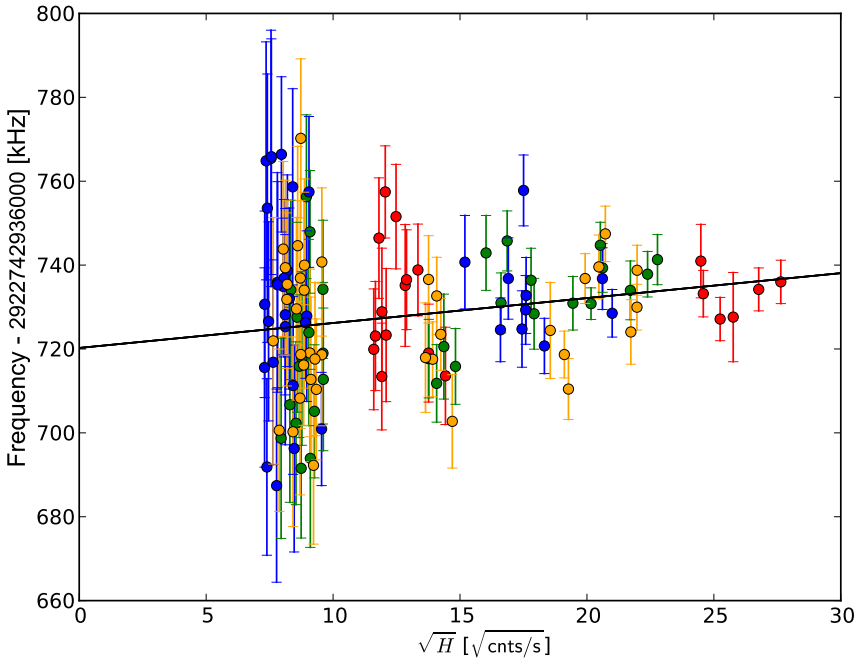

Figure 4.5: Frequency as a function of the square root of signal height. The signals of the last four days of the LP2 data set were fitted using the optimal velocity distribution $(\sigma, v_0)_{\text{LP2}} = (1.495, 1.33)$. Each color corresponds to one day. The black line is a linear fit of the data, of slope 595 ± 172 Hz$/\sqrt{\text{cnts/s}}$.

This coefficient is used for the two low-pressure data sets (LP1 and LP2).

As the signal height depends on the pressure, the coefficient obtained at low pressure has no reason to be valid for the high-pressure data set. For this reason, we must determine a different coefficient for the HP set. However, the light intensity did not vary enough during the high-pressure recordings to allow us to recover a precise correction coefficient. Nevertheless, we decided to deduce the high-pressure correction by minimizing the chi-square χ^2 with respect to the light shift coefficient ξ. This is actually equivalent to performing an extrapolation using the entire HP data set.

For different values of ξ, we calculate $\nu^{corr}_{\text{mean}}(\xi)$ as defined in eq. (4.20), then the chi-square

$$\chi^2(\xi) = \sum_{i=1}^{k} \left[\frac{(\nu_i^{corr}(\xi) - \nu^{corr}_{\text{mean}}(\xi))^2}{\sigma_i^2} \right]. \tag{4.21}$$

The obtained $\chi^2(\xi)$ is fitted by a parabola. The position of the minimum of this parabola gives the optimal coefficient ξ_{HP} for high-pressure measurements. The uncertainty on this coefficient is defined by the value of ξ for which $\chi^2(\xi)$ is increased from its minimum value by an amount of the Birge ratio R_B as defined in eq. (4.17). In this case, $R_B = 1.1$. We thus obtain the coefficient for the high-pressure data set, $\xi_{\text{HP}} = 531 \pm 819$ Hz$/\sqrt{\text{cnts/s}}$.

Data set	ν_{opt}	δ_{LS}	ν_{corr}
LP1	734.2(3.9)	−10.4(3.0)	723.8(4.9)
LP2	730.3(2.4)	−12.1(3.5)	718.2(4.3)
HP	713.2(7.1)	−6.3(10.2)	706.9(12.4)

Table 4.2: The uncorrected frequency, light shift correction and corrected frequency for each data set, expressed in kHz. As in Table 4.1, only the last four digits of the transition frequency are shown: $\nu = 2\,922\,742\,936\,\text{xxx.x}$ kHz. The uncertainty on the corrected frequency is obtained as explained in the text.

Eventually, the corrected frequencies $\nu^{corr}_{\text{mean}}(\xi)$ are calculated for each data set using the corresponding coefficient ξ_{LP} or ξ_{HP}. The uncertainty on the resulting frequency shift $\delta_{LS} = \nu^{corr}_{\text{mean}} - \nu_{\text{opt}}$ is deduced from the uncertainty on the coefficient ξ. The final uncertainty on the corrected frequency can be obtained by adding in quadrature this uncertainty and that of ν_{opt} determined in the preceding section.

Table 4.2 summarizes the light shift corrections and the resulting frequencies.

4.3.2 Pressure shift

Using the frequencies corrected from the light shift, we can now perform the pressure extrapolation to determine the absolute $1S - 3S$ frequency. The pressure here is measured by the ionization gauge and is not the pressure "inside" the atomic beam.

We assume here that the frequency depends linearly on the pressure. This was verified experimentally during Sandrine Galtier's Ph.D., where the collisional shift was determined using three different pressure values.

The extrapolation, shown on Fig. 4.6, is realized using the linear least-squares method described in Appendix C (eq. (C.2)). We add a correlation between the two low-pressure sets because the light shift correction was done using the same coefficient for both sets. The covariance matrix V of the measurements is thus defined with non-diagonal terms between the LP1 and LP2 data sets, equal to the product of the light shift uncertainties of these two sets.

The slope of the linear fit gives a pressure shift coefficient of −77(75) MHz/mbar. The collisional shift is negative, as predicted by the theory mentioned in Chapter 3, part 3.2.2. The intercept yields the frequency at zero pressure

$$\nu = 2\,922\,742\,936\,722.3(4.9)\ \text{kHz}. \tag{4.22}$$

The uncertainties are obtained from the diagonal terms of the covariance matrix G as defined in Appendix C.

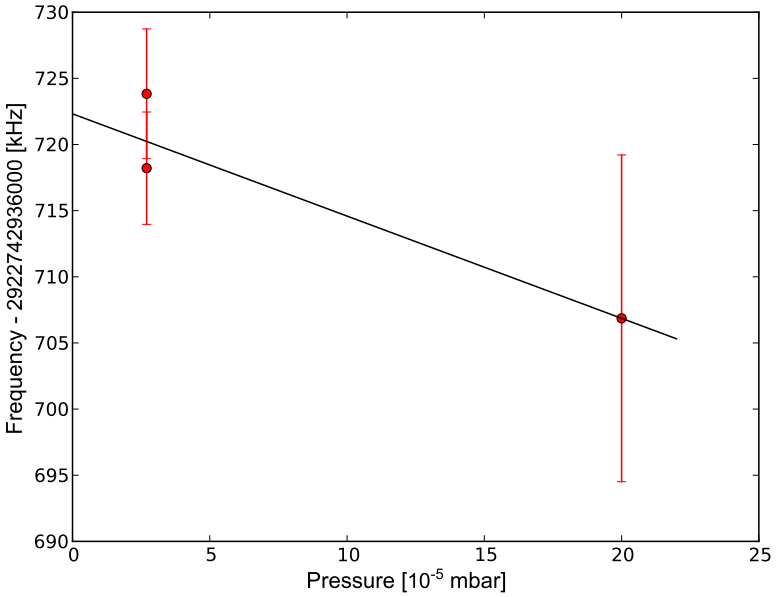

Figure 4.6: Pressure extrapolation. The slope of the linear fit is the pressure shift coefficient −77(75) MHz/mbar.

4.4 Final result

4.4.1 1*S*–3*S* transition frequency

As explained in Chapter 3, the final result should be corrected from the cross-damping shift, which has been theoretically estimated at −0.6(2) kHz. One should thus add a positive correction of +0.6(2) kHz to the value of eq. (4.22) to obtain

$$\nu_{1S-3S}^{F=1} = 2\,922\,742\,936\,722.9(4.9)\ \text{kHz}. \tag{4.23}$$

The applied magnetic field is only known with an uncertainty of about 100 mG, as mentioned in Chapter 2. The influence of this uncertainty on the measured frequency can be estimated theoretically. Near the anticrossing at 180 G, where the theoretical variation of the frequency with the magnetic field due to the Stark effect is largest, a change in magnetic field of 100 mG would induce a frequency shift of about 600 Hz. For this reason, we add in quadrature a global uncertainty of 0.6 kHz to our result.

To obtain the centroid frequency of the $1S-3S$ transition, one must use the hyperfine splittings whose values have been discussed in Chapter 1, part 1.1.3. One has

$$\begin{aligned} &\nu_{1S-3S}^{\text{centroid}} = \nu_{1S-3S}^{F=1} + \frac{1}{4}\Delta E_{\text{HFS}}(1S) - \frac{1}{4}\Delta E_{\text{HFS}}(3S), \\ &\text{with} \left| \begin{array}{l} \Delta E_{\text{HFS}}(1S) = 1\,420\,405.752\ \text{kHz}, \\ \Delta E_{\text{HFS}}(3S) = 52\,609.44(1)\ \text{kHz}. \end{array} \right. \end{aligned} \tag{4.24}$$

Finally, the centroid frequency is

$$\nu_{1S-3S} = 2\,922\,743\,278\,672.0(4.9)\ \text{kHz}. \tag{4.25}$$

The 4.9 kHz uncertainty corresponds to a relative uncertainty of 1.7×10^{-12}.

4.4.2 Rydberg constant, Lamb shift and proton charge radius

Combining our result with the very precisely known $1S - 2S$ transition frequency [Parthey2011], we can derive a value of the Rydberg constant and $1S$ Lamb shift. The method followed here is similar to the calculation described in Chapter 1, part 1.2.2.

Using eq. (1.9), we can write the energy differences as

$$E_{1S-2S} = E_{2S}^{DR} - E_{1S}^{DR} + L_{2S} - L_{1S} \tag{4.26}$$

$$E_{1S-3S} = E_{3S}^{DR} - E_{1S}^{DR} + L_{3S} - L_{1S} \tag{4.27}$$

In order to determine the Lamb shift L_{1S}, we need to eliminate the main contribution to the Dirac-recoil term E_{nJ}^{DR}. As a reminder, this contribution scales as $1/n^2$. An appropriate linear combination of eqs. (4.26) and (4.27) leads to

$$32E_{1S-2S} - 27E_{1S-3S} = 32L_{2S} - 27L_{3S} - 5L_{1S} + \Delta^{DR} \tag{4.28}$$

where $\Delta^{DR} = 32E_{2S}^{DR} - 27E_{3S}^{DR} - 5E_{1S}^{DR}$ is an exactly known function of α and $m_\mathrm{e}/m_\mathrm{p}$ and does not depend significantly on the value of the Rydberg constant. Using the CODATA-2014 recommended values [Mohr2016], one has

$$\Delta^{DR}/h = 87\,470\,296.44(4)\ \text{kHz}, \tag{4.29}$$

the uncertainty being due to that of the fine-structure constant α.

In the same manner as in Chapter 1, one can now make use of the fact that most contributions to the Lamb shift vary as $1/n^3$. We can write

$$L_{nS} = \frac{1}{n^3}(L_{1S} + \Delta_n), \tag{4.30}$$

where the differences Δ_n are very precisely known theoretically and have been published in [Czarnecki2005]. In particular, for $n = 2$ and 3, one has

$$\Delta_2/h = 187\,225.70(5)\ \text{kHz}, \tag{4.31}$$

$$\Delta_3/h = 235\,070.90(7)\ \text{kHz}. \tag{4.32}$$

Replacing in eq. (4.28), and solving for L_{1S}, one obtains

$$L_{1S} = -16E_{1S-2S} + 13.5E_{1S-3S} + 2\Delta_2 + 0.5(\Delta^{DR} - \Delta_3). \tag{4.33}$$

This yields

$$L_{1S}/h = 8\,172\,847(66)\ \text{kHz} \tag{4.34}$$

To find the value of the Rydberg constant R_∞, which is hidden inside the Dirac-recoil term E_{nS}^{DR}, one can use eq. (4.26) again. It can be rewritten as

$$E_{2S}^{DR} - E_{1S}^{DR} = E_{1S-2S} + \frac{1}{8}(7L_{1S} - \Delta_2). \tag{4.35}$$

The obtained value,

$$R_\infty = 10\,973\,731.568\,55(26)\ \text{m}^{-1}, \tag{4.36}$$

agrees with the value recommended by the latest CODATA adjustment [Mohr2016],

$$R_\infty^{\text{CODATA}} = 10\,973\,731.568\,508(65)\ \text{m}^{-1}. \tag{4.37}$$

From the $1S$ Lamb shift determined above, assuming that the QED calculations are correct, one can derive a value of the proton charge radius,

$$r_p = 0.879(25)\ \text{fm}. \tag{4.38}$$

This is four times less precise, but in good agreement with the CODATA-2014 recommended value [Mohr2016]

$$r_p^{\text{CODATA}} = 0.8751(61)\ \text{fm}. \tag{4.39}$$

4.4.3 New analysis of Sandrine Galtier's recordings

At the end of Sandrine Galtier's Ph.D. in 2014, there remained an unresolved question: whether the atomic velocity distribution depends, or not, on the pressure. Depending on the assumption that was made, the final result varied by 10 kHz. The proton radius deduced from her measurements agreed either with the CODATA recommended value, or with the value deduced from muonic hydrogen spectroscopy.

The measurements realized in the present work have allowed to give an answer to this question: the velocity distribution does not seem to depend significantly on the pressure, at least within the uncertainties of Table 4.1. To corroborate this statement, I have fitted some of the low-pressure signals using the three optimal velocity distributions. The obtained frequencies differ by 2 to 3 kHz at the most.

In the light of this result, it is possible to revisit Sandrine Galtier's measure.

During her Ph.D., she had estimated the velocity distribution for a single pressure value. To determine the collisional shift, she had carried out measurements, in a single day, for three pressure values at zero applied magnetic field. When analyzing these recordings, we should now use the same velocity distribution for all pressure values. The slope of a linear fit yields the collisional shift coefficient. To take into account the uncertainty on the velocity distribution determination, an uncertainty of 3 kHz divided by the maximal pressure difference is added in quadrature to that of the obtained collisional shift coefficient.

The data recorded during her Ph.D. have been entirely reanalyzed by François Biraben. The collisional shift is obtained using a more complete data set than the one she presented in her manuscript. The cross-damping effect is taken into account by adding a correction of $+0.6(2)$ kHz. The $1S-3S$ transition frequency resulting from this new analysis of S. Galtier's data is

$$\nu_{1S-3S} = 2\,922\,743\,278\,672.2(2.8)\ \text{kHz}. \tag{4.40}$$

It is in good agreement with our new measurement given in eq. (4.25). The smaller uncertainty is mainly due to a higher power of the 205-nm excitation laser (reaching 15 mW), yielding a better signal-to-noise ratio.

I would like to point out that although the experimental setup was essentially the same for both measurements, several differences must be emphasized. The frequency of the Verdi laser is now measured with two separate beat notes using an additional laser to convert the frequency to the infrared domain, instead of making a simple beat note with the frequency comb at 532 nm.

Moreover, the ionization gauge used to measure the pressure broke down at the beginning of my Ph.D., and was replaced by a used gauge which was not well calibrated. The pressure measurements cannot be compared directly. Indeed, the value, as measured by the gauge, of the pressure for which the signal was optimal, was not the same for the two recording sessions (8×10^{-5} mbar for S. Galtier, 2.7×10^{-5} mbar in our case). Besides, this type of gauge is known for not being very sensitive to hydrogen.

Yet another difference is the way the light power in the cavity was estimated for the light shift correction. For S. Galtier's recordings, the transmitted power was measured directly using a UV photodiode. Furthermore, the light power varied sufficiently during the entire recording session to determine the light shift coefficient by performing an extrapolation with respect to this transmitted power using the entire data set, averaged over each day. This, along with the higher UV power, allowed a more precise determination of the light shift.

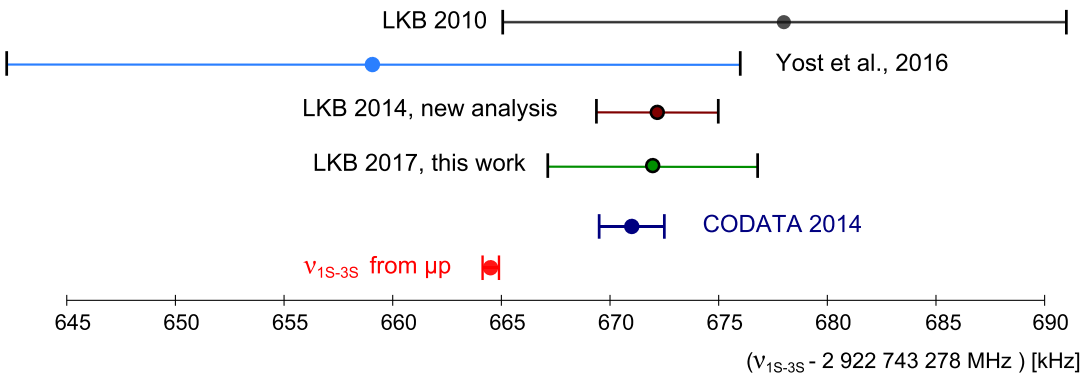

Figure 4.7: Comparison of our measurement (LKB 2017) with other determinations of the $1S-3S$ transition frequency.

Figure 4.7 shows our new measurement (labeled LKB 2017) along with the new analysis of Sandrine Galtier's data (LKB 2014), our last published result (LKB 2010, [Arnoult2010]), and the recently published measure in Garching with a picosecond frequency comb excitation [Yost2016]. Two theoretical values are also represented, calculated either using the CODATA-2014 recommended constants, or using the proton radius and Rydberg constant deduced from the muonic hydrogen (μp) spectroscopy.

Conclusion

We have recorded many runs over several months, while varying the magnetic field for different pressure values. Each signal was fitted using a theoretical line profile. We then performed a chi-square minimization to determine the velocity distribution parameters. This was done separately for three data sets corresponding to two different pressure values.

The light shift has then been included in the analysis, by applying a correction derived from the variation of the frequency with the square root of the signal height. A linear extrapolation to zero pressure yields a value of the $1S-3S$ transition frequency in good agreement with the CODATA value.

Furthermore, we have found that the velocity distribution does not depend significantly on the pressure. Considering this result, Sandrine Galtier's data has been reanalyzed, yielding a transition frequency which agrees very well with our new measurement.

Conclusion

This work has allowed to perform a new measurement of the $1S - 3S$ transition frequency of hydrogen, yielding the value

$$\nu_{1S-3S} = 2\,922\,743\,278\,672.0(4.9)\ \text{kHz}.$$

It has involved an important experimental work, including an improvement of the frequency measurement of our green laser, which is now performed using an additional laser to convert the measured frequency to the infrared domain. A months-long recording session was necessary to characterize the atomic velocity distribution for various pressure values, in order to determine both the second-order Doppler shift and the collisional shift. Other systematic effects had to be taken into account, most importantly the light shift, which requires to estimate the light intensity experienced by the atoms. The cross-damping shift was studied theoretically in detail, but it is very small in our experimental situation.

This measure has shown that the velocity distribution of the atoms does not depend significantly on the pressure. In view of this result, it was possible to reanalyze the data of Sandrine Galtier's Ph.D. thesis. The resulting frequency

$$\nu_{1S-3S} = 2\,922\,743\,278\,672.2(2.8)\ \text{kHz}$$

is in very good agreement with the one obtained in the present work, despite several differences between the two data sets. Indeed, three years have passed between the two recording sessions, and several changes were made on the experiment during this time. In addition to the modification of the frequency measurement of the 532-nm laser, the pressure gauge was replaced, so that the collisional shift cannot be directly compared. The light power experienced by the atoms was also estimated differently.

Both the new measure and the reanalyzed data are in agreement with the value predicted by the CODATA.

In particular, the result of this work yields a value of the proton charge radius

$$r_p = 0.879(25) \text{ fm}$$

which is in good agreement with the CODATA-2014 value ($r_p = 0.8751(61)$ fm), thus reinforcing the proton radius puzzle.

Outlook

In the coming months, we plan to start measuring the $1S - 3S$ transition frequency again, this time using hydrogen atoms cooled to the temperature of liquid nitrogen with the cooling system presented in Chapter 2. This would reduce the second-order Doppler effect by a factor of 4, so that our measurement should be less sensitive to the determination of the velocity distribution. We have installed the cooling system in the final months of my Ph.D., and in the very last days of July 2017, we have been able to observe the transition for the first time with cooled hydrogen. An average of 19 runs is shown in Fig. 4.8. Our frequency measurement is only relative because the frequency comb was switched off. Besides, the BBO crystal used for the 205-nm generation was old and not very efficient, yielding less than 4 mW of 205-nm light. By comparing this signal, to other recordings realized on the same day with room-temperature hydrogen, we were nonetheless able to see the frequency shift (very roughly 100 kHz) due to the change in velocity. Several technical issues still have to be overcome before starting a recording session. The $1S - 3S$ metrology of cooled hydrogen will be performed by Simon Thomas during his Ph.D.

Another future goal for this experiment will be the metrology of the $1S - 3S$ transition of deuterium. It is rather straightforward to modify the excitation laser frequency in order to reach this transition. In this work, we have been able to observe the deuterium $1S - 3S$ transition for the first time with a continuous-wave laser.

In a more long-term perspective, the UV laser source could be modified to reach the two-photon $1S - 4S$ hydrogen/deuterium transition at 194 nm, which has never been observed yet. An advantage of this transition is that it has a narrower natural width of 700 kHz, as compared to 1 MHz for the $1S - 3S$ transition. Moreover, a small part of the atoms excited to the $4S$ state would decay by a radiative cascade to the metastable $2S$ state, from which it could be possible to probe the velocity distribution through a one-photon transition. This would allow to cross-check our current method of velocity distribution determination.

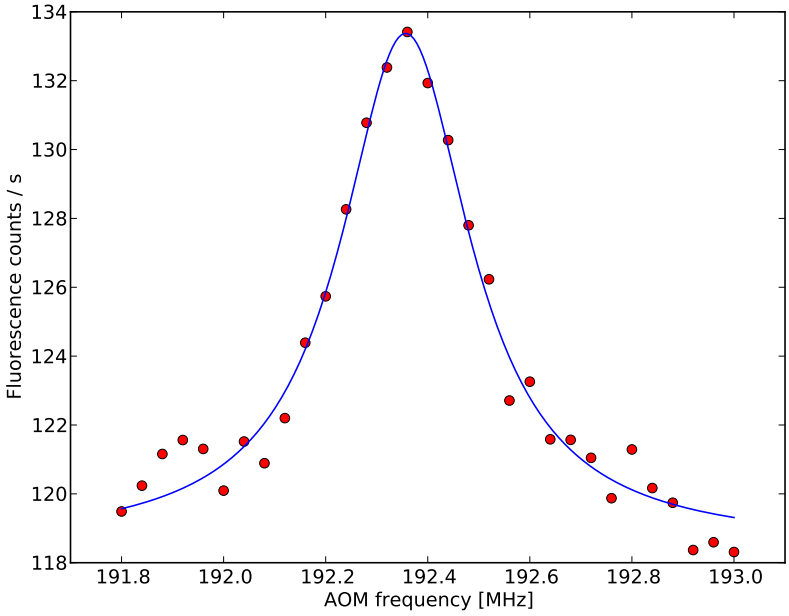

Figure 4.8: The first observation of the $1S - 3S$ transition with cooled hydrogen. Red points are the average of 19 runs, the blue line is a Lorentzian fit. The AOM frequency should be multiplied by 4, and reversed, to get a relative atomic frequency scale. The incident 205-nm light power was about 3.8 mW. The temperature of the nozzle was estimated at about 120 K, with a pressure of 2×10^{-5} mbar inside the interaction chamber.

Appendix A

Estimate of cross-damping shift

In this section I derive an approximate value of the frequency shift, assuming that the interfering levels are very far from resonance and of small linewidth. I thus show that, under this assumption, it is possible to obtain a very good estimate of the QI shift without any fitting procedure.

Let us assume, in a first step, that there are only two transitions of width Γ and Γ' separated by Δ. Denoting ω the atomic frequency detuning with respect to the first transition, the signal can be written as

$$\text{Signal} = \left| \frac{A}{\omega + i\Gamma/2} + \frac{B}{\omega - \Delta - i\Gamma'/2} \right|^2, \tag{A.1}$$

where A and B are the respective amplitudes of the two transitions. We then expand this expression around the $\omega = 0$ resonance, assuming that $\omega \ll \Delta$ and $\Gamma, \Gamma' \ll \Delta$ (*c.c.* means complex conjugate),

$$\begin{aligned}
\text{Signal} &= \frac{A^2}{\omega^2 + \Gamma^2/4} + \frac{B^2}{(\omega - \Delta)^2 + \Gamma'^2/4} + \frac{AB}{(\omega + i\Gamma/2)(\omega - \Delta - i\Gamma'/2)} + c.c. \\
&\sim \frac{A^2}{\omega^2 + \Gamma^2/4} + \frac{2AB(\omega(\omega - \Delta) + \Gamma^2/4)}{(\omega^2 + \Gamma^2/4)((\omega - \Delta)^2 + \Gamma^2/4)} \\
&\sim \frac{A^2}{\omega^2 + \Gamma^2/4} + 2AB \frac{\Delta}{\Delta^2 + \Gamma^2/4} \times \frac{-\omega}{\omega^2 + \Gamma^2/4} \\
&\sim \frac{\mathcal{A}}{\omega^2 + \Gamma^2/4} - \frac{\mathcal{B}}{\Delta} \times \frac{\omega}{\omega^2 + \Gamma^2/4}
\end{aligned} \tag{A.2}$$

In the last line, we have defined $\mathcal{A} = A^2$ and $\mathcal{B} = 2AB$, and assumed that

$$\frac{\Delta}{\Delta^2 + \Gamma^2/4} \sim \frac{1}{\Delta}.$$

The obtained expression (eq. (A.2)) is valid for ω close to 0, and shows a Lorentzian profile distorted by a dispersion-shaped cross term.

Then we can follow [JENTSCHURA2002] to derive an estimate of the shift, rewriting eq. (A.2) as

$$\begin{aligned} \text{Signal} &\sim \frac{\mathcal{A}-\mathcal{B}\omega/\Delta}{\omega^2+\Gamma^2/4} \\ &\sim \frac{\mathcal{A}}{[\omega-\delta(\omega)]^2+\Gamma^2/4} \end{aligned} \tag{A.3}$$

with

$$\delta(\omega) = \frac{\mathcal{B}}{2\mathcal{A}\Delta}\left(\omega^2+\Gamma^2/4\right) \tag{A.4}$$

The shift of the half-maximum points is then

$$\delta(\Gamma/2) = \frac{\mathcal{B}}{\mathcal{A}}\frac{\Gamma^2}{4\Delta}. \tag{A.5}$$

Note that the shift of the maximum position is twice smaller

$$\delta(0) = \frac{\mathcal{B}}{\mathcal{A}}\frac{\Gamma^2}{8\Delta}. \tag{A.6}$$

Now, we can compare eq. (A.1) and eq. (3.49) to define, with $\nu = 3S$ and ν' denoting any interfering $3D$ sublevel,

$$\mathcal{A} = S^2_{f\nu i}\Lambda^{F_iF_\nu}_{J_iJ_\nu} \tag{A.7}$$

$$\mathcal{B} = S_{f\nu i}S_{f\nu' i}\Xi^{F_iF_\nu F_{\nu'}}_{J_iJ_\nu J_{\nu'}}(\theta) \tag{A.8}$$

$$\Delta = \omega_{\nu i} - \omega_{\nu' i} \tag{A.9}$$

$$\Gamma = \Gamma_\nu \tag{A.10}$$

Then we sum over the different ν' levels to obtain the shift of the half-maximum points of the $1S-3S$ line,

$$\delta(\Gamma_\nu/2) \approx \sum_{\nu'}\left[\frac{\Gamma^2_\nu}{4(\omega_{\nu i}-\omega_{\nu' i})} \times \frac{S_{f\nu' i}\ \Xi^{F_iF_\nu F_{\nu'}}_{J_iJ_\nu J_{\nu'}}(\theta)}{S_{f\nu i}\ \Lambda^{F_iF_\nu}_{J_iJ_\nu}}\right]. \tag{A.11}$$

Appendix B

Integration of the fluorescence over the detection region

The purpose of the following calculation is to determine how to integrate the fluorescence signal emitted upwards, when the emission point is not in the center of the system, but at a given point in the detection region.

This detection region is along the x axis. It is formally equivalent to shift the emission point with respect to the lens or vice versa. In this calculation, we will keep the emission point as the origin of the coordinates, and shift the center of the lens along the x axis to a new position x_0. In our case, we always have $x_0 < R$, where R is the radius of the lens.

We assume here that the angular distribution of the emission direction is uniform, so that the surface over which we must integrate is a portion of the unit sphere, of area element $\sin(\theta)d\theta d\varphi$.

We need to integrate the signal over the range of emission angles accepted by the lens. This range is defined by the intersection between the unit sphere and the detection cone. The apex of the cone is the emission point, and its circular base is the edge of the lens. If the lens is not centered, the cone becomes oblique.

Figure B.1 shows a side view of the unit sphere and the detection cone for a lens centered in x_0. The angles θ_+ and θ_- shown on this figure are defined by

$$\theta_\pm = \arctan\left(\frac{R \pm x_0}{h}\right). \tag{B.1}$$

We must integrate over the shaded region. For a symmetrically centered lens ($x_0 = 0$), this integral can be written as

$$Signal = \int_0^{\theta_{max}} \int_0^{2\pi} f(\theta)\sin(\theta)d\theta d\varphi = \int_0^{\theta_{max}} 2\pi f(\theta)\sin(\theta)d\theta, \tag{B.2}$$

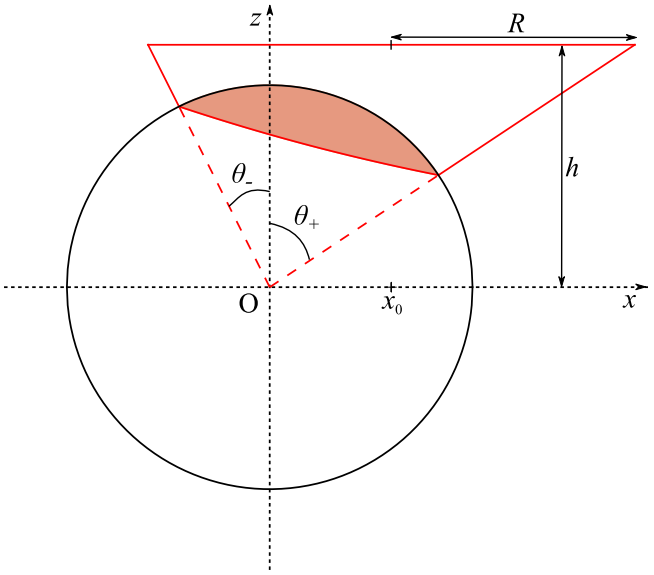

Figure B.1: Side view of the unit sphere and detection cone, in the case where the lens is centered in $x = x_0$. The shaded region shows the integration domain.

with $\theta_{max} = \arctan(R/h)$. We find an equation similar to eq. (3.59).

If the lens is not centered, the maximal angle θ_{max} increases with x_0 and is given by

$$\theta_{max}(x_0) = \theta_+ = \arctan\left(\frac{R + x_0}{h}\right). \tag{B.3}$$

Furthermore, for a given emission angle θ, the angle φ is restricted to the portion that is allowed by the intersection between the cone and the unit sphere. Two cases appear, depending on the value of θ.

- For $\theta < \theta_-$, the maximal φ angle, that will be called $\alpha(\theta)$, is simply equal to π.
- In the case where $\theta \in [\theta_-, \theta_+]$, $\alpha(\theta)$ can be calculated in the plane $z = h$ containing the lens, via a homothety. Figure B.2 shows the lens edge as a circle of radius R centered in $x = x_0$; O' is the point of coordinates $(0, 0, h)$. A photon emitted from the coordinate origin O at an angle θ from the z-axis would cross the plane $z = h$ along the circle of center O' and radius $r = h \tan\theta$. This circle (drawn in red on Fig. B.2) intersects the lens edge in two points M_1 and M_2. The angle $\alpha(\theta)$ is defined as the angle between O'M_1 and the x-axis.
  The coordinates of the point M_1 are

$$x_1 = \frac{x_0^2 + r^2 - R^2}{2x_0}, \quad y_1 = \sqrt{r^2 - x_1^2}, \quad z_1 = h \tag{B.4}$$

  We then have:

$$\alpha(\theta) = \arccos(x_1/r) = \arctan\left(\frac{x_0^2 + (h\tan\theta)^2 - R^2}{2x_0 h \tan\theta}\right). \tag{B.5}$$

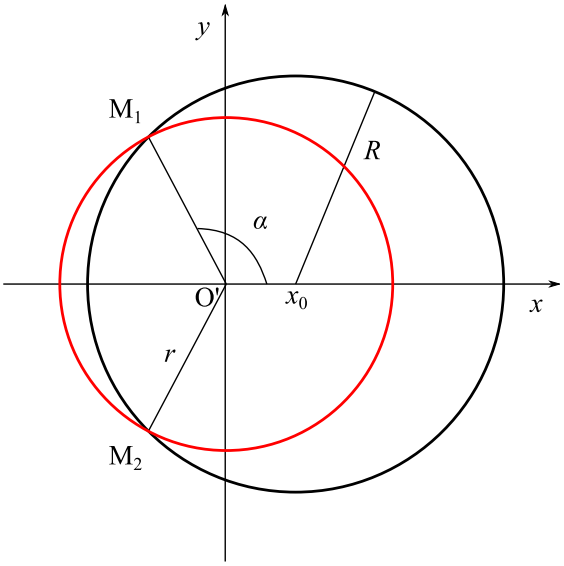

Figure B.2: The drawing is in the plane $z = h$. The black circle of radius R is the lens, centered in x_0. For a given angle θ between θ_- and θ_+, the red circle of center O' and radius $r = h \tan\theta$ intersects the lens edge in points M_1 and M_2.

Finally, for a given $x_0 < R$, the signal integrated over the angles accepted by the lens is

$$Signal(x_0) = \int_0^{\theta_{max}(x_0)} 2\alpha(\theta, x_0) \sin(\theta) f(\theta) d\theta \tag{B.6}$$

with

$$\theta_{max}(x_0) = \arctan\left(\frac{R + x_0}{h}\right) \tag{B.7}$$

$$\alpha(\theta, x_0) = \begin{cases} \pi & \text{if } \theta < \arctan\left(\frac{R-x_0}{h}\right) \\ \arctan\left(\frac{x_0^2 + (h\tan\theta)^2 - R^2}{2x_0 h \tan\theta}\right) & \text{else} \end{cases} \tag{B.8}$$

We can now check that for $x_0 = 0$, $\alpha(\theta, 0) = \pi$ for all values of θ and eq. (B.6) simplifies back to eq. (3.59).

Finally, we should integrate the function $Signal(x_0)$ along the detection region.

Appendix C

Least-squares method and uncertainties

We may start from the weighted linear least-squares fit in matrix notation, as explained in Appendix E of [Mohr2000]. This consists in solving $Y = AX$, with Y a vector containing N measurements, X the M parameters of the fit and A a $M \times N$ rectangular matrix, with $N > M$. Let us denote V the covariance matrix of the measurements Y. The fit consists in minimizing the sum of squares[1]

$$S = (Y - AX)^{\mathsf{T}} V^{-1} (Y - AX). \tag{C.1}$$

The solution for the parameters is given by

$$\hat{X} = G A^{\mathsf{T}} V^{-1} Y, \tag{C.2}$$

where $G = (A^{\mathsf{T}} V^{-1} A)^{-1}$ is the covariance matrix of the solution $\hat{X}$. The minimal value of S is

$$S_0 = (Y - A\hat{X})^{\mathsf{T}} V^{-1} (Y - A\hat{X}). \tag{C.3}$$

In section 4.2.2 of Chapter 4, I have written that the uncertainty on the fit parameters can be obtained from the size of the hypersurface (in M-dimensional space) defined by $S(X) = S_0 + 1$. Here, I would like to show that it can be easily understood in the weighted linear least-squares framework.

The idea is to develop S around its minimal value S_0,

$$\begin{aligned} S(\delta X) &= S_0 + (A\delta X)^{\mathsf{T}} V^{-1} (A\delta X) && \text{(C.4)} \\ &= S_0 + \delta X^{\mathsf{T}} (A^{\mathsf{T}} V^{-1} A) \delta X && \text{(C.5)} \\ &= S_0 + \delta X^{\mathsf{T}} G^{-1} \delta X && \text{(C.6)} \end{aligned}$$

[1] This corresponds to the chi-square χ^2 defined in Chapter 4.

where $\delta X = X - \hat{X}$.

I would like to show that the extremum of the hypersurface defined by

$$\delta X^{\mathsf{T}} G^{-1} \delta X = 1 \tag{C.7}$$

with respect to a given parameter (namely, the projection of the hypersurface on a given axis) yields the uncertainty on this parameter, that is the square root of the corresponding term of the matrix G.

Let us restrict this calculation to the simplified case of two parameters, which can be generalized easily. We can define

$$\delta X = \begin{bmatrix} x \\ y \end{bmatrix} \quad \text{and} \quad f(x,y) = \begin{bmatrix} x & y \end{bmatrix} G^{-1} \begin{bmatrix} x \\ y \end{bmatrix} \tag{C.8}$$

Equation (C.7) becomes

$$f(x,y) = 1 \tag{C.9}$$

In this two-dimensional case, it is the equation of an ellipse. If the two parameters x and y are correlated, the ellipse is tilted with respect to the axes. An illustration of this can be found in Fig. 4.2.

One should calculate the extremum with respect to x, that is, the value for which

$$\frac{\partial f}{\partial y} = 0 \tag{C.10}$$

This can be written as

$$\begin{bmatrix} 0 & 1 \end{bmatrix} G^{-1} \begin{bmatrix} x \\ y \end{bmatrix} + \begin{bmatrix} x & y \end{bmatrix} G^{-1} \begin{bmatrix} 0 \\ 1 \end{bmatrix} = 0 \tag{C.11}$$

The two terms on the left-hand side of the previous equation are equal to each other. One can combine eqs. (C.9) and (C.10) to write:

$$\begin{bmatrix} x & y \\ 0 & 1 \end{bmatrix} G^{-1} \begin{bmatrix} x \\ y \end{bmatrix} = \begin{bmatrix} 1 \\ 0 \end{bmatrix} \tag{C.12}$$

The inverse of the matrix on the left-hand side of this equation is given by

$$\begin{bmatrix} x & y \\ 0 & 1 \end{bmatrix}^{-1} = \begin{bmatrix} 1/x & -y/x \\ 0 & 1 \end{bmatrix}. \tag{C.13}$$

Multiplying both sides of eq. (C.12) by this inverse, then by the matrix G, one

obtains

$$\begin{bmatrix} x \\ y \end{bmatrix} = G \begin{bmatrix} 1/x & -y/x \\ 0 & 1 \end{bmatrix} \begin{bmatrix} 1 \\ 0 \end{bmatrix} = G \begin{bmatrix} 1/x \\ 0 \end{bmatrix} = \begin{bmatrix} G_{xx}/x \\ G_{xy}/x \end{bmatrix} \tag{C.14}$$

where $\begin{bmatrix} G_{xx} & G_{xy} \end{bmatrix}$ is the first row of the matrix G. Finally, the value of x at the extremum verifies

$$x = \sqrt{G_{xx}} \tag{C.15}$$

By definition, G_{xx} is the variance of parameter x. We have thus proven that the extremum of the hypersurface defined by $S(X) = S_0 + 1$ with respect to a given fit parameter gives the uncertainty on this parameter.

Résumé en français

Le travail présenté dans ce manuscrit a été réalisé entre 2014 et 2017 dans l'équipe « Métrologie des systèmes simples et tests fondamentaux » du Laboratoire Kastler Brossel, sous la direction de François Nez.

Contexte et principe de l'expérience

Les niveaux d'énergie de l'hydrogène

L'hydrogène est l'élément chimique le plus simple, composé d'un proton et d'un électron. Cela permet une bonne description théorique des niveaux d'énergie, qui dépendent de trois nombres quantiques n, L et J. Ces niveaux d'énergie peuvent s'écrire sous la forme d'une somme de deux termes :

$$E_{nLJ} = E_{nJ}^{DR} + L_{nLJ}. \tag{1}$$

Le premier terme a une expression exacte en fonction de la constante de Rydberg R_∞ et d'autres constantes fondamentales. Il prend en compte la solution de l'équation de Dirac, ainsi que l'effet de recul lié à la masse finie du noyau.

Le deuxième terme, appelé communément « déplacement de Lamb » ou « Lamb shift », lève la dégénérescence des niveaux de mêmes n, J et de L différent. Il inclut des contributions décrites par la théorie de l'électrodynamique quantique (QED), dont la plus importante est la self-énergie, suivie par la polarisation du vide, et d'autres termes d'ordres supérieurs dont le calcul peut s'avérer très complexe. Il contient également un effet dû à la taille finie du proton. En effet, le potentiel coulombien ressenti par l'électron est écranté à courte distance par la distribution de charge du proton, ce qui a pour effet de remonter l'énergie des niveaux S, pour lesquels la probabilité de présence de l'électron au niveau du noyau est plus forte.

A ces niveaux d'énergie s'ajoute une correction supplémentaire dite de structure hyperfine, décrivant le couplage du moment angulaire de l'électron avec le spin du noyau.

Spectroscopie haute résolution

Les différences entre niveaux d'énergie peuvent être mesurées expérimentalement très précisément grâce à la spectroscopie, la mesure de fréquences de transitions. L'électron peut passer d'un niveau d'énergie à un autre en émettant, ou absorbant, un photon dont l'énergie correspond à la différence entre celles des niveaux. Pour des raisons de symétrie, seules certaines transitions sont permises. Les états excités, qui peuvent se désexciter spontanément vers des niveaux de plus basse énergie, ont de ce fait des durées de vie très différentes. Un niveau d'énergie de durée de vie τ possède une largeur spectrale naturelle $\Gamma = 1/2\pi\tau$.

En pratique, les transitions sont souvent élargies, principalement par l'effet Doppler dû à l'agitation thermique des atomes. Pour repousser la limite de précision due à cet élargissement, plusieurs techniques de spectroscopie ont été développées. En particulier, la spectroscopie des transitions à deux photons, reliant des niveaux de même parité, permet de s'affranchir de l'effet Doppler du premier ordre par absorption simultanée de deux photons issus de deux faisceaux laser contra-propageants de même fréquence.

La spectroscopie à deux photons de l'hydrogène joue un rôle prépondérant dans la détermination de la constante de Rydberg par le CODATA[1], qui effectue tous les quatre ans un ajustement global des constantes fondamentales prenant en compte les dernières avancées expérimentales.

L'énigme du rayon du proton

A partir de l'ajustement du CODATA et des données expérimentales, on peut déduire une valeur du rayon de charge[2] du proton, en supposant que les calculs de QED sont exacts. Pour tester ces calculs, il faut disposer d'une détermination indépendante du rayon du proton. Une telle détermination peut être obtenue par des expériences de diffusion électron-proton. Cependant, l'analyse des données de ces expériences, très complexe, rend leur résultat peu précis.

Le rayon du proton peut également être déduit de la spectroscopie de l'hydrogène muonique, dans lequel l'électron est remplacé par un muon. Le muon étant 207 fois plus massif que l'électron, il est d'autant plus proche du noyau, et donc plus sensible à la taille de celui-ci. De ce fait, la contribution de l'effet de taille du noyau représente 1,8 % de l'écart $2S - 2P$ de l'hydrogène muonique, à comparer à une proportion de 0,014 % dans l'hydrogène électronique. Cette particularité rend possible une détermination très précise du rayon du proton, indépendante de la constante de Rydberg, sans nécessiter un effort aussi considérable sur la précision de la spectroscopie elle-même.

[1] Committee on Data for Science and Technology.

[2] Le rayon de charge est défini comme la racine du second moment de la distribution de charge du proton : $r_\mathrm{p} = \sqrt{\langle r^2 \rangle}$.

Une expérience dans ce but a été menée au Paul Scherrer Institute en Suisse, par une collaboration internationale incluant des membres de notre équipe. La fréquence de transition $2S-2P$ obtenue est étrangement en désaccord avec celle prédite par la théorie. Le rayon du proton déduit de cette expérience [Antognini2013], $r_\mathrm{p} = 0{,}84087(39)$ fm, est un ordre de grandeur plus précis, mais environ 4 % plus petit, que la valeur donnée par le dernier ajustement du CODATA [Mohr2016], $r_\mathrm{p} = 0{,}8751(61)$ fm.

Pour tenter de résoudre cette « énigme du rayon du proton », plusieurs expériences sont en cours. Notre expérience s'inscrit également dans cet effort.

Principe de notre expérience

La transition $1S - 3S$ à deux photons est excitée par un laser continu à 205 nm dans une cavité Fabry-Perot, sur un jet effusif d'atomes d'hydrogène à température ambiante. Elle est détectée par l'intermédiaire de la fluorescence Balmer-α ($3S - 2P$) à 656 nm. L'effet Doppler du premier ordre est compensé grâce à l'absorption de deux photons contra-propageants, mais il reste un effet du deuxième ordre, provoquant un déplacement de fréquence

$$\delta_\mathrm{Dop.2} \simeq -\frac{\nu_0 v^2}{2c^2}, \tag{2}$$

où ν_0 est la fréquence de résonance, v la vitesse atomique et c la vitesse de la lumière.

Une méthode originale permettant d'estimer la distribution de vitesse de notre jet atomique a été mise en place durant la thèse de Gaëtan Hagel [Hagel2001]. En appliquant un champ magnétique uniforme $\mathbf{B}$ perpendiculairement à la direction du jet atomique, les atomes de vitesse $\mathbf{v}$ perçoivent un champ électrique motionnel $\mathbf{E} = \mathbf{v} \times \mathbf{B}$ (figure 1). L'effet Stark quadratique dû à ce champ électrique déplace la fréquence de transition d'une quantité

$$\delta_\mathrm{Stark} \propto \frac{E^2}{\Delta_{SP}} = \frac{v^2 B^2}{\Delta_{SP}}, \tag{3}$$

où Δ_{SP} est l'écart en énergie du niveau $3S$ avec le plus proche niveau $3P$. Ce déplacement est proportionnel au carré de la vitesse atomique, comme l'effet Doppler du deuxième ordre. On pourrait penser que ces deux effets se compenseraient pour une valeur bien choisie du champ magnétique.

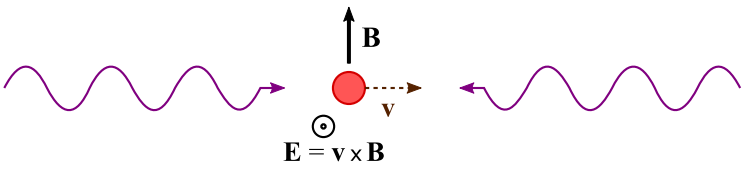

Figure 1 – Le champ magnétique $\mathbf{B}$ et le champ électrique motionnel $\mathbf{E}$.

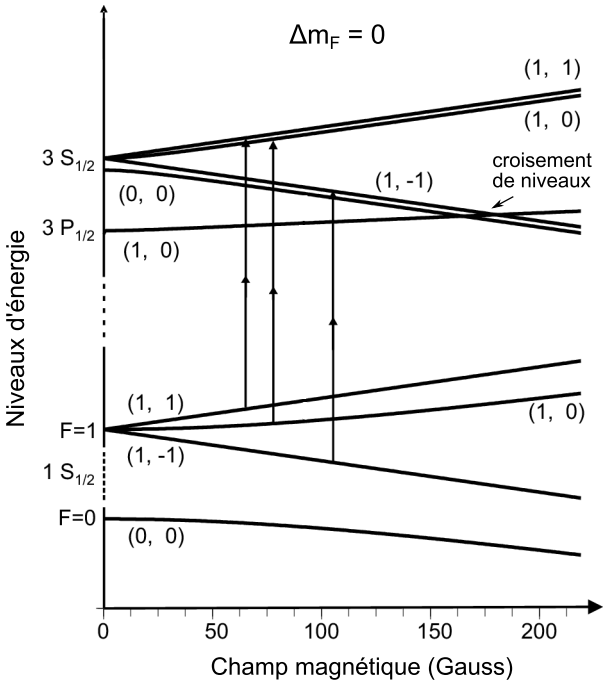

FIGURE 2 – Diagramme des niveaux déplacés par l'effet Zeeman. Les sous-niveaux $3S_{1/2}(F = 1, m_F = -1)$ et $3P_{1/2}(F = 1, m_F = 0)$ se croisent pour un champ magnétique d'environ 180 G.

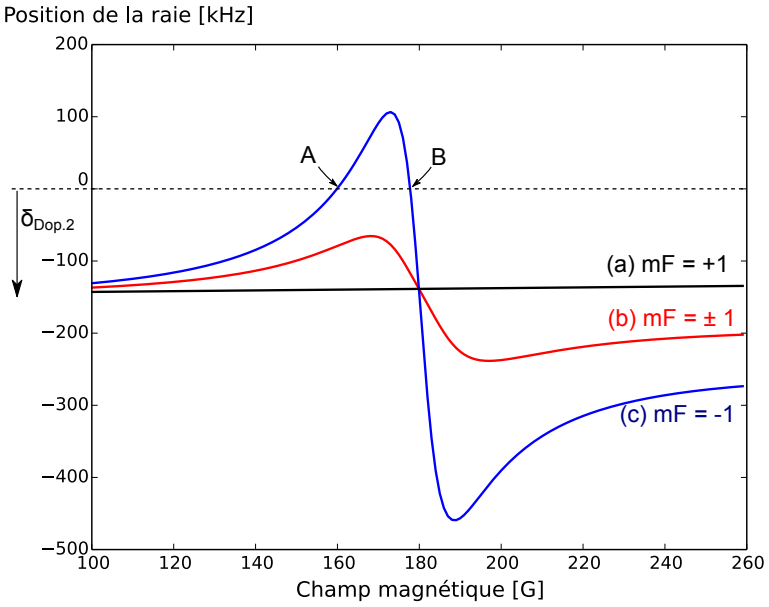

FIGURE 3 – Position théorique des raies $1S - 3S(F = 1, m_F = 1$ (a) et -1 (b)) en fonction du champ magnétique, calculées pour une vitesse atomique $v = 3$ km/s. La position apparente (b) résulte de la superposition des deux sous-transitions.

Cependant, le champ magnétique déplace lui-même tous les niveaux d'énergie par effet Zeeman, en levant la dégénérescence des sous-niveaux hyperfins, comme illustré sur la figure 2. De plus, pour la transition $1S-3S$ à deux photons, seules les transitions entre niveaux de même F et même m_F sont permises par les règles de sélection. Nous observons la transition entre les niveaux $F = 1$ car le niveau $1S_{1/2}(F = 1)$ est plus peuplé ; elle se sépare donc en trois sous-transitions. La fréquence de la transition entre les sous-niveaux $m_F = 0$ est très affectée par l'effet Zeeman ; elle est utilisée pour calibrer le champ magnétique. En revanche, les autres sous-transitions sont très peu déplacées par l'effet Zeeman. Pour un champ magnétique d'environ 180 G (18 mT), l'effet Zeeman cause un anticroisement entre les sous-niveaux $3S_{1/2}(F = 1, m_F = -1)$ et $3P_{1/2}(F = 1, m_F = 0)$. Par conséquent, l'effet Stark motionnel est grand pour la sous-transition $m_F = -1$ et compense l'effet Doppler pour deux valeurs du champ magnétique (points A et B sur la figure 3).

L'effet Doppler, et l'effet Stark pouvant le compenser, sont tous deux de l'ordre d'une centaine de kHz et bien inférieurs à la largeur naturelle du niveau $3S$ (1 MHz). Le signal observé résulte donc de la superposition des deux sous-transitions ($m_F = \pm 1$). Le déplacement de fréquence apparent est alors la moyenne des deux courbes précédentes, et la compensation de l'effet Doppler est seulement partielle. Il est donc nécessaire de mesurer la fréquence de transition pour différentes valeurs du champ magnétique appliqué, afin d'en déduire la distribution de vitesse grâce à un profil de raie théorique qui tient compte à la fois de l'effet Doppler et de l'effet Stark motionnel.

Historique récent

Ces dernières années, plusieurs améliorations ont marqué notre montage expérimental. Au cours de la thèse d'Olivier Arnoult, un dispositif de mesure de fréquence utilisant un peigne de fréquences a été mis en place, permettant une mesure de la fréquence de transition $1S - 3S$ avec une incertitude de 13 kHz, ou $4{,}4 \times 10^{-12}$ en valeur relative [Arnoult2010]. Sandrine Galtier a ensuite modifié la source laser d'excitation à 205 nm, remplaçant deux doublages successifs par une somme de fréquence, ce qui a permis un gain notable en intensité.

Grâce à cette nouvelle source laser, Sandrine Galtier a pu effectuer une nouvelle mesure de la fréquence $1S - 3S$, avec une incertitude statistique de 2,1 kHz [Galtier2014b]. Sa thèse s'est cependant terminée sur une interrogation quant à la valeur obtenue. En effet, un des effets systématiques entachant la mesure est un effet de déplacement de fréquence dû aux collisions subies par les atomes d'hydrogène. Pour estimer cet effet, la fréquence est mesurée pour différentes valeurs de la pression dans le jet atomique, afin d'effectuer une extrapolation à pression nulle. Le protocole de détermination de la vitesse atomique, utilisant le champ magnétique, n'avait été réalisé

que pour une seule valeur de pression. Or, le modèle de distribution de vitesse utilisé lors de l'analyse peut inclure une dépendance en pression. Suivant si l'on supposait, ou non, une telle dépendance en pression, la fréquence de transition obtenue par Sandrine Galtier variait d'une dizaine de kHz ! Il apparaissait donc indispensable d'estimer la distribution de vitesse pour différentes valeurs de la pression afin de s'assurer de sa dépendance (ou non) en pression. Cela a été réalisé au cours de mon doctorat et est présenté dans ce manuscrit.

Le montage expérimental $1S$–$3S$

Le laser d'excitation à 205 nm

La radiation à 205 nm nécessaire à l'excitation est produite par somme de fréquences, d'un laser titane-saphir à 894 nm et d'une radiation à 266 nm produite par le doublage en fréquence d'un laser Verdi à 532 nm. Tous ces lasers fonctionnent en mode continu.

Le laser titane-saphir (Ti:Sa) est un laser « fait-maison » construit selon un modèle proposé par François Biraben. Sa cavité en anneau comporte plusieurs éléments sélectifs qui lui confèrent une grande accordabilité. Dans sa configuration actuelle, il délivre environ 1,6 W à 894 nm. Le doublage en fréquence d'un laser Nd:YVO_4 commercial (Verdi V6 et cavité de doublage MBD266, Coherent) produit environ 250 mW à 266 nm.

La somme de fréquences est réalisée dans un cristal de bêta-borate de baryum (BBO) à l'aide de deux cavités imbriquées dont les chemins optiques se recouvrent dans le cristal. La géométrie de la cavité de doublage, qui a été construite par Sandrine Galtier durant sa thèse, est présentée dans la figure 2.3. Elle permet d'obtenir jour à jour environ 10 mW de radiation continue à 205 nm.

Les deux lasers, Ti:Sa et Verdi, sont stabilisés en fréquence à l'aide de plusieurs asservissements utilisant des cavités Fabry-Perot. Par l'intermédiaire d'un modulateur acousto-optique (AOM), la fréquence du laser Ti:Sa peut être ajustée finement tout en restant stabilisée. Un laser étalon, dont la fréquence est asservie sur une transition à deux photons du rubidium, fournit la stabilité long-terme.

Mesures de fréquences

Les fréquences de ces différents lasers sont mesurées grâce à un peigne de fréquences femtoseconde, qui est un laser en impulsions à modes bloqués en phase, émettant une suite cohérente d'impulsions courtes. Le spectre d'un tel laser est composé de nombreux modes régulièrement espacés, formant une sorte de « règle graduée » optique permettant de déterminer avec précision la fréquence de nos lasers continus.

Pour mesurer la fréquence d'un laser continu f_{cw}, nous réalisons le battement entre ce laser et la « dent » du peigne la plus proche, de fréquence $f_n = nf_{\mathrm{rep}} \pm f_0$. Le taux de répétition f_{rep} et la fréquence d'offset f_0 qui caractérisent le spectre du peigne sont tous deux stabilisés et référencés grâce à un lien par fibre optique avec l'horloge à césium du SYRTE.

La fréquence du laser Ti:Sa, ainsi que celle du laser étalon, sont mesurées de cette façon. En revanche, pour pallier une insuffisance de puissance dans la partie verte du spectre de notre peigne, nous avons modifié le dispositif permettant d'obtenir la fréquence du laser Verdi. Après maints essais infructueux, la solution finalement choisie nécessite un laser supplémentaire permettant de transférer la mesure de fréquence dans le domaine infrarouge. Ce laser Nd:YAG continu possède deux sorties : l'une à 1064 nm, avec laquelle nous réalisons un battement avec le peigne de fréquences ; l'autre, doublée à 532 nm, pouvant être comparée directement au laser Verdi.

Le jet atomique et la cavité d'excitation

Les atomes d'hydrogène sont produits par dissociation de molécules de dihydrogène dans une décharge radiofréquence. Ils sont ensuite conduits à travers une buse en Téflon vers la cavité de détection, qui est mise sous vide par l'intermédiaire d'une pompe à diffusion d'huile, elle-même pompée par une pompe primaire à palettes. Le jet effusif formé par les atomes est colinéaire avec la cavité Fabry-Perot à 205 nm qui permet l'excitation à deux photons. Cette cavité est placée en configuration quasi-concentrique pour maximiser l'intensité lumineuse au niveau du col du faisceau. L'un des miroirs est monté sur une cale piézoélectrique afin de maintenir sa longueur à résonance avec la radiation à 205 nm par l'intermédiaire d'une détection synchrone.

La mesure de l'intensité lumineuse intra-cavité, nécessaire à l'évaluation expérimentale du déplacement lumineux, n'est pas aisée. D'une part, l'alignement optique de la cavité est peu stable. D'autre part, le rayonnement ultraviolet dégrade les couches réfléchissantes des miroirs, ainsi que la photodiode placée en sortie de la cavité. Dans une tentative d'amélioration de la mesure d'intensité transmise, nous avons modifié cette photodiode en tirant partie d'une propriété de la fluorescéine : celle-ci, placée en solution aqueuse dans un petit tube de verre, absorbe l'UV et réémet des photons verts, recueillis par une photodiode placée sur le côté du tube. Malgré tout, la mesure d'intensité lumineuse demeure difficile et peu reproductible à long terme.

La fluorescence à 656 nm résultant de la désexcitation des atomes vers le niveau $2P$ est recueillie par un système de détection composé d'un condenseur situé au dessus de la zone d'excitation (au centre de la cavité Fabry-Perot), et d'un miroir sphérique placé en dessous de cette zone. Les photons sont ensuite conduits vers un photomultiplicateur à travers un filtre interférentiel à 656 nm et un jeu de lentilles.

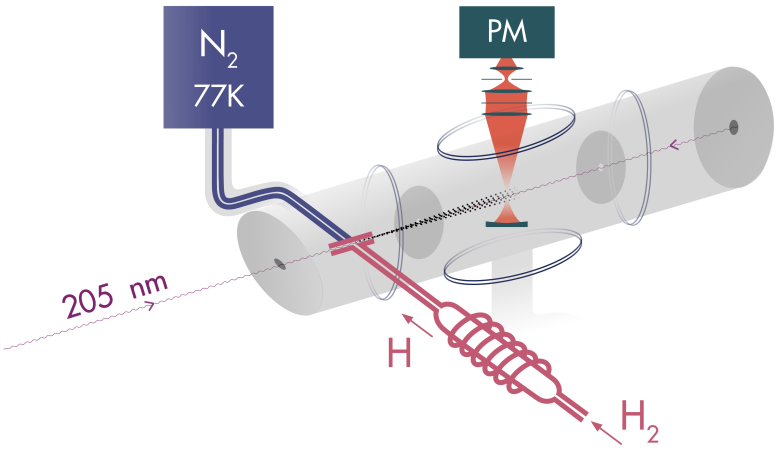

FIGURE 4 – Vue schématique de la cavité d'excitation.

A la toute fin de ma thèse, nous avons mis en place un système permettant de refroidir les atomes à la température de l'azote liquide (77 K), par thermalisation avec une buse en aluminium reliée à un réservoir d'azote liquide. Cela permettra de réduire leur vitesse, et donc l'effet Doppler du deuxième ordre. Toutes les mesures présentées dans ce manuscrit ont été réalisées à température ambiante.

Deux bobines de Helmholtz, dans lesquelles peut circuler un courant d'une centaine d'ampères, permettent de créer le champ magnétique vertical nécessaire à l'évaluation de la distribution des vitesses atomiques. Ce champ magnétique est calibré en mesurant la fréquence de la transition $1S_{1/2} \rightarrow 3S_{1/2}(F = 1, m_F = 0)$, qui est fortement déplacée par l'effet Zeeman.

Signaux observés

L'acquisition des données est contrôlée par un programme informatique écrit en langage Python. Durant un enregistrement, la fréquence d'excitation est modifiée, par l'intermédiaire du modulateur acousto-optique (AOM), en suivant une séquence prédéfinie d'allers-retours pour éviter d'éventuelles dérives. Pour chaque point de mesure durant une seconde, l'ordinateur enregistre la fréquence des différents battements, ainsi que le nombre de photons de fluorescence, et l'intensité lumineuse transmise par la cavité. D'autres paramètres, tels que la puissance lumineuse à l'entrée de la cavité d'excitation, la pression dans cette cavité, et le courant circulant dans les bobines de Helmholtz, sont recueillis à la main. Un exemple de signal de transition est représenté sur la figure 5.

J'ai également eu l'occasion d'observer pour la première fois la transition $1S-3S$ du deutérium (voir figure 2.18 p. 46), située à environ 800 GHz de celle dans l'hydrogène.

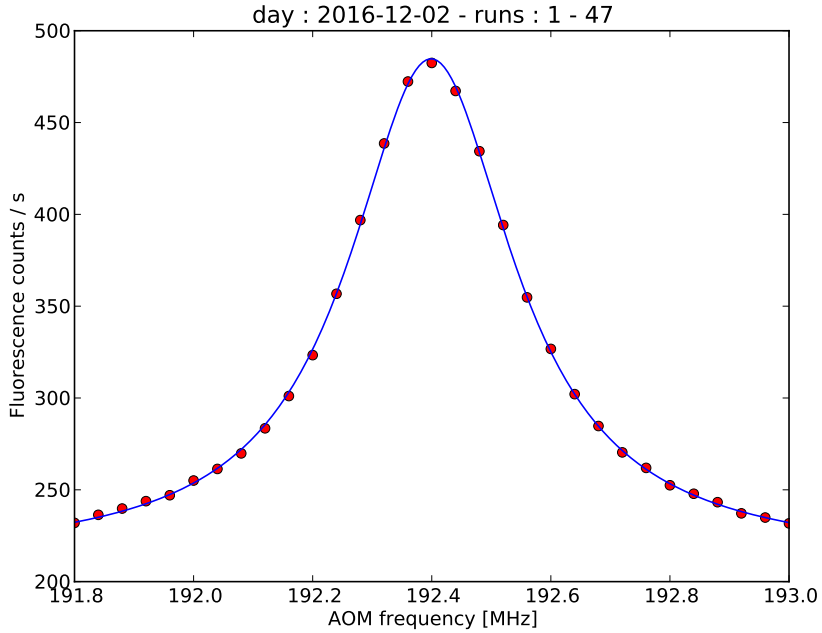

FIGURE 5 – Exemple de signal de la transition $1S - 3S$ de l'hydrogène, obtenu en 4 heures d'intégration, à champ magnétique nul. Le nombre de photons de fluorescence par seconde est indiqué en fonction de la fréquence du modulateur acousto-optique (AOM) servant à modifier la fréquence d'excitation. L'abscisse doit être multipliée par 4, et renversée, pour obtenir une échelle relative en fréquence atomique. Les points sont les données expérimentales, la courbe est un ajustement lorenztien. La largeur de raie observée vaut environ 1,35 MHz, à comparer à une largeur naturelle de 1 MHz.

Les effets systématiques

Le signal enregistré est ajusté par une forme de raie théorique qui tient compte à la fois de l'effet Doppler du deuxième ordre, et de l'effet Stark motionnel pouvant le compenser en partie. D'autres effets pouvant déplacer la raie sont également considérés.

Calcul de la forme de raie théorique

Le signal de fluorescence résulte de la désexcitation du niveau $3S$, et du niveau $3P$ qui lui est couplé par l'effet Stark. Dans un premier temps, la population de ces niveaux est calculée en utilisant le formalisme de la matrice densité. Il s'agit de résoudre l'équation d'évolution de la matrice densité ρ,

$$\frac{\mathrm{d}\rho}{\mathrm{d}t} = \frac{1}{i\hbar}\left[(H + H_L + H_{Stark}), \rho\right] + \left\{\frac{\mathrm{d}\rho}{\mathrm{d}t}\right\}_{s.e.}, \tag{4}$$

où H est le hamiltonien d'un atome d'hydrogène immobile placé dans un champ magnétique uniforme, H_L décrit l'interaction atome-lumière, et H_{Stark} est la perturbation due au champ électrique motionnel. Le dernier terme représente la relaxation

par émission spontanée. La fluorescence théorique est obtenue en multipliant chaque population par le rapport de branchement correspondant [Arnoult2010].

Le modèle de distribution de vitesse utilisé dans le calcul de forme de raie a été raffiné au cours de la thèse de Sandrine Galtier. S'appuyant sur la distribution de vitesse « maxwellienne » d'un jet effusif, il tient compte d'une déplétion des atomes lents. La distribution de vitesse dépend alors de deux paramètres σ et v_0, et est de la forme

$$f(v, \sigma, v_0) \propto v^3 \exp\left(-\frac{v^2}{2\sigma^2}\right) P[v/\sigma] \exp(-v_0/v). \tag{5}$$

La fluorescence calculée précédemment est donc intégrée sur cette distribution de vitesse. Le profil de raie est ensuite convolué avec une fonction lorentzienne de largeur Γ afin de simuler un élargissement. La fonction utilisée pour l'ajustement des données contient des paramètres supplémentaires d'amplitude (A) et d'offset (C), et s'écrit

$$F_{B,\sigma,v_0}(\nu_c, \Gamma, A, C; \nu) = A \times (S_{B,\sigma,v_0} * f_{\mathrm{Lor}})(\nu - \nu_c, \Gamma) + C. \tag{6}$$

Effets de déplacement de la fréquence

Dans notre expérience, outre l'effet Doppler déjà pris en compte dans le modèle de forme de raie, deux effets sont susceptibles de déplacer la fréquence de transition de plusieurs kHz : le déplacement lumineux et le déplacement collisionnel. Ils nécessitent tous deux une étude expérimentale importante. L'effet d'interférence quantique, qui est petit dans notre cas, a fait l'objet d'une étude théorique approfondie.

Déplacement lumineux Cet effet est dû à un couplage entre les photons d'excitation et les états d'énergie électroniques. Un champ électromagnétique a deux effets sur ces niveaux d'énergie : à résonance, il induit des transitions ; hors résonance (ou dans le cas d'une transition à deux photons), il déplace les niveaux proportionnellement à l'intensité lumineuse reçue par les atomes. Dans notre cas, une estimation théorique donne un décalage en fréquence positif de l'ordre de 12 kHz. Il était donc important d'évaluer cet effet expérimentalement.

Déplacement collisionnel Les collisions subies par les atomes d'hydrogène peuvent aussi induire un déplacement de la fréquence de transition, proportionnellement à la pression dans le jet atomique. Durant la thèse de Sandrine Galtier, une interrogation était apparue quant au signe de cet effet, suivant l'existence, ou non, d'une dépendance en pression de la distribution de vitesse. L'étude expérimentale menée durant ma thèse a permis de montrer que le déplacement collisionnel est négatif. Ce signe est en accord avec une modélisation réalisée par A. Matveev, simulant les collisions par un potentiel attractif de Van der Waals [Matveev2017, Yost2016].

Interférence quantique Il est également utile d'estimer l'effet d'interférence quantique, plus connu sous le nom de *cross-damping*, qui peut intervenir lorsqu'une transition atomique induite optiquement est détectée via la fluorescence induite. Cet effet est dû à la présence de niveaux atomiques non résonants, mais proches du niveau excité. Comme la fluorescence est détectée de manière non sélective, une interférence est possible entre les différents chemins radiatifs ($1S-3S-2P$ et $1S-3D-2P$) partageant les mêmes niveaux initial et final. Le signal observé devient le carré d'une somme d'amplitudes, au lieu d'être une simple somme d'intensités :

$$\text{Signal} = \left|\sum_{\mathrm{i}} \mathrm{A_i}\right|^2 = \sum_{\mathrm{i}} |\mathrm{A_i}|^2 + \sum_{\substack{i,j \\ i\neq j}} \mathrm{A_i A_j^*}. \tag{7}$$

Il contient alors des termes croisés, dont la forme en dispersion induit une asymétrie de la forme de raie et un déplacement de la fréquence apparente de la transition, cet effet n'étant pas pris en compte dans le modèle utilisé pour calculer la forme de raie théorique.

En m'inspirant des travaux de P. Amaro *et al.*, effectués dans le cadre de la spectroscopie des atomes muoniques [Amaro2015], j'ai estimé théoriquement le déplacement de la fréquence $1S-3S$ dans notre expérience [Fleurbaey2017]. Ici, l'effet d'interférence est dû à la présence des niveaux $3D$, à quelques gigahertz du niveau $3S$. La méthode de calcul est basée sur une analogie avec une diffusion de type Raman-Stokes. Dans notre cas, l'excitation se fait à deux photons, ce qui implique la présence d'un opérateur tensoriel, de rang 0 ou 2 suivant la transition étudiée, remplaçant l'opérateur dipolaire électrique habituel. L'étude théorique a été effectuée pour l'hydrogène et le deutérium, dont les niveaux d'énergie diffèrent uniquement par la structure hyperfine. Le décalage en fréquence est cependant approximativement le même pour les deux isotopes, car la structure hyperfine du niveau $3D$ est négligeable devant la largeur naturelle de ce niveau (environ 10 MHz).

Cet effet d'interférence disparaît si la fluorescence est détectée dans toutes les directions. Dans le cas d'un détecteur ponctuel, l'amplitude des termes croisés (et donc le déplacement de fréquence résultant) dépend simplement de l'angle entre la polarisation des photons d'excitation et la direction de détection.

Pour la transition $1S-3S$, le déplacement en fréquence maximal dans le cas d'un détecteur ponctuel serait d'environ $-0{,}9$ kHz. En prenant en compte l'étendue spatiale de notre détecteur, le déplacement prédit pour la fréquence atomique devient environ $-0{,}58$ kHz, ce qui est inférieur à notre incertitude expérimentale actuelle. Cette étude sera néanmoins prise en compte dans le résultat final, en ajoutant une correction de $+0{,}6(2)$ kHz à la fréquence obtenue.

Causes d'élargissement

La largeur du signal observé (figure 5) est supérieure à la largeur naturelle du niveau $3S$. Bien que cette largeur ne soit pas un élément primordial pour notre mesure, il est utile de comprendre l'origine de l'élargissement observé.

Plusieurs causes d'élargissement ont été considérées. Le temps de transit des atomes à travers le faisceau laser semble être la cause prépondérante d'élargissement. Les collisions peuvent également jouer un rôle, tandis que l'élargissement par saturation est négligeable dans notre cas. La largeur spectrale du laser d'excitation ne limite pas à l'heure actuelle la largeur de la transition observée. Elle peut en revanche avoir une grande incidence sur celle-ci, comme nous en avons fait l'expérience fortuite lors d'un problème affectant la stabilisation en fréquence du laser Verdi.

Analyse des données

Entre septembre 2016 et février 2017, nous avons enregistré environ 1700 signaux de la transition $1S_{1/2}^{F=1} - 3S_{1/2}^{F=1}$, en suivant le protocole décrit page 114. Ces mesures ont été effectuées pour deux valeurs de la pression, évaluées à $2{,}7 \times 10^{-5}$ mbar (basse pression) et 2×10^{-4} mbar (haute pression). Cette pression n'est connue que de manière relative, la jauge à ionisation étant placée sur le côté de la chambre à vide et non pas au niveau du jet atomique. Pour l'analyse, nous avons séparé ces enregistrements en trois séries de données, deux séries à basse pression (BP1 et BP2) encadrant une série à haute pression (HP). Pour chaque valeur de la pression, nous avons fait varier le champ magnétique B appliqué aux atomes, observant la transition à champ magnétique nul et pour différentes valeurs de B autour de l'anticroisement à 180 G, là où l'effet Stark motionnel est important.

Chaque enregistrement (« run ») est composé de 10 scans de N points de mesure (avec $N = 31$ ou 51, correspondant à une largeur de balayage en fréquence atomique de 1,2 ou 2 MHz). Pour chacun de ces points, la fréquence atomique est déduite des différentes fréquences de battements ainsi que de la fréquence de l'AOM, qui est modifiée au cours d'un scan suivant une séquence prédéfinie.

Un filtre est alors appliqué aux données afin de supprimer les points erronés. Ceux-ci peuvent avoir différentes causes. La fréquence est parfois mal comptée, si une boucle d'asservissement décroche par exemple. On vérifie donc que chaque fréquence de battement est comprise dans un intervalle prédéfini. Le nombre de photons de fluorescence peut également chuter de manière anormale, principalement lorsque la cavité de détection, qui est sensible aux vibrations, se désasservit. Le comptage de photons, ainsi que l'intensité d'UV transmise par la cavité, sont tous deux comparés à des seuils définis pour chaque run.

Enfin, un « signal » est obtenu par la moyenne des 10 scans, pour les N points du balayage en fréquence.

Dans un premier temps, chaque signal est ajusté séparément par le profil théorique de forme de raie $F_{B,\sigma,v_0}(\nu_c, \Gamma, A, C; \nu)$ défini dans l'équation (6). Quatre paramètres sont ajustés : fréquence centrale ν_c, élargissement Γ, amplitude A et offset C. L'ajustement est réalisé par la routine *optimize.leastsq* en langage Python, basée sur la méthode des moindres carrés, qui consiste à minimiser la quantité

$$S = \sum_{i=1}^{N} [Y_i - F_{B,\sigma,v_0}(\nu_c, \Gamma, A, C; X_i)]^2, \tag{8}$$

où X_i sont les N points de fréquence, et Y_i la fluorescence mesurée pour chaque point.

L'incertitude sur la fréquence centrale optimale est déduite de la matrice de covariance créée par la routine Python.

Distribution de vitesse

Il faut alors déterminer les paramètres σ et v_0 de la distribution de vitesse, séparément pour les différentes valeurs de la pression. L'ajustement décrit ci-dessus est réalisé pour une grille de valeurs des paramètres (σ, v_0). Pour chaque série de données (BP1, BP2, HP), on calcule la moyenne pondérée de la fréquence centrale, sans distinction de champ magnétique,

$$\nu_{\text{mean}} = \frac{\sum_{i=1}^{k} (\nu_i/\sigma_i^2)}{\sum_{i=1}^{k} (1/\sigma_i^2)}, \tag{9}$$

ainsi que la quantité

$$\chi^2 = \sum_{i=1}^{k} \left[\frac{(\nu_i - \nu_{\text{mean}})^2}{\sigma_i^2} \right]. \tag{10}$$

La surface $\chi^2(\sigma, v_0)$ est ajustée par un polynôme du second degré en σ et du troisième degré en v_0. Le minimum de cette surface donne les valeurs optimales des paramètres. Il est alors possible de calculer la fréquence correspondante ν_{opt}, soit en ajustant la surface de fréquence par un polynôme similaire, soit en ajustant à nouveau tous les signaux pour les paramètres optimaux de la distribution de vitesse (ces deux manières sont compatibles).

La méthode utilisée pour calculer les incertitudes s'appuie sur le fait que, en l'absence de corrélations, l'incertitude sur un paramètre d'ajustement est donnée par la valeur de ce paramètre pour laquelle χ^2 est augmenté de 1 par rapport à sa valeur optimale χ^2_{opt}. Ici, les paramètres σ et v_0 étant corrélés, l'incertitude est calculée simultanément pour les deux paramètres.

Dans le plan (σ, v_0), nous traçons la courbe d'équation

$$\chi^2(\sigma, v_0) = \chi^2_{\text{opt}} + 1, \tag{11}$$

qui ressemble à une ellipse. Les incertitudes sont alors données par la projection de cette courbe sur les axes (voir figure 4.2 p. 81). A ce stade, nous calculons le rapport de Birge, défini par $R_B = \sqrt{\chi^2_{\text{opt}}/(k-2)}$, où k est le nombre de runs. Nous multiplions les incertitudes par ce rapport s'il est plus grand que 1, afin de tenir compte de la dispersion des points expérimentaux. L'incertitude sur la fréquence s'obtient facilement en calculant l'écart maximal entre les fréquences correspondant à la courbe d'équation (11) et la fréquence optimale (figure 4.3).

Correction des effets systématiques

Dans un premier temps, il faut corriger du déplacement lumineux les fréquences obtenues ci-dessus. La correction sera basée sur un paramètre mesurable qui reflète l'intensité lumineuse vue par les atomes. Or, nous avons potentiellement accès à deux tels paramètres : l'intensité lumineuse transmise par la cavité, et la hauteur du profil de fluorescence observé. Cette dernière, exprimée en photons/s, est proportionnelle au carré de l'intensité lumineuse absorbée par les atomes. Cette hauteur doit être corrigée de sa variation théorique avec le champ magnétique appliqué aux atomes, et est également dépendante de la pression. A première vue, le paramètre le plus naturel à utiliser paraît être l'intensité transmise. Cependant, la mesure de cette intensité n'était pas reproductible au delà de quelques jours ; il semblerait qu'elle dépende de l'alignement de la cavité d'excitation. Nous avons donc décidé d'utiliser la hauteur du signal comme indicateur de l'intensité lumineuse reçue par les atomes.

Dans le but de caractériser le déplacement lumineux, nous avons réalisé des enregistrements (inclus dans la série BP2) en faisant varier manuellement l'intensité lumineuse, à basse pression. La pente d'un ajustement linéaire de la fréquence en fonction de la racine de la hauteur du signal (figure 4.5), donne un coefficient de correction ($\xi_{\text{BP}} = 595 \pm 172$ Hz$/\sqrt{\text{photons/s}}$) qui est alors appliqué à tous les signaux enregistrés à basse pression. A haute pression, ce coefficient n'a aucune raison d'être valide, puisque la hauteur du signal peut dépendre de la pression. Le coefficient de correction est obtenu en minimisant le χ^2 de cette série, ce qui revient à faire une extrapolation utilisant l'intégralité des signaux. L'intensité lumineuse d'excitation ayant peu varié lors des enregistrements à haute pression, ce coefficient est peu précis.

Finalement, les valeurs de fréquence, avant et après correction du déplacement lumineux, ainsi que les paramètres de la distribution de vitesse, sont résumées dans la table 1.

Série	ν_{opt}	δ_{LS}	ν_{corr}	σ	v_0
BP1	734,2(3,9)	−10,4(3,0)	723,8(4,9)	1,515(52)	1,23(55)
BP2	730,3(2,4)	−12,1(3,5)	718,2(4,3)	1,495(32)	1,33(31)
HP	713,2(7,1)	−6,3(10,2)	706,9(12,4)	1,521(85)	0,87(78)

TABLE 1 – La fréquence non corrigée, la correction du déplacement lumineux, et la fréquence corrigée, exprimées en kHz. Seuls les quatre derniers chiffres de la fréquence sont donnés : $\nu = 2\,922\,742\,936\,\text{xxx,x}$ kHz. L'incertitude sur la fréquence corrigée est la somme en quadrature des deux autres incertitudes. Le tableau donne également les paramètres de la distribution de vitesse obtenus par l'ajustement, en km/s.

Il est alors possible d'effectuer une extrapolation en fonction de la pression afin de déterminer la fréquence corrigée du déplacement collisionnel (figure 4.6). Pour réaliser l'extrapolation, une corrélation a été prise en compte entre les deux séries de données à basse pression, pour traduire le fait que la correction de déplacement lumineux a été déterminée avec le même coefficient pour ces deux séries. La fréquence à pression nulle vaut ainsi

$$\nu = 2\,922\,742\,936\,722{,}3(4{,}9)\ \text{kHz}. \tag{12}$$

Comme indiqué plus haut, il faut maintenant ajouter une correction de +0,6(2) kHz pour prendre en compte l'effet d'interférence quantique. Nous pouvons enfin utiliser les écarts hyperfins pour obtenir la fréquence centroïde de la transition $1S-3S$,

$$\begin{aligned} &\nu_{1S-3S}^{\text{centroïde}} = \nu_{1S-3S}^{F=1} + \frac{1}{4}\Delta E_{\text{HFS}}(1S) - \frac{1}{4}\Delta E_{\text{HFS}}(3S), \\ &\text{avec} \left| \begin{array}{l} \Delta E_{\text{HFS}}(1S) = 1\,420\,405{,}752\ \text{kHz}, \\ \Delta E_{\text{HFS}}(3S) = 52\,609{,}44(1)\ \text{kHz}. \end{array} \right. \end{aligned} \tag{13}$$

Conclusion

Finalement, la fréquence de la transition $1S-3S$ obtenue vaut

$$\nu_{1S-3S} = 2\,922\,743\,278\,672{,}0(4{,}9)\ \text{kHz}. \tag{14}$$

L'incertitude de 4,9 kHz correspond à une incertitude relative de $1{,}7 \times 10^{-12}$.

Par combinaison linéaire avec la fréquence de transition $1S-2S$, mesurée avec une très grande précision [PARTHEY2011], on peut déduire de notre résultat une valeur de la constante de Rydberg,

$$R_\infty = 10\,973\,731{,}568\,55(26)\ \text{m}^{-1}, \tag{15}$$

et du rayon du proton,

$$r_p = 0{,}879(25)\ \text{fm}. \tag{16}$$

Ces valeurs sont en bon accord avec les valeurs recommandées par le CODATA [Mohr2016].

Par ailleurs, on remarque que la distribution de vitesse estimée semble peu dépendre de la pression. A la lumière de ce résultat, nous avons pu réanalyser les données recueillies pendant la thèse de Sandrine Galtier [Galtier2014a]. Le résultat de cette nouvelle analyse, réalisée par François Biraben,

$$\nu_{1S-3S} = 2\,922\,743\,278\,672{,}2(2{,}8)\ \text{kHz}, \tag{17}$$

est en très bon accord avec celui obtenu durant ma thèse, malgré plusieurs différences entre les jeux de données. En effet, durant les trois ans séparant les deux sessions d'enregistrement, plusieurs changements sont survenus dans le montage expérimental. La fréquence du laser à 532 nm est maintenant mesurée par l'intermédiaire d'un laser auxiliaire à 1064 nm. La jauge mesurant la pression a été remplacée, empêchant une comparaison directe du déplacement collisionnel. Enfin, la puissance lumineuse ressentie par les atomes était également estimée différemment.

Ces deux résultats sont en accord avec la valeur prédite par le CODATA, renforçant ainsi l'énigme du rayon du proton.

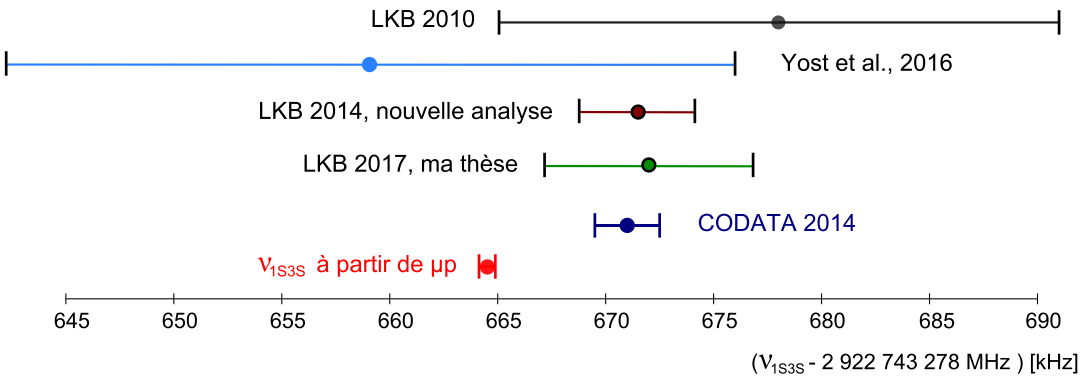

Figure 6 – Comparaison de notre mesure (LKB 2017) avec d'autres déterminations de la fréquence de transition $1S-3S$ de l'hydrogène.

La figure 6 présente une comparaison de notre mesure (LKB 2017) avec d'autres déterminations expérimentales de la fréquence de transition $1S-3S$: la dernière mesure publiée par l'équipe (LKB 2010, [Arnoult2010]), les données de Sandrine Galtier réanalysées (LKB 2014), et la mesure publiée récemment par le groupe de Garching où la transition est excitée par un peigne de fréquence picoseconde [Yost2016]. Deux déterminations théoriques de cette fréquence sont également représentées, obtenues en utilisant soit les valeurs recommandées par le CODATA, soit le rayon du proton et la constante de Rydberg déduites de la spectroscopie de l'hydrogène muonique.

Perpectives

Dans les prochains mois, une nouvelle mesure de la fréquence de transition $1S-3S$ sera effectuée, cette fois avec les atomes refroidis à une température proche de celle de l'azote liquide grâce au système de refroidissement mentionné page 114. En théorie, cela réduira l'effet Doppler du deuxième ordre d'un facteur 4, rendant notre mesure moins sensible à la détermination de la distribution de vitesse. Le système de refroidissement a été installé durant les derniers mois de mon doctorat, et nous avons pu observer la transition pour la première fois avec des atomes refroidis à la toute fin du mois de juillet 2017. La figure 4.8 (page 95) présente ainsi une moyenne de 19 runs, enregistrés pour une température autour de 120 K. La mesure de fréquence était seulement relative, le peigne de fréquence étant éteint. Par ailleurs, le cristal de BBO utilisé pour la somme de fréquence était vieux et peu efficace, délivrant moins de 4 mW à 205 nm. En comparant ce signal à d'autres enregistrements réalisés le même jour, mais à température ambiante, nous avons néanmoins pu observer le décalage en fréquence (de l'ordre d'une centaine de kHz) dû à la variation de la vitesse atomique. Plusieurs problèmes techniques doivent encore être surmontés avant de pouvoir commencer une série d'enregistrements. La métrologie $1S-3S$ de l'hydrogène refroidi sera effectuée par Simon Thomas durant sa thèse.

La transition $1S-3S$ pourra également être étudiée dans le deutérium. En effet, la fréquence de la source laser d'excitation peut être modifiée simplement pour atteindre cette transition. Durant ma thèse, la transition $1S-3S$ du deutérium a été observée pour la première fois avec un laser continu.

A plus long terme, la source UV pourra être modifiée pour atteindre la transition à deux photons $1S-4S$ à 194 nm, dans l'hydrogène ou le deutérium. Un avantage de cette transition, qui n'a jamais été observée, est sa largeur naturelle de 700 kHz, plus faible que celle de la transition $1S-3S$ (1 MHz). De plus, une petite partie des atomes excités retomberont par cascade radiative sur le niveau métastable $2S$, à partir duquel il serait possible d'effectuer une transition à un photon pour déterminer la distribution de vitesse. Cela permettrait de tester notre méthode actuelle de détermination de cette distribution.

Bibliography

[Amaro2015] P. Amaro, B. Franke, J. J. Krauth, M. Diepold, F. Fratini, L. Safari, J. Machado, A. Antognini, F. Kottmann, P. Indelicato, R. Pohl, and J. P. Santos. *Quantum interference effects in laser spectroscopy of muonic hydrogen, deuterium, and helium-3.* Phys. Rev. A **92** (2015) 022514.

[Antognini2013] A. Antognini, F. Nez, K. Schuhmann, F. D. Amaro, F. Biraben, J. M. R. Cardoso, D. S. Covita, A. Dax, S. Dhawan, M. Diepold, L. M. P. Fernandes, A. Giesen, A. L. Gouvea, T. Graf, T. W. Hänsch, P. Indelicato, L. Julien, C.-Y. Kao, P. Knowles, F. Kottmann, E.-O. Le Bigot, Y.-W. Liu, J. A. M. Lopes, L. Ludhova, C. M. B. Monteiro, F. Mulhauser, T. Nebel, P. Rabinowitz, J. M. F. dos Santos, L. A. Schaller, C. Schwob, D. Taqqu, J. F. C. A. Veloso, J. Vogelsang, and R. Pohl. *Proton Structure from the Measurement of 2S-2P Transition Frequencies of Muonic Hydrogen.* Science **339** (2013) 417–420.

[Arnoult2006] O. Arnoult (2006). *Utilisation d'un peigne de fréquences optiques pour la spectroscopie de l'atome d'hydrogène.* PhD thesis, Université Pierre et Marie Curie.

[Arnoult2010] O. Arnoult, F. Nez, L. Julien, and F. Biraben. *Optical frequency measurement of the 1S–3S two-photon transition in hydrogen.* The European Physical Journal D **60** (2010) 243–256.

[Barker1955] W. A. Barker and F. N. Glover. *Reduction of relativistic two-particle wave equations to approximate forms. III.* Phys. Rev. **99** (1955) 317–324.

[Berkeland1997] D. J. Berkeland, F. C. Cruz, and J. C. Bergquist. *Sum-frequency generation of continuous-wave light at 194 nm.* Applied Optics **36** (1997) 4159.

[Bethe1957] H. A. Bethe and E. E. Salpeter (1957). *Quantum mechanics of one- and two-electron atoms.* Springer-Verlag.

[Bevington2003] P. R. Bevington and D. K. Robinson (2003). *Data reduction and error analysis for the physical sciences.* McGraw-Hill, third edition.

[Beyer2017] A. Beyer, L. Maisenbacher, A. Matveev, R. Pohl, K. Khabarova, A. Grinin, T. Lamour, D. C. Yost, T. W. Hänsch, N. Kolachevsky, and T. Udem.

The Rydberg constant and proton size from atomic hydrogen. Science **358** (2017) 79–85.

[Biraben1974] F. Biraben (1974). *Spectroscopie à deux et trois photons sans élargissement Doppler. Application à l'étude des collisions sodium-gaz rare.* Thèse d'Etat, Université Pierre et Marie Curie.

[Biraben1979] F. Biraben, M. Bassini, and B. Cagnac. *Line-shapes in Doppler-free two-photon spectroscopy. The effect of finite transit time.* J. Phys. France **40** (1979) 445–455.

[Biraben1982] F. Biraben and P. Labastie. *Balayage d'un laser à colorant continu monomode sur 150 GHz.* Opt. Commun. **41** (1982) 49.

[Biraben1991] F. Biraben, L. Julien, J. Plon, and F. Nez. *Compensation of the second-order Doppler effect in two-photon spectroscopy of atomic hydrogen.* Europhys. Lett. **15** (1991) 831.

[Bourzeix1993] S. Bourzeix, M. D. Plimmer, F. Nez, L. Julien, and F. Biraben. *Efficient frequency doubling of a continuous wave titanium: sapphire laser in an external enhancement cavity.* Opt. Commun. **99** (1993) 89.

[Bourzeix1995] S. Bourzeix (1995). *Laser continu à 205 nm, application à la mesure du déplacement de Lamb dans l'hydrogène.* PhD thesis, Université Pierre et Marie Curie.

[Bourzeix1997] S. Bourzeix, B. de Beauvoir, F. Nez, F. de Tomasi, L. Julien, and F. Biraben. *Ultra-violet light generation at 205 nm by two frequency doubling steps of a cw titanium-sapphire laser.* Opt. Commun. **133** (1997) 239–244.

[Brown2013] R. C. Brown, S. Wu, J. V. Porto, C. J. Sansonetti, C. E. Simien, S. M. Brewer, J. N. Tan, and J. D. Gillaspy. *Quantum interference and light polarization effects in unresolvable atomic lines: Application to a precise measurement of the* ^{6,7}*Li* D_2 *lines.* Phys. Rev. A **87** (2013) 032504.

[Bryant2000] R. A. Bryant, J. M. Donbar, and J. F. Driscoll. *Acetone laser induced fluorescence for low pressure/low temperature flow visualization.* Experiments in Fluids **28** (2000) 471–476.

[Cagnac2002] B. Cagnac and J.-P. Faroux (2002). *Lasers. Interaction lumière-matière.* EDP Sciences.

[Carlson2015] C. E. Carlson. *The proton radius puzzle.* Progress in Particle and Nuclear Physics **82** (2015) 59–77.

[Cesar2001] C. L. Cesar. *Zeeman effect on the* $1S-2S$ *transition in trapped hydrogen and antihydrogen.* Phys. Rev. A **64** (2001) 023418.

[Cohen-Tannoudji1962] C. Cohen-Tannoudji. *Thèse d'Etat.* Ann. Phys. **13** (1962) 423–468.

[Cohen-Tannoudji1973] C. Cohen-Tannoudji, B. Diu, and F. Laloë (1973). *Mécanique quantique (Tome 2).* Hermann.

[Czarnecki2005] A. Czarnecki, U. D. Jentschura, and K. Pachucki. *Calculation of the one- and two-loop Lamb shift for arbitrary excited hydrogenic states.* Phys. Rev. Lett. **95** (2005) 180404.

[deBeauvoir1997] B. de Beauvoir (1997). *Réalisation d'un étalon de fréquence à 778 nm : mesure absolue des fréquences 2S-8S/D des atomes d'hydrogène et de deutérium et détermination de la constante de Rydberg.* PhD thesis, Université Pierre et Marie Curie.

[deBeauvoir2000] B. de Beauvoir, C. Schwob, O. Acef, L. Jozefowski, L. Hilico, F. Nez, L. Julien, A. Clairon, and F. Biraben. *Metrology of the hydrogen and deuterium atoms: Determination of the Rydberg constant and Lamb shifts.* The European Physical Journal D - Atomic, Molecular, Optical and Plasma Physics **12** (2000) 61–93.

[Drever1983] R. Drever, J. Hall, F. Kowalski, J. Hough, G. Ford, A. Munley, and H. Ward. *Laser phase and frequency stabilization using an optical resonator.* Applied Physics B **31** (1983) 97–105.

[Edmonds1957] A. R. Edmonds (1957). *Angular momentum in quantum mechanics.* Princeton University Press, Princeton, NJ.

[Eides2007] M. I. Eides, H. Grotch, and V. A. Shelyuto (2007). *Theory of Light Hydrogenic Bound States.* Springer.

[Erickson1965] G. W. Erickson and D. R. Yennie. *Radiative level shifts II: Higher order contributions to the Lamb shift.* Ann. Phys. (NY) **35** (1965) 447.

[Fleurbaey2017] H. Fleurbaey, F. Biraben, L. Julien, J.-P. Karr, and F. Nez. *Cross-damping effects in $1S-3S$ spectroscopy of hydrogen and deuterium.* Phys. Rev. A **95** (2017) 052503.

[Galtier2014a] S. Galtier (2014). *High precision spectroscopy of the 1S-3S transition of hydrogen to determine the proton radius.* PhD thesis, Université Pierre et Marie Curie.

[Galtier2014b] S. Galtier, F. Nez, L. Julien, and F. Biraben. *Ultraviolet continuous-wave laser source at 205 nm for hydrogen spectroscopy.* Opt. Commun. **324** (2014) 34–37.

[Galtier2015] S. Galtier, H. Fleurbaey, S. Thomas, L. Julien, F. Biraben, and F. Nez. *Progress in Spectroscopy of the 1S–3S Transition in Hydrogen.* J. Phys. Chem. Ref. Data **44** (2015) 031201.

[Garreau1989] J.-C. Garreau (1989). *Mesure de la constante de Rydberg par spectrocopie à deux photons des états de Rydberg de l'atome d'hydrogène.* PhD thesis, Université Pierre et Marie Curie.

[Girard1983] B. Girard (1983). *Étude par pompage optique à deux photons de l'état* $A\ ^1\Pi$ *de CO.* Thèse de 3^e cycle, Université Pierre et Marie Curie.

[Grynberg1976] G. Grynberg (1976). *Spectroscopie d'absorption à deux photons sans élargissement Doppler. Application à l'étude du sodium et du néon.* Thèse d'Etat, Université Pierre et Marie Curie.

[Haas2006] M. Haas, U. D. Jentschura, C. H. Keitel, N. Kolachevsky, M. Herrmann, P. Fendel, M. Fischer, T. Udem, R. Holzwarth, T. W. Hänsch, M. O. Scully, and G. S. Agarwal. *Two-photon excitation dynamics in bound two-body Coulomb systems including ac Stark shift and ionization.* Phys. Rev. A **73** (2006) 052501.

[Hagel2001] G. Hagel (2001). *Spectroscopie de l'atome d'hydrogène vers une mesure absolue de la fréquence de la transition* $1S - 3S$. PhD thesis, Université Pierre et Marie Curie.

[Hagel2002] G. Hagel, F. Nez, and F. Biraben. *Analysis and observation, on an atomic resonance, of the frequency shift due to the length modulation of an optical cavity.* Applied Optics **41** (2002) 7702–7706.

[Hänsch1972] T. W. Hänsch, I. S. Shahin, and A. L. Schawlow. *Optical Resolution of the Lamb Shift in Atomic Hydrogen by Laser Saturation Spectroscopy.* Nature Physical Science **235** (1972) 63–65.

[Hänsch1980] T. W. Hänsch and B. Couillaud. *Laser frequency stabilization by polarization spectroscopy of a reflecting reference cavity.* Opt. Commun. **35** (1980) 441.

[Hellwig1970] H. Hellwig, R. F. C. Vessot, M. W. Levine, P. W. Zitzewitz, D. Allan, and D. Glaze. *Measurement of the unperturbed hydrogen hyperfine transition frequency.* IEEE Trans. Instr. Meas. **19** (1970) 200–209.

[Horbatsch2010] M. Horbatsch and E. A. Hessels. *Shifts from a distant neighboring resonance.* Phys. Rev. A **82** (2010) 052519.

[Jannin2015] R. Jannin (2015). *Atom interferometry with a Bose-Einstein condensate: effect of internal interactions.* PhD thesis, Université Pierre et Marie Curie.

[Jentschura2002] U. D. Jentschura and P. J. Mohr. *Nonresonant effects in one- and two-photon transitions.* Canadian Journal of Physics **80** (2002) 633–644.

[Jentschura2005] U. Jentschura, S. Kotochigova, E. Le Bigot, P. Mohr, and B. Taylor (2005). *The Energy Levels of Hydrogen and Deuterium (version 2.1).* National Institute of Standards and Technology, Gaithersburg, MD.

[Julien1974] L. Julien (1974). *Étude, par la méthode des anticroisements, de la structure des niveaux n=3 de l'hydrogène atomique produit par excitation dissociative d'hydrogène moléculaire.* Thèse de 3^e cycle, Université Pierre et Marie Curie.

[Karshenboim2002] S. G. Karshenboim and V. G. Ivanov. *Hyperfine structure of the ground and first excited states in light hydrogen-like atoms and high-precision tests of QED.* Eur. Phys. J. D **19** (2002) 13–23.

[Kogelnik1966] H. Kogelnik and T. Li. *Laser Beams and Resonators.* Applied Optics **5** (1966) 1550–1567.

[Kolachevsky2009] N. Kolachevsky, A. Matveev, J. Alnis, C. G. Parthey, S. G. Karshenboim, and T. W. Hänsch. *Measurement of the* $2S$ *hyperfine interval in atomic hydrogen.* Phys. Rev. Lett. **102** (2009) 213002.

[Lamb1947] W. E. Lamb and R. C. Retherford. *Fine structure of the hydrogen atom by a microwave method.* Phys. Rev. **72** (1947) 241.

[Lundeen1981] S. R. Lundeen and F. M. Pipkin. *Measurement of the Lamb shift in hydrogen, n=2.* Phys. Rev. Lett. **46** (1981) 232–235.

[Matveev2017] A. Matveev (2017). Private communication.

[Mohr2000] P. J. Mohr and B. N. Taylor. *CODATA recommended values of the fundamental physical constants: 1998.* Rev. Mod. Phys. **72** (2000) 351–495.

[Mohr2016] P. J. Mohr, D. B. Newell, and B. N. Taylor. *CODATA recommended values of the fundamental physical constants: 2014.* Rev. Mod. Phys. **88** (2016) 035009.

[Olander1970] D. R. Olander, R. H. Jones, and W. J. Siekhaus. *Molecular beam sources fabricated from multichannel arrays. IV. Speed distribution in the centerline beam.* Journal of Applied Physics **41** (1970) 4388–4391.

[Parthey2011] C. G. Parthey, A. Matveev, J. Alnis, B. Bernhardt, A. Beyer, R. Holzwarth, A. Maistrou, R. Pohl, K. Predehl, T. Udem, T. Wilken, N. Kolachevsky, M. Abgrall, D. Rovera, C. Salomon, P. Laurent, and T. W. Hänsch. *Improved measurement of the hydrogen 1S–2S transition frequency.* Phys. Rev. Lett. **107** (2011) 203001.

[Pohl2010] R. Pohl, A. Antognini, F. Nez, F. D. Amaro, F. Biraben, J. M. R. Cardoso, D. S. Covita, A. Dax, S. Dhawan, L. M. P. Fernandes, A. Giesen, T. Graf, T. W. Hänsch, P. Indelicato, L. Julien, C.-Y. Kao, P. Knowles, E.-O. Le Bigot, Y.-W. Liu, J. A. M. Lopes, L. Ludhova, C. M. B. Monteiro, F. Mulhauser, T. Nebel, P. Rabinowitz, J. M. F. dos Santos, L. A. Schaller, K. Schuhmann, C. Schwob, D. Taqqu, J. F. C. A. Veloso, and F. Kottmann. *The size of the proton.* Nature **466** (2010) 213–216.

[Pohl2016] R. Pohl, F. Nez, L. M. P. Fernandes, F. D. Amaro, F. Biraben, J. M. R. Cardoso, D. S. Covita, A. Dax, S. Dhawan, M. Diepold, A. Giesen, A. L. Gouvea, T. Graf, T. W. Hänsch, P. Indelicato, L. Julien, P. Knowles, F. Kottmann, E.-O. Le Bigot, Y.-W. Liu, J. A. M. Lopes, L. Ludhova, C. M. B. Monteiro, F. Mulhauser, T. Nebel, P. Rabinowitz, J. M. F. dos Santos, L. A. Schaller, K. Schuhmann, C. Schwob, D. Taqqu, J. F. C. A. Veloso, A. Antognini, and the CREMA collaboration. *Laser spectroscopy of muonic deuterium.* Science **353** (2016) 669–673.

[Ramsey1956] N. F. Ramsey (1956). *Molecular beams.* Oxford University Press.

[Rothery2000] N. E. Rothery and E. A. Hessels. *Measurement of the* $2S$ *atomic hydrogen hyperfine interval.* Phys. Rev. A **61** (2000) 044501.

[Sapirstein1990] J. R. Sapirstein and D. R. Yennie (1990). *Theory of hydrogenic bound states.* In *Quantum Electrodynamics*, edited by T. Kinoshita, chapter 12, pp. 560–672. World Scientific.

[Touahri1997] D. Touahri, O. Acef, A. Clairon, J.-J. Zondy, R. Felder, L. Hilico, B. de Beauvoir, F. Biraben, and F. Nez. *Frequency measurement of the* $5S_{1/2}(F = 3) - 5D_{5/2}(F = 5)$ *two-photon transition in rubidium.* Opt. Commun. **133** (1997) 471–478.

[Verkerk1989] P. Verkerk, M. Pinard, F. Biraben, and G. Grynberg. *1S-3S and 1S-3D Doppler-free two-photon transition in hydrogen and deuterium.* Opt. Commun. **72** (1989) 202–204.

[Vigué2014] J. Vigué (2014). Private communication.

[Walraven1982] J. T. M. Walraven and I. F. Silvera. *Helium temperature beam source of atomic hydrogen.* Review of Scientific Instruments **53** (1982) 1167–1181.

[Yost2014] D. C. Yost, A. Matveev, E. Peters, A. Beyer, T. W. Hänsch, and T. Udem. *Quantum interference in two-photon frequency-comb spectroscopy.* Phys. Rev. A **90** (2014) 012512.

[Yost2016] D. C. Yost, A. Matveev, A. Grinin, E. Peters, L. Maisenbacher, A. Beyer, R. Pohl, N. Kolachevsky, K. Khabarova, T. W. Hänsch, and T. Udem. *Spectroscopy of the hydrogen* $1S - 3S$ *transition with chirped laser pulses.* Phys. Rev. A **93** (2016) 042509.

Métrologie de la fréquence de transition 1S–3S dans l'hydrogène : contribution au débat sur le rayon de charge du proton

Résumé : La mesure précise de la fréquence de la transition 1S–3S de l'atome d'hydrogène est d'un grand intérêt pour l'énigme du rayon de charge du proton, qui a pour origine les résultats récents de la spectroscopie de l'hydrogène muonique. Nous excitons la transition à deux photons 1S–3S, dans un jet d'atomes d'hydrogène, à l'aide d'un laser continu à 205 nm obtenu par somme de fréquences dans un cristal non-linéaire. La fréquence de la transition est mesurée par rapport à l'horloge à césium du LNE-SYRTE à l'aide d'un peigne de fréquence.

L'enregistrement du signal pour différentes valeurs d'un champ magnétique appliqué permet d'estimer la distribution de vitesse des atomes du jet et d'en déduire l'effet Doppler du deuxième ordre. Les autres effets systématiques qui déplacent la transition ont été pris en compte : interférence quantique, déplacement lumineux, collisions. Une étude systématique en fonction de la pression a permis de montrer que la distribution de vitesse ne dépend pas de la pression et de déterminer le déplacement collisionnel.

Finalement, une valeur de la fréquence de transition 1S–3S est obtenue avec une incertitude d'environ 5 kHz, ou $1{,}7 \times 10^{-12}$ en valeur relative. Elle est en très bon accord avec la valeur recommandée par le CODATA. Cette nouvelle mesure contribue à la recherche autour de l'énigme du rayon du proton.

Frequency metrology of the 1S–3S transition of hydrogen: contribution to the proton charge radius puzzle

Abstract: The precise measurement of the 1S–3S transition frequency of hydrogen could have a great impact on the proton charge radius puzzle, which results from the recent spectroscopy of muonic hydrogen. In our experiment, the two-photon 1S–3S transition is excited in a hydrogen atomic beam, with a continuous-wave 205-nm laser which is obtained by sum frequency generation in a non-linear crystal. The transition frequency is measured with respect to the LNE-SYRTE Cs clock by means of a frequency comb.

Recording the signal for several values of an applied magnetic field allows to estimate the velocity distribution of the atoms in the beam and deduce the second-order Doppler shift. Other frequency-shifting systematic effects have been taken into account: cross-damping, light shift, collisions. A complete study has shown that the velocity distribution does not depend significantly on the pressure, and allowed to determine the collisional shift.

Eventually, a value of the 1S–3S transition frequency is obtained with an uncertainty of about 5 kHz, or a relative uncertainty of 1.7×10^{-12}. It is in very good agreement with the CODATA recommended value. This new measurement contributes to the ongoing search to solve the proton radius puzzle.